

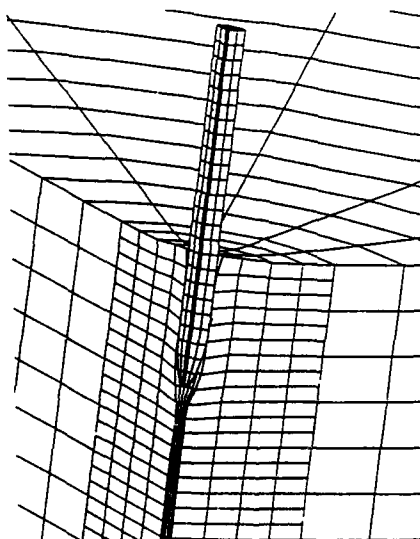


①

NCEL

November 1992
By Larry R. Hoge and
T.A. Shugar

Technical Note

Sponsored By Office of Chief of Naval
Research**THREE-DIMENSIONAL FINITE ELEMENT MODELING
OF CONFINEMENT STRESS FOR PROJECTILES
EMBEDDED IN ROCK - A PRELIMINARY STUDY**S DTIC
ELECTE
DEC 31 1992
A D92-32962
ABSTRACT

The explicit three-dimensional finite element computer program DYNA3D was applied to the problem of modeling penetration of anchor projectiles into seafloor rock media. It was used to compute the dynamic response and the residual stresses and strains for an axisymmetric penetration model where the penetrator axis and velocity vector are normal to the seafloor. Homogeneous nonlinear material behavior is considered for both the anchor projectile and the seafloor rock material, and a frictional interface is prescribed between the anchor projectile and rock media. An introductory discussion of cavity expansion theory is also included and used to guide physical interpretation of the data obtained from the numerical model. Validation of the three-dimensional model was limited to comparison with previous DYNA2D results for penetration depths. Qualitative agreement with very approximate analytical methods was also observed. A parameter study revealed that the rock target hardness, as represented by the strain hardening modulus in an elastic-plastic model of rock behavior, strongly influenced the confinement stress acting on the embedded projectile. Conversely, it was found that the coefficient of friction of the contact surface between the projectile and rock had only minor effect on the confinement stress, although it did affect the depth of penetration. DYNA3D is potentially a convenient and forthcoming framework for determining the relationship between confinement stress and various parameters of seafloor rock and anchor projectiles.

NAVAL CIVIL ENGINEERING LABORATORY PORT HUENEME CALIFORNIA 93043-4328

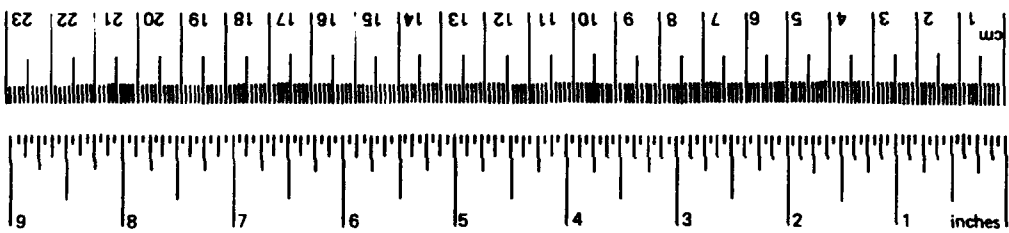
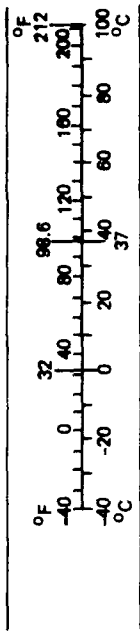
Approved for public release; distribution is unlimited.

92 12 28 137

METRIC CONVERSION FACTORS

Approximate Conversions to Metric Measures				Approximate Conversions from Metric Measures			
Symbol	When You Know	Multiply by	To Find	Symbol	When You Know	Multiply by	To Find
in ft yd mi	inches	*2.5 30 0.9 1.6	centimeters	mm cm m km	millimeters	0.04 0.4 3.3 1.1 0.6	inches
	feet		centimeters		centimeters		inches
	yards		meters		meters		feet
	miles		kilometers		kilometers		yards miles
in ² ft ² yd ² mi ²	square inches	6.5 0.09 0.8 2.6 0.4	square centimeters	cm ² m ² km ² ha	square centimeters	0.16 1.2 0.4 2.5	square inches
	square feet		square meters		square meters		square yards
	square yards		square meters		square kilometers		square miles
	square miles		square kilometers		hectares (10,000 m ²)		acres
oz lb	ounces	28 0.45 0.9	grams	g kg t	grams	0.035 2.2 1.1	ounces
	pounds		kilograms		kilograms		pounds
	short tons		tonnes		tonnes (1,000 kg)		short tons
	(2,000 lb)						
tsp Tbsp fl oz c pt qt gal ft ³ yd ³	teaspoons	5 15 30 0.24 0.47 0.95 3.8 0.03 0.76	milliliters	ml l m ³	milliliters	0.03 2.1 1.06 0.26 35 1.3	fluid ounces
	tablespoons		milliliters		liters		pints
	fluid ounces		milliliters		liters		quarts
	cups		liters		liters		gallons
	pints		liters		cubic meters		cubic feet
	quarts		liters		cubic meters		cubic yards
	gallons		liters				
	cubic feet		cubic meters				
	cubic yards		cubic meters				
°F	Fahrenheit temperature	5/9 (after subtracting 32)	Celsius temperature	°C	Celsius temperature	9/5 (then add 32)	Fahrenheit temperature

*1 in = 2.54 (exactly). For other exact conversions and more detailed tables, see NBS Misc. Publ. 286, Units of Weights and Measures, Price \$2.25, SD Catalog No. C13.10-286.



REPORT DOCUMENTATION PAGEForm Approved
OMB No. 0704-018

Public reporting burden for this collection of information is estimated to average 1 hour per response, including the time for reviewing instructions, searching existing data sources, gathering and maintaining the data needed, and completing and reviewing the collection of information. Send comments regarding this burden estimate or any other aspect of this collection information, including suggestions for reducing this burden, to Washington Headquarters Services, Directorate for Information and Reports, 1215 Jefferson Davis Highway, Suite 1204, Arlington, VA 22202-4302, and to the Office of Management and Budget, Paperwork Reduction Project (0704-0188), Washington, DC 20503.

1. AGENCY USE ONLY (Leave blank)		2. REPORT DATE November 1992	3. REPORT TYPE AND DATES COVERED Final: Jan 1990 through Oct 1990
4. TITLE AND SUBTITLE THREE-DIMENSIONAL FINITE ELEMENT MODELING OF CONFINEMENT STRESS FOR PROJECTILES EMBEDDED IN ROCK - A PRELIMINARY STUDY		5. FUNDING NUMBERS PR - YR023.08.01 WU - DN666359	
6. AUTHOR(S) Larry R. Hoge and T.A. Shugar			
7. PERFORMING ORGANIZATION NAME(S) AND ADDRESS(ES) Naval Civil Engineering Laboratory Port Hueneme, CA 93043-4328		8. PERFORMING ORGANIZATION REPORT NUMBER TN - 1848	
9. SPONSORING/MONITORING AGENCY NAME(S) AND ADDRESS(ES) Office of the Chief of Naval Research Office of Naval Technology Arlington, VA 22217-5000		10. SPONSORING/MONITORING AGENCY REPORT NUMBER	
11. SUPPLEMENTARY NOTES			
12a. DISTRIBUTION/AVAILABILITY STATEMENT Approved for public release; distribution is unlimited.		12b. DISTRIBUTION CODE	
13. ABSTRACT (Maximum 200 words) <p>The explicit three-dimensional finite element computer program DYNA3D was applied to the problem of modeling penetration of anchor projectiles into seafloor rock media. It was used to compute the dynamic response and the residual stresses and strains for an axisymmetric penetration model where the penetrator axis and velocity vector are normal to the seafloor. Homogeneous nonlinear material behavior is considered for both the anchor projectile and the seafloor rock material, and a frictional interface is prescribed between the anchor projectile and rock media. An introductory discussion of cavity expansion theory is also included and used to guide physical interpretation of the data obtained from the numerical model. Validation of the three-dimensional model was limited to comparison with previous DYNA2D results for penetration depths. Qualitative agreement with very approximate analytical methods was also observed. A parameter study revealed that the rock target hardness, as represented by the strain hardening modulus in an elastic-plastic model of rock behavior, strongly influenced the confinement stress acting on the embedded projectile. Conversely, it was found that the coefficient of friction of the contact surface between the projectile and rock had only minor affect on the confinement stress, although it did affect the depth of penetration. DYNA3D is potentially a convenient and forthcoming framework for determining the relationship between confinement stress and various parameters of seafloor rock and anchor projectiles.</p>			
14. SUBJECT TERMS Finite element, explicit integration, DYNA3D, rock penetration, seafloor anchors			15. NUMBER OF PAGES 108
			16. PRICE CODE
17. SECURITY CLASSIFICATION OF REPORT Unclassified	18. SECURITY CLASSIFICATION OF THIS PAGE Unclassified	19. SECURITY CLASSIFICATION OF ABSTRACT Unclassified	20. LIMITATION OF ABSTRACT UL

FOREWORD

The objective of Ocean Floor Rock Embedment Mechanics (OFREM) research is to develop a better understanding of interaction of rock media and ballistically embedded projectiles that ultimately can serve as ocean floor anchors. Current tasks are to: (a) determine the model scale effects for penetration into intact and jointed rock, (b) mathematically simulate the penetration process, (c) determine projectile extraction resistance and projectile/target interaction, and (d) mathematically simulate the projectile extraction process.

From FY88 through FY90, the University of California at Berkeley under contract to NCEL was tasked to formulate analytical models for predicting projectile anchor extraction in rock masses. Due to personnel turnover, the originally proposed analytical work based upon the use of the DYNA codes from Lawrence Livermore National Laboratory was discontinued. At about the same time, the DYNA codes were imported for use on unrelated projects in the 6.2 NAVFAC/NCEL Exploratory Development program. The present project resumes the originally proposed research based upon these codes, addressing the problems of numerical simulation of the penetration process, projectile/target interaction, and prediction of extraction resistance.

A similar project report for this study was submitted by the first author in partial fulfillment of the requirements for the degree of Master of Science in Mechanical Engineering at California State University, Northridge in May 1992; the title of the thesis is "Stress Surrounding Projectile Anchors."

Accession For	
NTIS	CRA&I <input checked="" type="checkbox"/>
DTIC	TAB <input type="checkbox"/>
Unannounced	<input type="checkbox"/>
Justification	
By	
Distribution /	
Availability Codes	
Dist	Avail and/or Special
A-1	

CONTENTS

	Page
INTRODUCTION	1
Objective	2
Scope	3
REVIEW OF PREVIOUS SOLUTION METHODS	4
Analytical Methods	4
DYNA2D Studies	5
THREE-DIMENSIONAL FINITE ELEMENT MODELS FOR PENETRATION . .	6
Previous DYNA3D Studies	7
Fastener Model Using DYNA3D	8
NUMERICAL MODEL TECHNIQUE AND DEMONSTRATION	20
Parameter Study	20
Larger Anchor Projectile Study	29
ANALYSIS OF CONFINEMENT STRESS	37
Description and Discussion of Residual and Confinement Stress Data	37
Discussion of Results	38
SUMMARY AND CONCLUSIONS	45
RECOMMENDATIONS	47
REFERENCES	48
APPENDIXES	
A - A Spherical Cavity Expansion Theory	A-1
B - Analysis of a Dynamic Cylindrical Cavity Expansion Theory	B-1
C - Overview Comments on DYNA3D	C-1
D - Annotated INGRID Input Data File	D-1
E - Sample INGRID, DYNA3D, and TAURUS Session	E-1
F - INGRID Input Data Files for Penetration Simulations	F-1

CONTENTS (continued)

Page

Tables

1	Mechanical Properties of Rock Materials.	13
2	Material Properties of AISI 4340 Steel	14
3	Projectile Material Properties for Material Model #3	14
4	Target Material Properties for Material Model #3	14
5	Target Material Properties for Material Model #5	26
6	Projectile Material Properties for the Larger Anchor Projectile	32
7	Target Material Properties for the #3 Larger Anchor Projectile	33
8	Target Material Properties Used With Material Model #5 for the Larger Anchor Projectile	34

Figures

1	Deployment of a propellant-embedment anchor system into conventional seafloor soil	1
2	Radial stress from spherical cavity expansion theory	5
3	Rainsberger penetration model and location of slide surfaces	8
4	Size of small fastener projectile in millimeters	9
5	The two-dimensional geometry of the projectile from Zhou's penetration problem	10
6	Two-dimensional representation of the projectile and target from Zhou's penetration problem	11
7	DYNA3D finite element penetration model for fastener projectile	12

CONTENTS (continued)

Figures	Page
8 Uniaxial stress-strain curve showing elastic-plastic material behavior for kinematic hardening ($\beta = 0$) and isotropic hardening ($\beta = 1$)	15
9 Projectile embedded in the target at end of the simulation	16
10 Projectile response from DYNA3D	17
11 Contours of residual pressure in the target	18
12 Projectile response from DYNA2D	19
13 Effect of target tunnel diameter on penetration depth, velocity, and acceleration	21
14 Residual pressure contours in the target for various tunnel diameters	22
15 Normalized chart for the effect of the target/projectile diameter ratio on the maximum penetration depth	23
16 Effect of friction coefficient on projectile penetration depth, velocity, and acceleration	25
17 Pressure versus volumetric strain curve for soil and crushable foam material model	26
18 Projectile embedded in target characterized by material model #5	27
19 Effect of rock target material models on projectile penetration depth, velocity, and acceleration	28
20 Effect of target hardening modulus on projectile penetration depth, velocity, and acceleration	30
21 Contours of residual pressure in the target for varying hardening modulus values	31
22 Larger anchor projectile	32

CONTENTS (continued)

Figures	Page
23 DYNA3D finite element penetration model for larger anchor projectile	33
24 Effect of target material models on larger anchor projectile penetration depth, velocity, and acceleration	35
25 Contours of target pressure for larger anchor projectile material model #5	36
26 Stress block at center of a typical finite element in target model	38
27 Residual stresses for smaller fastener anchor projectile in sandstone	39
28 The effect of tunnel-to-projectile diameter ratio on residual stress	42
29 Normal stress, σ_x , for zero coefficient of friction	43
30 Normal stress, σ_x , for zero strain hardening modulus	43
31 Residual stress for larger anchor projectile in sandstone	44
32 Confinement stress distribution for larger anchor projectile embedded in sandstone	45
A-1 One-dimensional coordinate system, stress and material behavior	A-2
A-2 Coordinate system, stress definitions, and material behavior region	A-3
A-3 Radial stress in elastic region	A-5
A-4 Radial stress in cracked and elastic regions	A-8
A-5 Constants model for pressure-dependent shear strength	A-9

INTRODUCTION

The Naval Civil Engineering Laboratory (NCEL) has developed a line of semipermanent mooring and anchor devices called propellant-embedment anchor (PEA) systems. They come in a family of sizes of 10K, 20K, 100K, and 300K, where K denotes 1,000 pounds of nominal pullout capacity in conventional seafloor soil. The assembled PEA system is composed of a launcher and a projectile. To deploy the system it is lowered over the side of the ship, and when the ocean floor is sensed, the propellant charge is detonated, and the launcher ballistically drives the projectile into the ocean floor. Figure 1 shows the sequence of events for conventional applications. The launcher assembly is composed of a modified gun barrel and a hemispherical reaction vessel. The reaction vessel provides recoil resistance to the downward thrust of the projectile caused by the propellant burn inside the modified gun barrel. The projectile is composed of a piston and an anchor fluke. The anchor flukes come in varied configurations to facilitate penetration into different ocean floor materials -- mud, clay, silt, sand, gravel, coral, or rock. In this study, the material of interest is rock.

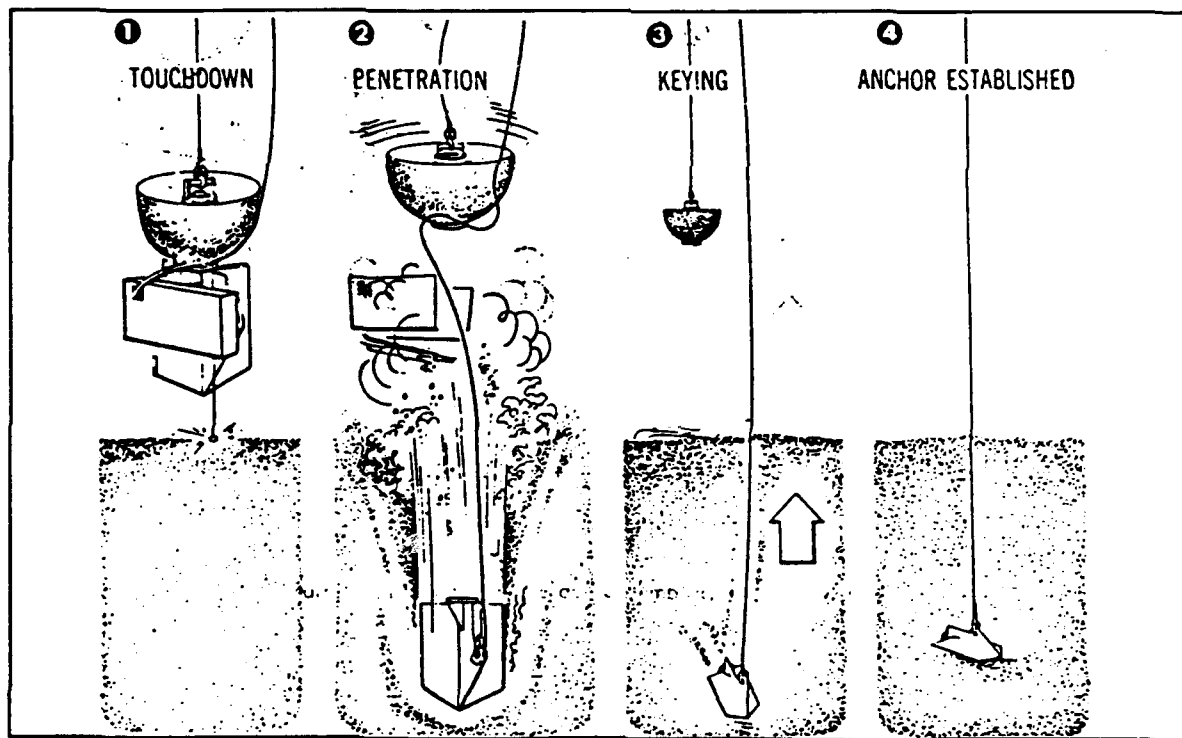


Figure 1
Deployment of a propellant-embedment anchor system into conventional seafloor soil.

Penetration of rock anchor projectiles depends on parameters such as initial kinetic energy, geometry of the projectile, interface friction, and constitutive properties of the seafloor rock material. Given these parameters, it should be possible to construct simplified and reliable models that predict the depth of penetration and the residual stress distribution surrounding the embedded anchor. The pullout resistance may be predicted once the confinement stress and the interface friction are known.

Data from various analytical and numerical investigations of the problem need to be developed to form the basis for simplified penetration and extraction model development. These simplified models, employing physical as well as empirical and interpolated parameters, would be used to predict the performance of PEA systems in seafloor rock media, including pullout capacity.

Based upon full-scale field tests in ocean sandstone and basalt rock, Beard (1984) concluded that the technology of PEA is feasible. Penetration depths up to one meter and maximum extraction forces of 200,000 pounds were obtained using the 20K propellant embedment anchor system. However, the penetration depths could not be correlated with anchor holding capacities, as concluded by Wadsworth and Beard (1980).

Therefore, the development of analytical models and numerical methods to simulate anchor penetration and extraction processes was initiated to improve understanding of the penetration and extraction processes. This also includes studying the response of seafloor rock materials under high rates of loading, and developing validated confinement and friction models for describing the anchor extraction process, both of which are being pursued elsewhere.

Analytical and numerical solution approaches to penetration problems have concentrated on predicting the depth of penetration and have, for the most part, ignored the structural response of the penetrator. Most approaches assume the penetration process can be formulated as axisymmetric with a rigid projectile. Deformations of a steel anchor projectile are often small compared to the target material, but stresses in the projectile may be very large.

Beard (1984) recorded some mechanical failures of the PEA systems, such as kinking and birdcaging of the mooring cable as well as shackle fractures, in the field tests. These failures were attributed to high deceleration forces. Shugar and Wager (1982) described structural failures of the larger PEA reaction vessel due to overpressure from the gun barrel muzzle. Therefore, in addition to prediction of the penetration process, prediction of the structural dynamics of the PEA system, including the projectile, is necessary since it imposes structural and mechanical constraints on system performance. Further, structural dynamics calculations can assist in the evaluation of alternative shapes of projectiles which are subject to mechanical constraints. Consequently, when the survivability of the anchor projectile is important, deformable projectile models are required. For these reasons, a deformable projectile model is demonstrated in this study instead of a simple rigid projectile model.

Objective

The objective of this preliminary study was to develop a numerical modeling technique for understanding the residual stresses surrounding deformable anchor projectiles that have been ballistically embedded in rock media. The approach was to include explicit finite element technology to model the nonlinear dynamic response of the projectile and surrounding rock media.

Further, the effects of various numerical model parameters on depth of penetration and confinement stress were to be studied to promote development of hypotheses for simplified models of the penetration process.

Scope

The explicit finite element computer program DYNA3D (Whirley and Hallquist, 1991) was employed to model the nonlinear structural dynamics of the penetration problem. The three-dimensional dynamic finite element solution approach included nonlinear material behavior and slide line interface behavior.

A static spherical cavity expansion theory for brittle materials (Forrestal and Longcope, 1990) was also pursued for general background into analytical procedures used for predicting penetration processes. Another potentially more powerful analytical solution was also pursued in the hope that it could be used to independently verify at least some part of the numerical solution such as prediction of penetration depth. A dynamic cylindrical cavity expansion theory, presented by Zhou (1988), was investigated in this regard.

The publications of Schwer and co-workers, Schwer, et al. (1988) and Schwer and Day (1991), were very useful, and the first paper was influential in the direction of the present research. It discussed the Lagrangian and Eulerian numerical frameworks for penetration problems and concluded that the former framework is more advantageous, particularly for computing the structural response of the penetrator. Further, the use of a prescribed artificial tunnel was recommended in the construction of the numerical model of the target medium to gain control of simulation time at the expense of having to assume a predetermined penetration path. The first publication also addresses axisymmetric analysis with DYNA2D while the second publication addresses three-dimensional analysis with DYNA3D. The latter publication became known to us only after the present study was completed. It presents three-dimensional studies of penetration and perforation processes in concrete and steel slabs. Where a single plane of symmetry exists in such problems, the use of a technique called the "local modified symmetry constraint" method, in lieu of the tunnel technique, is recommended. However, the tunnel technique, which is advocated in the present study, is currently the only alternative when fully three-dimensional simulation is required. For example, when the effects of in-situ rock fracture conditions are to be included, a fully three-dimensional model will be required to handle material anisotropy.

Zhou (1988) and Goldsmith and Zhou (1989) have demonstrated some agreement between DYNA2D predictions and laboratory measurements of projectile penetration into rock specimens. In the present study, a measure of verification was also sought by comparing Zhou's DYNA2D results with DYNA3D results for an axisymmetric model.

Material properties encountered in a literature survey were used in this study to specify material behavior of the rock and projectile. Material properties for rock media were found to vary significantly from publication to publication. This variation defines parametric ranges over which future numerical penetration models may eventually be exercised to sort out the consequences of the variation. For purposes of this study, the mechanical property data compiled by Goldsmith and Zhou (1989) were used in conjunction with elasto-plastic models of material behavior in the development of the numerical penetration model.

The DYNA3D finite element program and the corresponding pre- and post-processor codes, INGRID and TAURUS, were installed on a Sun 4/260 computer workstation. The

computer simulation times reported are based on the processor speed for this hardware; the processor ran at 25 MHz and is rated at 11 mips or 4 MFLOPS.

REVIEW OF PREVIOUS SOLUTION METHODS

Analytical Methods

Analytical methods for solving projectile penetration problems are based on either the cavity expansion theory or the differential area force law as explained by Heuzé (1989). These methods seek closed form or analytical solutions for the pressure on the projectile tip and the depth of penetration.

Cavity expansion theory employs either a spherical or a cylindrical geometry. The former is suited to penetration by blunt nose projectiles, while the latter is suited to penetration by conical nose projectiles. These theories may further be categorized as static or dynamic. Resistance to penetration is assumed to be due to the shear strength of the target material. Closed form solutions for pressure on the projectile tip and depth of penetration are provided. However, they do not predict the confinement stress on the projectile body which is needed for determining anchor extraction force. Further, they do not address the stress response of the projectile.

The differential area force law provides explicit formulations for the normal stress and tangential stress at every point on the external surface of the penetrator. This approach is three-dimensional and consists of a six-degree-of-freedom analysis of a rigid body penetrator. The method is primarily empirical because the material coefficients are empirically determined. According to Schwer et al. (1988), this theory is the basis for the PENCO2D program (Creighton, 1982), and deceleration histories of rigid body penetrators are easily and adequately predicted by this program for normal impacts. Clearly, PENCO2D was developed to address target penetration, excluding the structural response of the penetrator.

The application of static spherical cavity expansion theory for determining resistance to penetration into brittle materials, including cracking, has been pursued by Forrestal and Longcope (1990). This approach to an otherwise complex problem is compelling in its simplicity. It is useful since it can provide the stress acting on the tip of the projectile in the presence of elastic, plastic, and cracking material behavior in the target. In an auxiliary penetration model, the dynamics of a rigid spherical penetrator is considered, and the stress found by application of a spherical cavity expansion theory is integrated over the surface of the projectile nose to get the force resisting penetration. The analytical model helps in defining the parameters that are important to the determination of target resistance. Moreover, it serves as a guide to interpretation of results from numerical models as is demonstrated in the section "Analysis of Confinement Stress" in this report.

Appendix A contains a review and derivation of the associated equations of the spherical cavity expansion theory developed by Forrestal and Longcope (1990). For brittle materials the shear strength varies with confinement pressure. Thus, the radial stress which will retard penetration of a hemispherical projectile will vary with the pressure dependent shear strength parameter for the target material. This dependency is shown in Figure 2 for both a ceramic and plain concrete target material. The increase in hardness of the target due to the assumption of incompressible material behavior is also indicated for each material. This, for example, suggests the possibility that saturated soil or rock materials on the seafloor would develop a similar

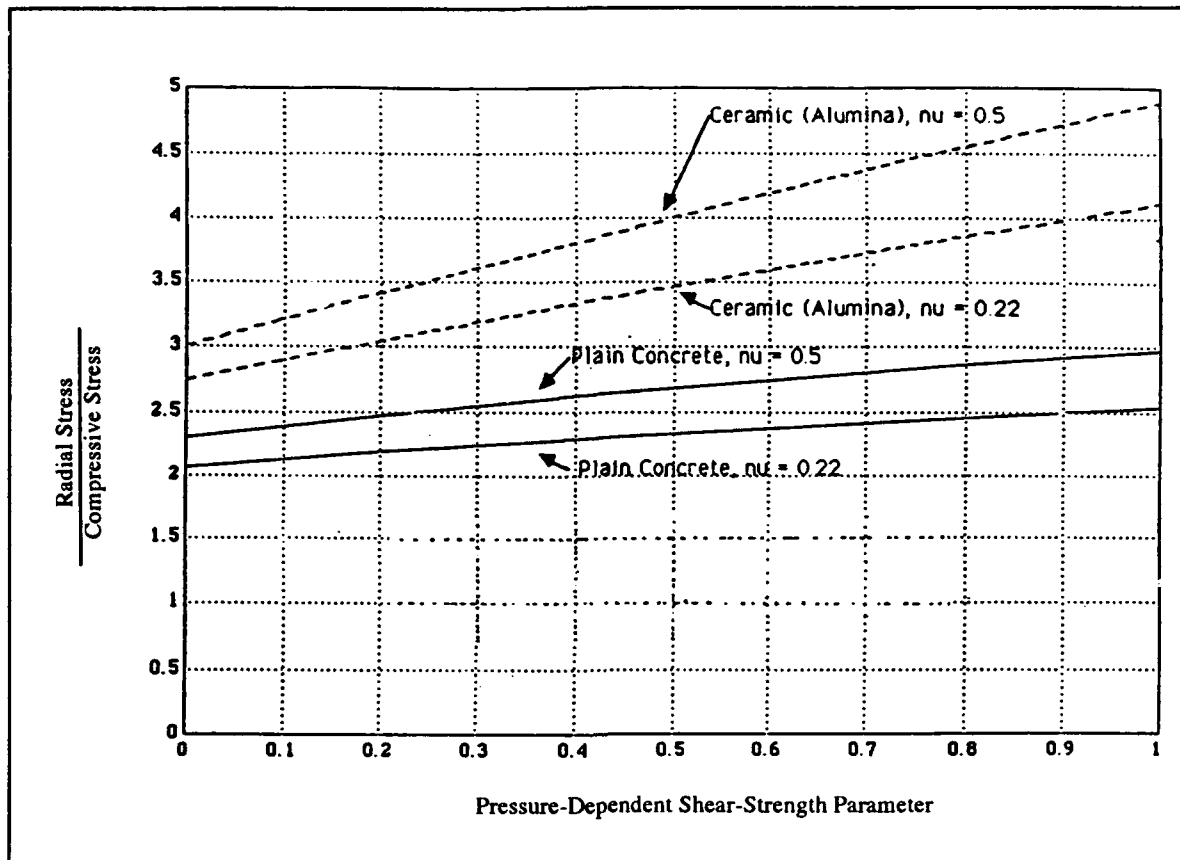


Figure 2
Radial stress from spherical cavity expansion theory.

increase in apparent hardness since water in the pores would not have time to migrate away from the projectile during the highly transient event.

Zhou (1988) presents a full discussion of a dynamic cylindrical cavity expansion theory for anchor penetration problems. Though simplifications designed to facilitate application were introduced, Zhou apparently felt the theory still remained too cumbersome for application and did not apply it in conjunction with his numerical studies. The set of equations derived were not exercised by Zhou, but they potentially offered a means in the present study to independently validate numerical predictions of depth of penetration using DYNA3D. This was an inducement to further analysis of these equations in the present study. However, it was soon found that the expression given for shear resistance contained an infinite series which diverged. The corresponding equations and the n th-term test for identifying divergent series are presented in Appendix B. The cause of the errant equation is unknown, and further work is required to apply this theory.

DYNA2D Studies

Zhou (1988) investigated the normal impact penetration of a fastener projectile into concrete and sandstone. He used theoretical, experimental, and numerical approaches in the study. Comparisons obtained between numerical and experimental data were reasonably good.

As mentioned, no comparisons were made using the cylindrical cavity expansion theory approach though an extensive presentation of the theory was given.

Zhou and Goldsmith (1989) also investigated factors related to PEA projectiles embedded in rock. They attempted to provide an analytical solution which was directly applicable to PEA projectiles based on the theory of elasticity, but certain nonlinear terms defied solution and the analytical effort was terminated. They also reported on a preliminary numerical study. The results from this numerical study were compared to experimental results with reasonably good correlation. Unfortunately, the DYNA2D input data file necessary for repeating the analysis was not presented and replication of the analysis using DYNA3D, as described herein, was therefore not necessarily precise.

Numerical modeling techniques based upon using DYNA2D to describe the target were emphasized in Schwer, et al. (1988). Success rested on the prescription of a small tunnel at the center of the axisymmetric model of the target which also predetermines the path the penetrator would be constrained to follow. The tunnel had the practical modeling effect of reducing the severity of element distortion in the finite element mesh, and reducing the computation time without apparently otherwise affecting the results. The agreement with experimental results was considered acceptable.

THREE-DIMENSIONAL FINITE ELEMENT MODELS FOR PENETRATION

Numerical modeling of the penetration process can be approached by using finite element, finite difference, or discrete element methods. Both Lagrangian and Eulerian formulations of finite element and finite difference methods have been used, and each has its advantages and limitations.

Eulerian codes are generally used for fluid dynamic problems where the fluid enters and exits from a control volume. They are also applicable to large strain problems in solid mechanics. They have been applied to the penetration problem with the target being the control volume. They are more advantageous than the Lagrangian codes when very large strains are involved because no distortions can occur to the control volume grid; this obviates the need to re-zone the model grid at various times during the simulation of the problem. The difficulty with using Eulerian codes involves inaccurate descriptions and calculations of material boundaries and interface conditions. Processing structural response information from Eulerian codes requires careful treatment of data on how the penetrator is flowing through the grid (Schwer et al., 1988). The assumption of a rigid penetrator often accompanies an Eulerian code application to remove this modeling difficulty. If a rigid penetrator model is satisfactory, Eulerian codes may be competitive for penetration problems.

Lagrangian codes require the model grid to follow displacements of the material. They provide a more accurate prediction of interface definition and behavior as well as penetrator structural response, if deformations of the grid can be managed so that re-meshing is avoided or minimized. The three-dimensional program DYNA3D is strictly a Lagrangian finite element code, while the two-dimensional program DYNA2D is primarily a Lagrangian code with limited Eulerian formulation capability.

Understanding how the anchor extraction force is dependent on the damaged rock material adjacent to the embedded projectile is crucial in predicting performance of anchor projectile systems as noted by Wilson et al. (1990). Predicting the resulting post anisotropic state of the target material, as well as including the in-situ anisotropic state of the target, are potentially

important features of successful numerical simulation. As these features are not generally axisymmetric, three-dimensional models are required to replicate them. Therefore, application of DYNA3D vice DYNA2D for simulation of the penetration process has been pursued in the present study to promote procedures and techniques for calculating fully three-dimensional confinement stresses surrounding embedded projectile anchors. DYNA3D is also currently regarded as being better supported for material models that can be used for describing the behavior of rock. Additional advantages of DYNA3D vice DYNA2D for anchor projectile penetration simulation might also include the potential for any future extension to oblique angles of impact and non-rotationally symmetric anchor projectiles.

Three-dimensional modeling in the present investigation employed quarter models of axisymmetric configurations because they are sufficient to develop three-dimensional modeling techniques while minimizing simulation time. Fully three-dimensional model demonstrations were beyond the scope of this initial investigation.

The critical feature of the DYNA codes relative to the objectives of the present project is their capability for handling sliding interfaces (Hallquist, 1978). The numerical treatment involves slave and master node lines defined by the user such that a slave node is constrained to slide on a line between two adjacent master nodes subsequent to impact until a tensile force develops. A separation between a slave and master line is referred to as a void in DYNA3D parlance. The designation of the master surface is apparently arbitrary (Hallquist, 1977). The dynamics of contact/impact and master/slave interfaces as well as other pertinent features, are discussed further in Appendix C, where a brief description of DYNA3D is provided.

Previous DYNA3D Studies

Rainsberger Example. Rainsberger (1988) developed an example of a three-dimensional finite element penetration model using DYNA3D. He fully described the necessary parameters needed to reproduce the computational results for a projectile penetrating a rock target. The grid technique for both the target and the projectile was described.

The Rainsberger example was reproduced in this study at the outset to verify that the software system consisting of INGRID, DYNA3D, and TAURUS was operating as intended. INGRID and TAURUS are, respectively, pre- and post-processor programs for DYNA3D. The example consisted of a two-part steel projectile penetrating a target. The target material behavior was modeled by a soil/crushable foam material model (DYNA3D Material Type 5). All the parameters were defined and presented in an INGRID input data file. The example contained a quarter model (two planes of symmetry were exploited) with three slide surfaces defined as shown in Figure 3. Slide surface 1 was used to tie the two-part steel projectile together. Slide surface 2 was a sliding interface (including separation or void formation) between the projectile and the target. Slide surface 3 was used to tie the differently zoned target model together and, thus, avoid the requirement for special transition elements at the interface. After the skill necessary for using the pre- and post-processor programs and the slide line capability was developed, the example was reproduced as published. Though not shown here, the resulting pressures in the target, on the projectile, and at the projectile/target interface were typical of the type of data sought in the present project. The Rainsberger example thus provided the initial guidance required to apply DYNA3D to the problem at hand.

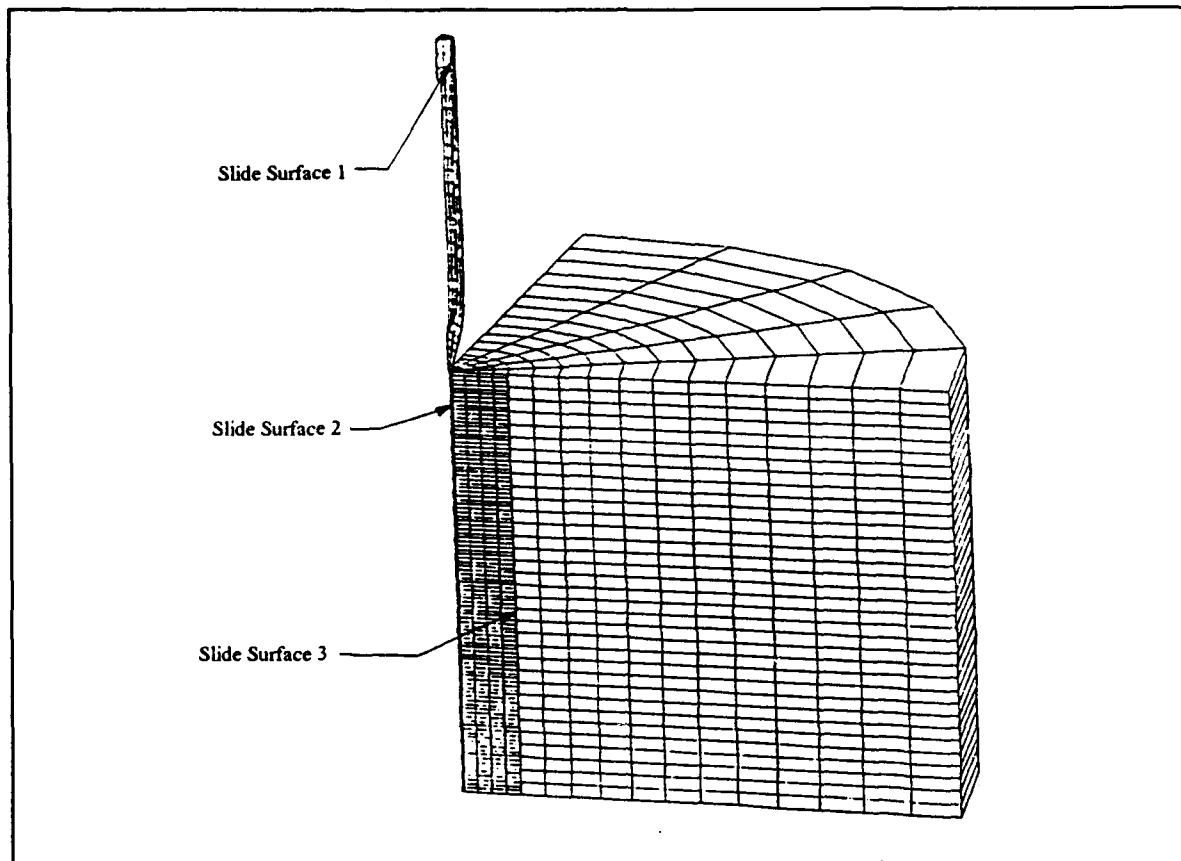


Figure 3
Rainsberger penetration model and location of slide surfaces.

Schwer and Day Simulations. Schwer and Day (1991) have employed DYNA3D for oblique angles of penetrator impact into concrete targets where the penetration path is predetermined using the tunnel method. They also recommend a method called the local modified symmetry constraint technique, where penetration may take any path restricted to a predetermined plane of symmetry within an otherwise arbitrary three-dimensional target medium. (Both the target geometry and target material behavior must be symmetric with the plane of symmetry.) The method reports to work similarly to the tunnel method, in effect exploiting DYNA3D features for releasing symmetry constraints and providing slide surfaces. The simulations presented are remarkable and fully demonstrate the capability of DYNA3D for this class of problem.

Fastener Model Using DYNA3D

A published DYNA2D analysis of fastener projectile penetration by Zhou (1988) was repeated using DYNA3D. The small projectile, shown in Figure 4, was 4 millimeters in diameter, 35 millimeters long, and had a 2.5 caliber radius head with an ogival nose.

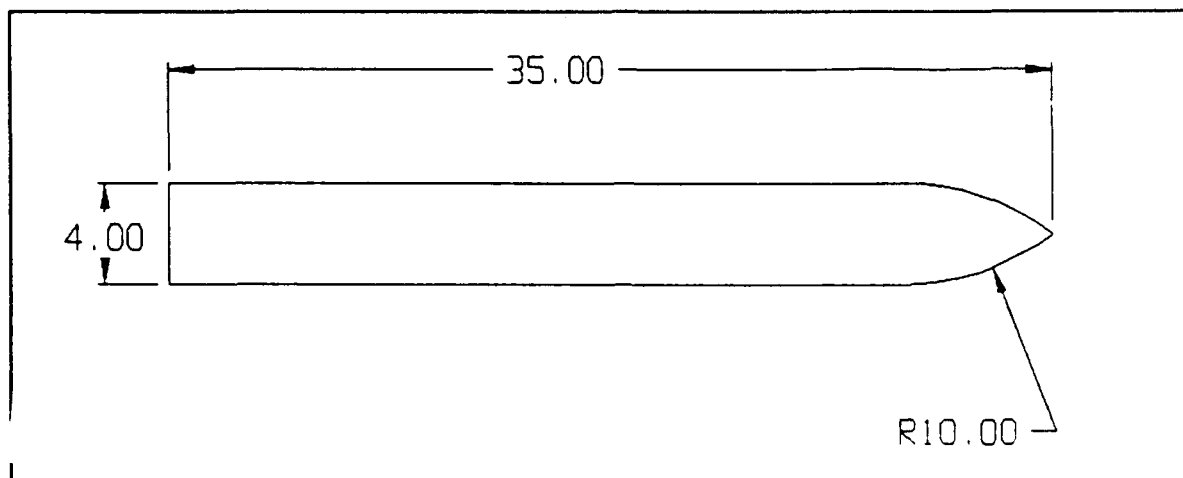


Figure 4
Size of small fastener projectile in millimeters.

The three-dimensional version of Zhou's axisymmetric model contained a frictional sliding interface with voids or gaps permitted to form between the projectile and target. A quarter finite element model was constructed exploiting two planes of symmetry of the axisymmetric configuration. Correspondingly, two planes of symmetry were used in the INGRID input data file to effect the quarter model. The typical INGRID input data file generated for this simulation is presented in Appendix D. The file has been annotated for convenience to the reader as to the meaning of the INGRID commands used. Additional data required for the projectile penetration model had to be reconstructed from Zhou's narrative description since actual input data files for his DYNA2D model were not included in his publication. Consequently the recreated DYNA3D model may not exactly replicate his model.

The projectile was modeled with a small artificial bore hole (0.4 mm in diameter) to effect the formation of a hexahedron element when the plane containing the lines were rotated to make a solid. This is crucial to numerical efficiency of the overall modeling technique because it leads to control of the time step size. The artificial bore does not affect the results since its surface does not come in contact with the target tunnel.

Figure 5 shows the two-dimensional projectile geometry used to generate the three-dimensional geometry for the model. The designated line numbers correspond to numbered line definitions in the INGRID input data file (see Appendix D). This two-dimensional geometry is then rotated about the axis of symmetry to form solid elements. The projectile was divided into a grid 2 elements wide by 24 elements long and then rotated 90 degrees in five successive increments or copies to create 240 eight-node solid elements. Figure 6 shows the initial two-dimensional geometry of the target and projectile together.

Zhou's target was a cylindrical block of rock having both a height and diameter of 150 millimeters. In the corresponding model, the first 15 millimeters were finely zoned to accommodate the large amount of deformation expected in the region. The planar mesh in this zone was 4 elements wide by 102 elements deep and was rotated in five successive increments to form a quarter model of the inner part of the target. The second or outer part of the target was divided into a 12-element-wide mesh with the elements increasing in width with distance from the center. The planar mesh was 34 elements deep and was rotated in five successive increments to form a quarter model of the outside solid portion of the target. The two different

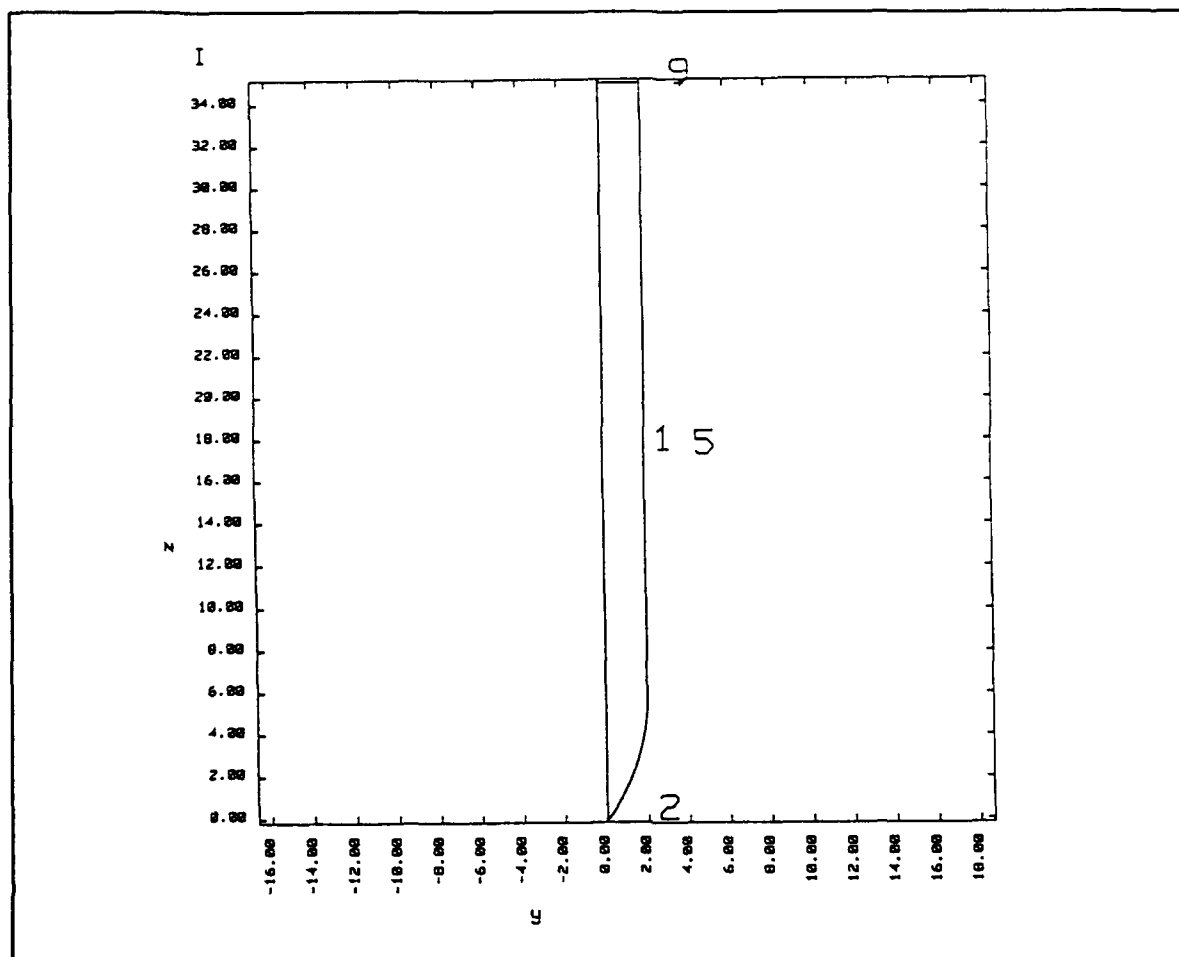


Figure 5

The two-dimensional geometry of the projectile from Zhou's penetration problem. (The line numbers refer to the line definitions in the INGRID input data file. The scales are in millimeters.)

meshes of the target were joined using a tied sliding boundary. No sliding or separation occurs at this boundary; this use of the slide boundary capability in DYNA3D is a convenient and expedient way to avoid dealing with transitional elements in preparing the model. A total of 4,080 eight-node solid elements make up the target model.

The resulting three-dimensional finite element model of the target and projectile was composed of 4,380 eight-node solid elements, and is shown in Figure 7. The bottom nodes of the target model were restrained against displacement.

A small artificial tunnel (1.4 mm diameter) was introduced at the centerline of the target. The tunnel reduced the risk of extreme distortion of the elements in the target. This in turn facilitates the use of the Lagrangian approach for describing material deformation by avoiding having to remesh the model. Once introduced, the size of the tunnel will significantly affect the computer time required; a large tunnel diameter uses less computer time than a small tunnel diameter. This is because explicit finite element computer programs such as DYNA3D cannot step forward in the time integration procedure for solving the equations of motion any faster than the smallest element allows. For the integration to remain stable, the time step size must remain

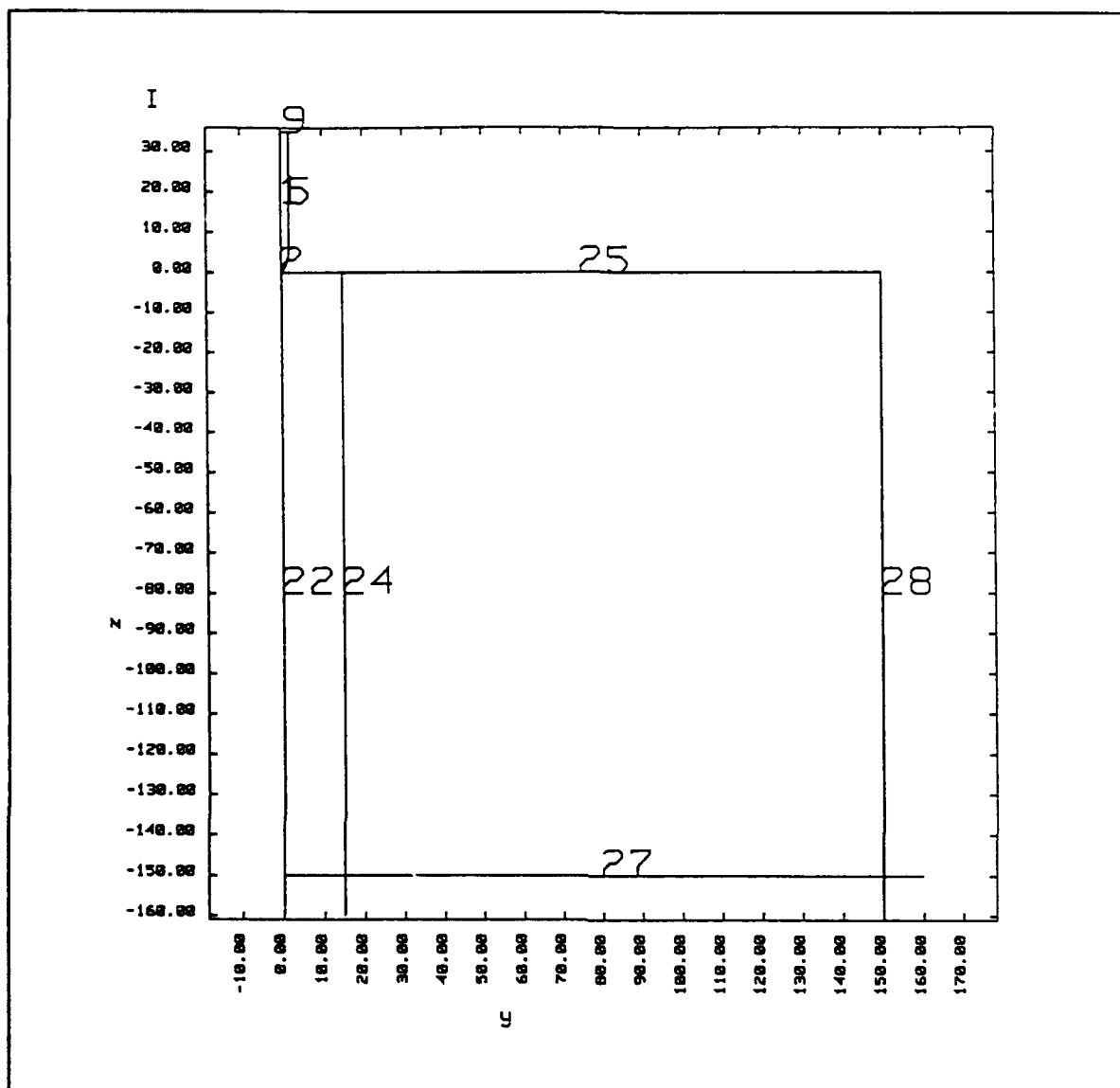


Figure 6
Two-dimensional representation of the projectile and target from Zhou's penetration problem. (The line numbers refer to the definitions in the INGRID input file. The scales are in millimeters.)

smaller than the transit time of an elastic wave traversing the smallest element in the model. However, the effect of the size of the artificial tunnel on computational results is of concern and was also addressed by Schwer et al. (1988). It is important to determine this effect and it will be addressed later in this report as well.

A sliding interface was introduced between the areas of contact of the target and projectile. This interface was assigned a frictional value of zero (the value used by Zhou), and gaps or voids were allowed to form during the simulation.

Material properties for rock were sought from the literature to support development of the numerical model. Published values for rock media vary significantly. Some published mechanical properties for rock are compiled in Table 1. Soft and hard sandstone, and vesicular

and intrusive basalt materials are included. The data developed by Goldsmith and Zhou (1989) were used in the numerical penetration model in the present study. The material properties used for modeling the steel projectile anchors are listed in Table 2.

The steel projectile material behavior and rock target material behavior were both modeled using DYNA3D Material Model #3, an elastic-plastic material model with isotropic or kinematic hardening. Specific parameter values used for the projectile and target material models are given in Tables 3 and 4, respectively. As nearly as can be determined, these values were used in the axisymmetric model by Zhou, who used DYNA2D's version of Material Model #3. The uniaxial stress-strain curve shown in Figure 8 depicts elastic-plastic material behavior for kinematic hardening ($\beta = 0$) and isotropic hardening ($\beta = 1.0$). Kinematic hardening was assumed for both the projectile and the target.

A typical set of data plots and graphs of results from the simulation is shown in Figures 9 through 11. Appendix E contains information on a sample session for pre-processing, executing, and post-processing a projectile anchor penetration simulation using, respectively, INGRID, DYNA3D, and TAURUS. The TAURUS batch file used to create the plots and graphs in Figures 9 through 11 is given at the end of Appendix E. The INGRID input data file can be found in Appendix F where it is labeled as try#18.

The results from the DYNA3D model were near the expected values for the maximum depth of penetration. Zhou reported a depth of penetration of 20 mm as shown in Figure 12(a). In both cases, the initial impact velocity was 100 m/s. The DYNA3D simulation computed a maximum depth of 15 mm as shown in Figure 10(a). This represents a 25 percent difference between the two simulation models. In a displacement-based finite element formulation, the exact displacement solution is always approached monotonically from below, though reduced integration (see Appendix C) mitigates this argument. In this case, the DYNA2D simulation must be regarded as more accurate since the configuration modeled is axisymmetric. Therefore, that the DYNA3D displacement is less than the DYNA2D displacement is somewhat as expected.

Other differences between the DYNA2D and DYNA3D simulation results involved the amount of rebound and final velocity of the projectile. The reported velocity for the DYNA2D simulation reversed and approached a zero residual value, and the reported rebound of the projectile was less than 10 mm. The velocity for the DYNA3D simulation also reversed but approached a nonzero steady state residual value causing the projectile to back out of the cavity. This was apparently due to residual cavity pressure acting on the ogival nose of the projectile and the absence of friction.

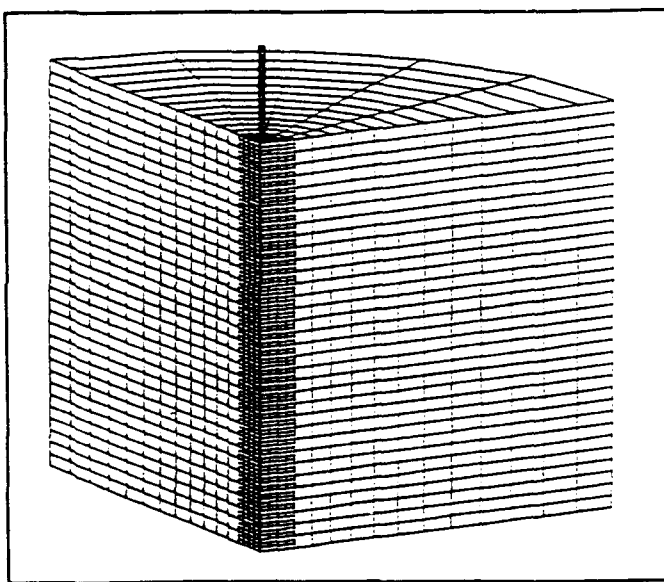


Figure 7
DYNA3D finite element penetration model
for fastener projectile.

Table 1
Mechanical Properties of Rock Materials

Reference Source	Density (kg/m ³)	Young's Modulus (GPa)	Poisson's Ratio	Porosity (%)	Ultimate Compressive Strength (MPa)	Ultimate Tensile Strength (MPa)
Rock Type: Soft Sandstone						
Beard (1984)	2231	-	-	-	10.13	-
Stowe (1984)	2291	4.896	0.35	20.7	15.24	0.161
Goldsmith & Zhou (1989)	2164	4.4	-	-	23.37	-
Zhou (1988)	2130	13.62	0.20	18.0	45.00	4.55
Brunette & Goldsmith (1989)	1940	0.35	-	-	7.05	-
Rock Type: Hard Sandstone						
Wadsworth & Beard (1980)	2600	26.4	0.01	-	146.5	-
Goldsmith & Zhou (1989)	2588	47.34	-	-	122.	-
Brunette & Goldsmith (1989)	2500	4.98	-	-	124.	-
Rock Type: Vesicular Basalt						
Wadsworth & Beard (1980)	2167	7.29	0.167	30.	33.13	-
Beard (1984)	2325	26.24	-	-	17.31	-
Goldsmith & Zhou (1989)	2248	26.24	-	26.	40.4	-
Brunette & Goldsmith (1989)	2970	8.29	-	-	123.	-
Rock Type: Intrusive Basalt						
Beard (1984)	2710	-	-	-	50.48	-
Stowe (1984)	2662	34.48	0.15	7.0	87.08	-
Goldsmith & Zhou (1989)	2798	51.88	-	-	99.93	-
Brunette & Goldsmith (1989)	2500	3.53	-	-	56.3	-

Table 2
Material Properties of AISI 4340 Steel

Density	7832 kg/m ³
Young's Modulus	200 GPa
Yield Strength	310-793 MPa
Tensile Strength	552-2000 MPa

Table 3
Projectile Material Properties for Material Model #3

Density	7.8E-6 kg/mm ³	(7800 kg/m ³)
Young's modulus, E	209E6 kg/(mm·s ²)	(209 GPa)
Poisson's ratio	0.3	
Uniaxial yield stress, σ_0	1.2E6 kg/(mm·s ²)	(1.2 GPa)
Tangent modulus, E_T	1E6 kg/(mm·s ²)	(1.0 GPa)
Hardening parameter, β	0	

Table 4
Target Material Properties for Material Model #3

Density	2.13E-6 kg/mm ³	(2130 kg/m ³)
Young's modulus, E	13.62E6 kg/(mm·s ²)	(13.62 GPa)
Poisson's ratio	0.2	
Uniaxial yield stress, σ_0	0.026 kg/(mm·s ²)	(0.02 GPa)
Tangent modulus, E_T	0	
Hardening parameter, β	0	

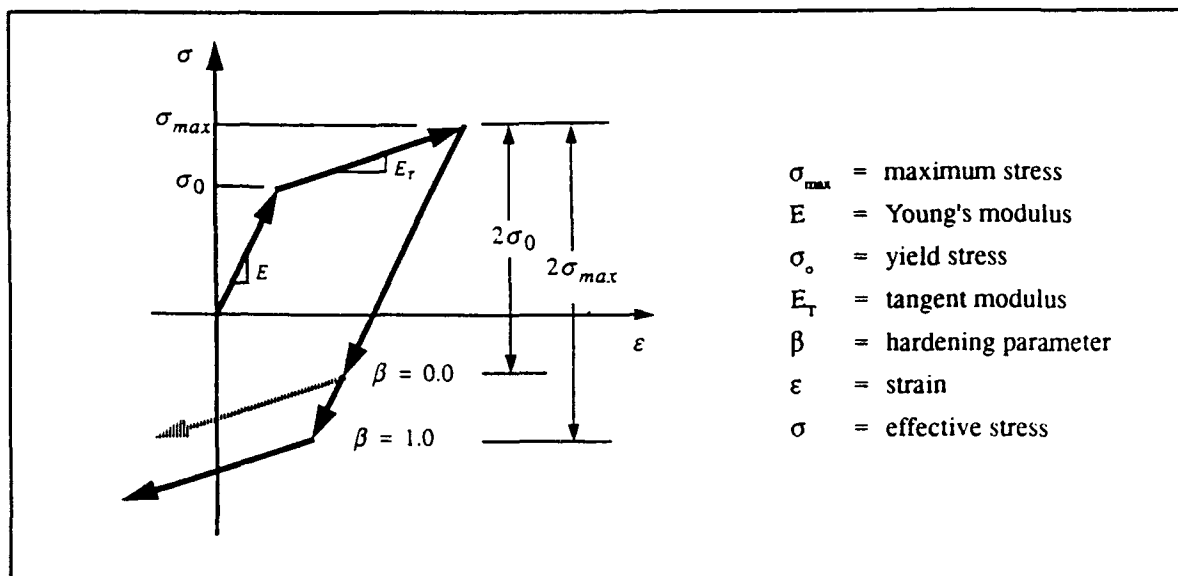


Figure 8
Uniaxial stress-strain curve showing elastic-plastic material
behavior for kinematic hardening ($\beta=0$) and isotropic hardening ($\beta=1$)
(Hallquist and Whirley, 1991).

Without friction between the projectile and target, and with a zero value prescribed for the target hardening modulus, the problem as modeled is physically unrealistic. The noted differences in results may also be due to misinterpretation of Zhou's model. Again, the results of the DYNA3D model should be expected to approach those for the DYNA2D model as the three-dimensional mesh is refined around the perimeter of the model. In this respect, the DYNA3D model must be viewed only as an approximation to the DYNA2D model. The differences noted between the results of these two simulations otherwise are not explained.

The computer processing time for a 0.5-ms DYNA3D simulation on the Sun 4/260 workstation was approximately 45 hours. The amount of computer time on this simulation is excessive for two reasons. First, the projectile had reached a steady state condition within approximately 0.25-ms. Thus, the simulation could have been terminated with no loss of useful data much earlier. Second, the number of elements in the target model was excessive. This was because most of the elements that experienced significant pressure were within 5 projectile radii of the centerline (Figure 11). A similar result was noted by Schwer et al. (1988). The finite element model needlessly extended well beyond this range. It is therefore surmised that a satisfactory simulation could have been obtained by halving the duration and using a substantially reduced finite element model of the target.

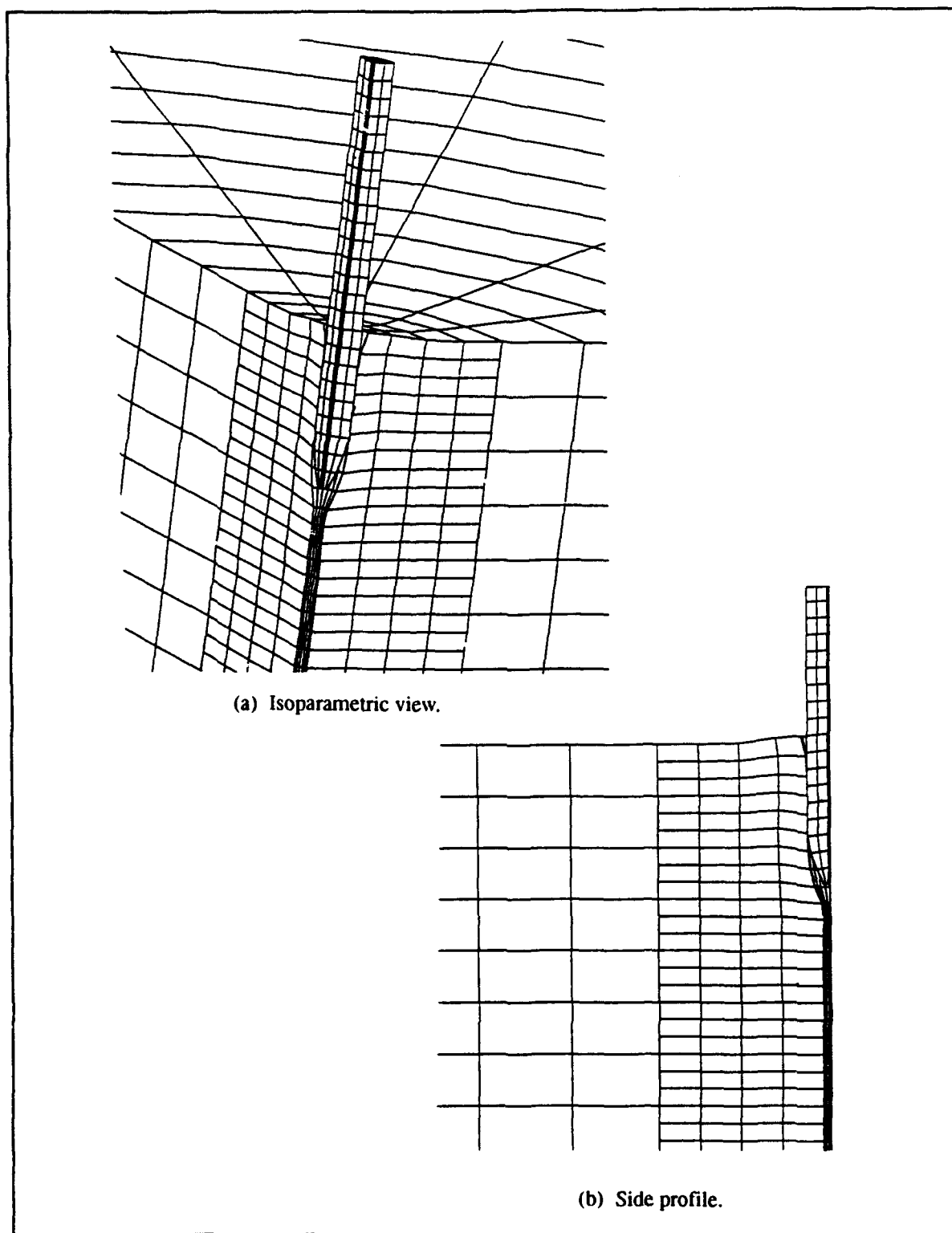


Figure 9
Projectile embedded in the target at end of the simulation.

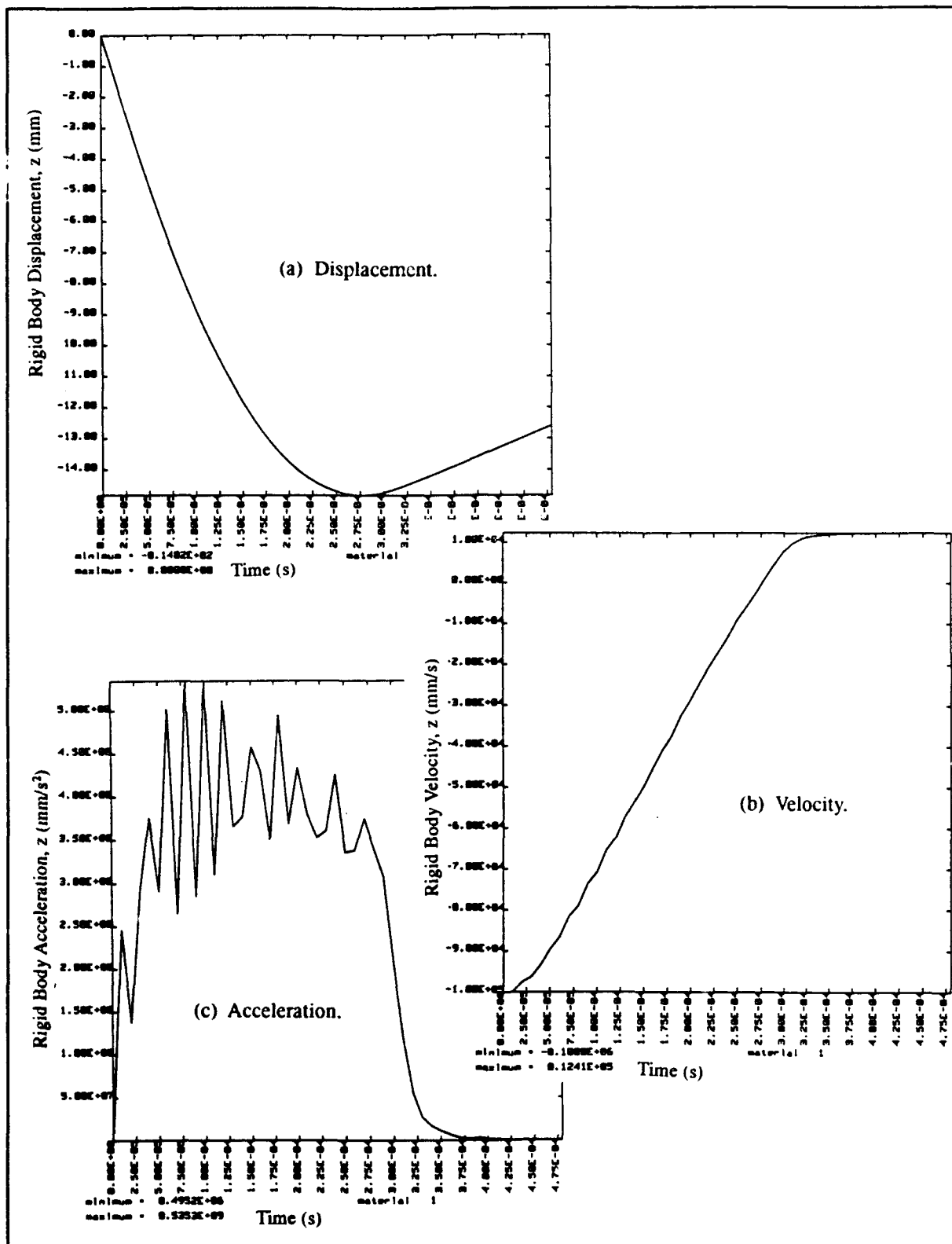
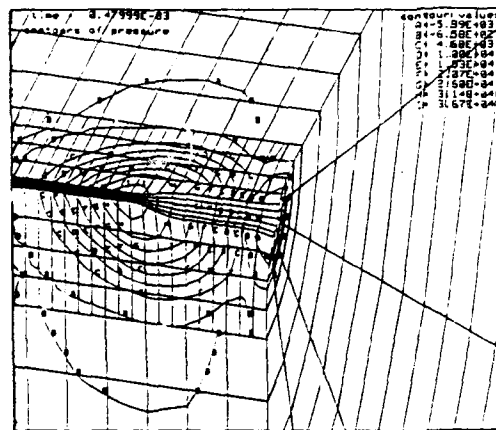
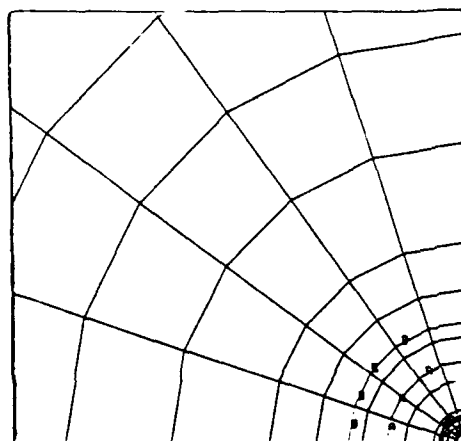


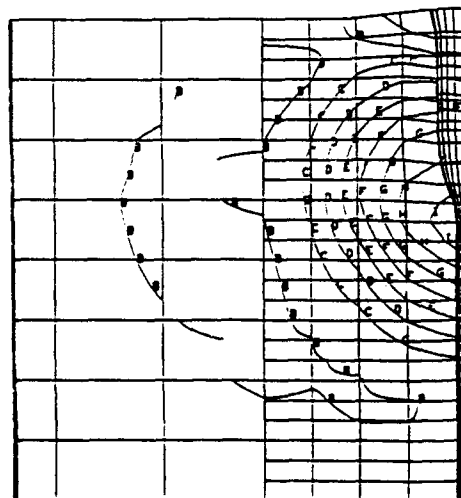
Figure 10
Projectile response from DYNA3D.



(a) Isometric view.

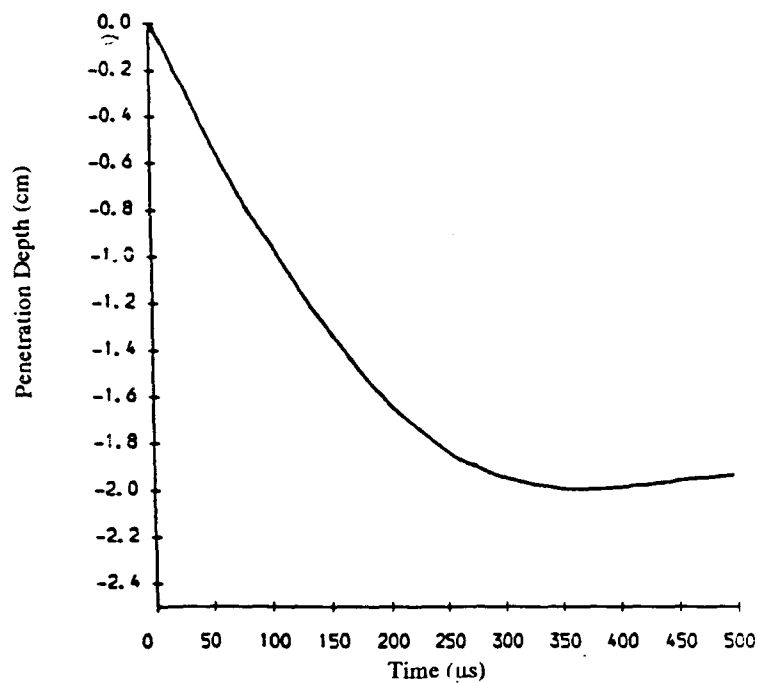


(b) Top view.

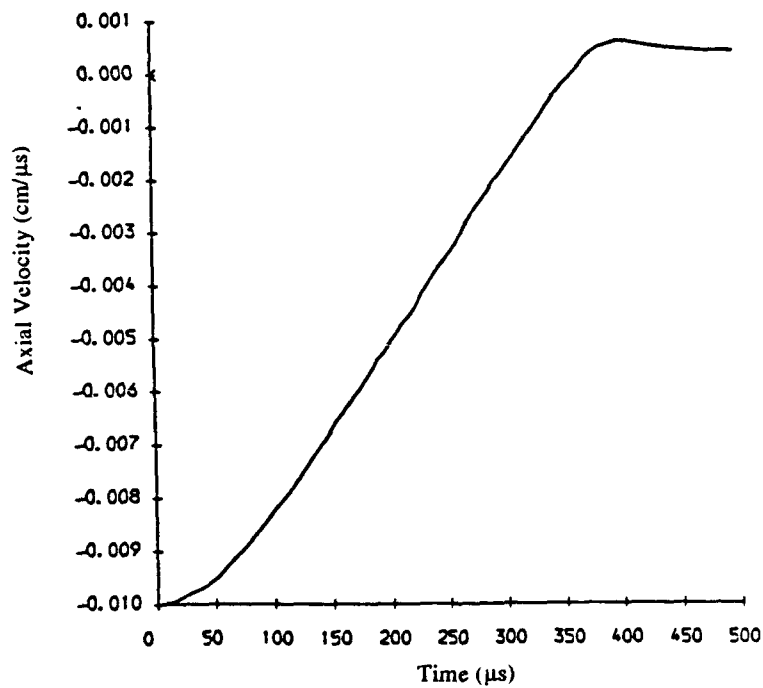


(c) Side view.

Figure 11
Contours of residual pressure in the target.
(Units for the pressure are $\text{kg}/(\text{mm} \cdot \text{s}^2)$)



(a) Displacement.



(b) Velocity.

Figure 12
Projectile response from DYNA2D (Zhou, 1988).

NUMERICAL MODEL TECHNIQUE AND DEMONSTRATION

The basic DYNA3D numerical model discussed in the previous section was exercised further to evaluate the effects of various modeling parameters. The parameter study would help verify the numerical model by investigating areas of uncertainty that were raised during the preliminary analysis and the literature review, such as artificial tunnel size, effect of friction, material model selection, and amount of strain hardening. After the parameter study, the geometry for the model was changed to reflect a larger anchor projectile for rock anchor penetration simulation.

Parameter Study

Effect of Target Tunnel Diameter. The effect of artificial tunnel size was addressed by Schwer (1988) in DYNA2D models. An upper limit on the tunnel diameter which minimizes computation time and maintains accuracy is perhaps even more meaningful for DYNA3D applications than for DYNA2D applications because of higher compute times in three dimensions. A suitable range for the tunnel diameter was sought which would not compromise simulation results and would minimize computation time. The diameter of the tunnel was varied in five runs to determine how it affects the computed response. (In Appendix F these runs correspond to INGRID input data files labeled try #7, 8, 9, 15, and 16.) The hardening modulus used for these simulations was one percent of Young's modulus, and the coefficient of friction used between the projectile and the target was 0.1 as suggested by Goldsmith and Zhou (1989).

Figure 13 shows the computed response of the projectile for various tunnel diameters. The displacement histories show various amounts of projectile rebound associated with the various tunnel diameters. The smallest diameter causes the largest rebound of the projectile. Rebound was not discussed in the previous DYNA studies reviewed. However, the amount of rebound is of interest because the residual penetration depth can clearly play a significant role in predicted anchor holding capacity. The projectile velocity neared a steady state velocity of 20 m/s upward for the smallest tunnel case, and was still rebounding when the simulation was manually terminated. For all the larger tunnels, the projectile came to rest at various rebound depths.

The acceleration history also varied significantly with target tunnel diameter. Mechanical failures of anchor systems have been associated with high deceleration rates. Thus, these data are important to development of modeling technique. Larger diameter tunnels result in lower computed values for projectile deceleration. Also, since the 0.40-mm and 1.02-mm tunnel simulations are similar, a lower limit for the tunnel diameter in this range is suggested at which higher deceleration will not occur for the specific problem modeled.

The contours of pressure shown in Figure 14 provide insight into the fundamental cause of projectile rebound. These data are shown at 0.5 ms into the simulation, the point where the projectile generally had come to rest. They may be regarded as residual pressures in the target material. The largest positive (compressive) pressures occur near the ogival nose of the projectile, where force is mobilized to push the projectile back out of the cavity. Smaller diameter tunnels lead to larger contact areas on the nose of the projectile over which the residual pressures act, and, thus, a larger force is mobilized to push the projectile back out of the cavity. The deformation of the tunnel is not as pronounced in Figure 14(e) and the force mobilized is small when compared to the case shown in Figure 14(a) where a well-pronounced cavity has

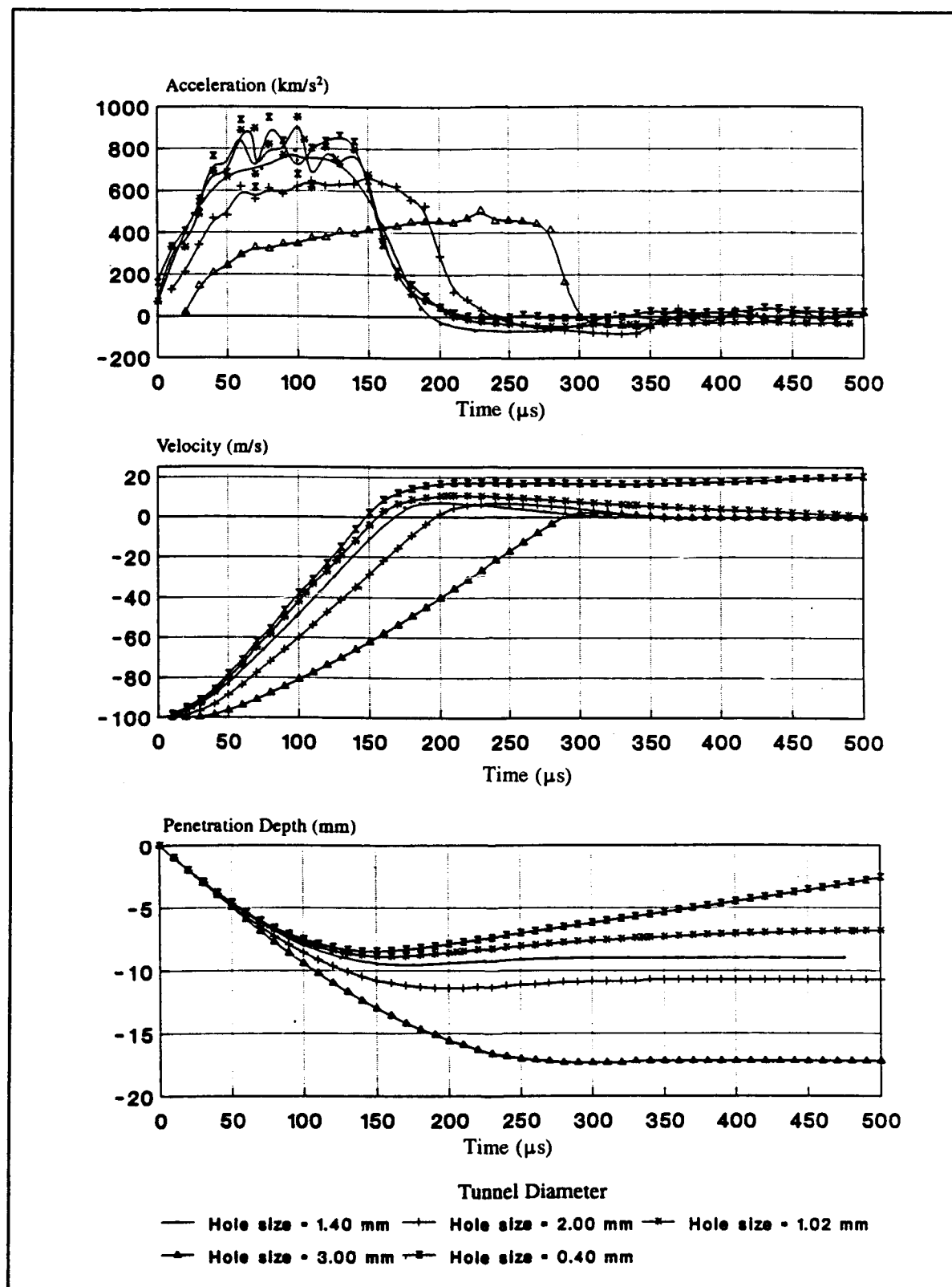


Figure 13
Effect of target tunnel diameter on penetration depth, velocity, and acceleration.

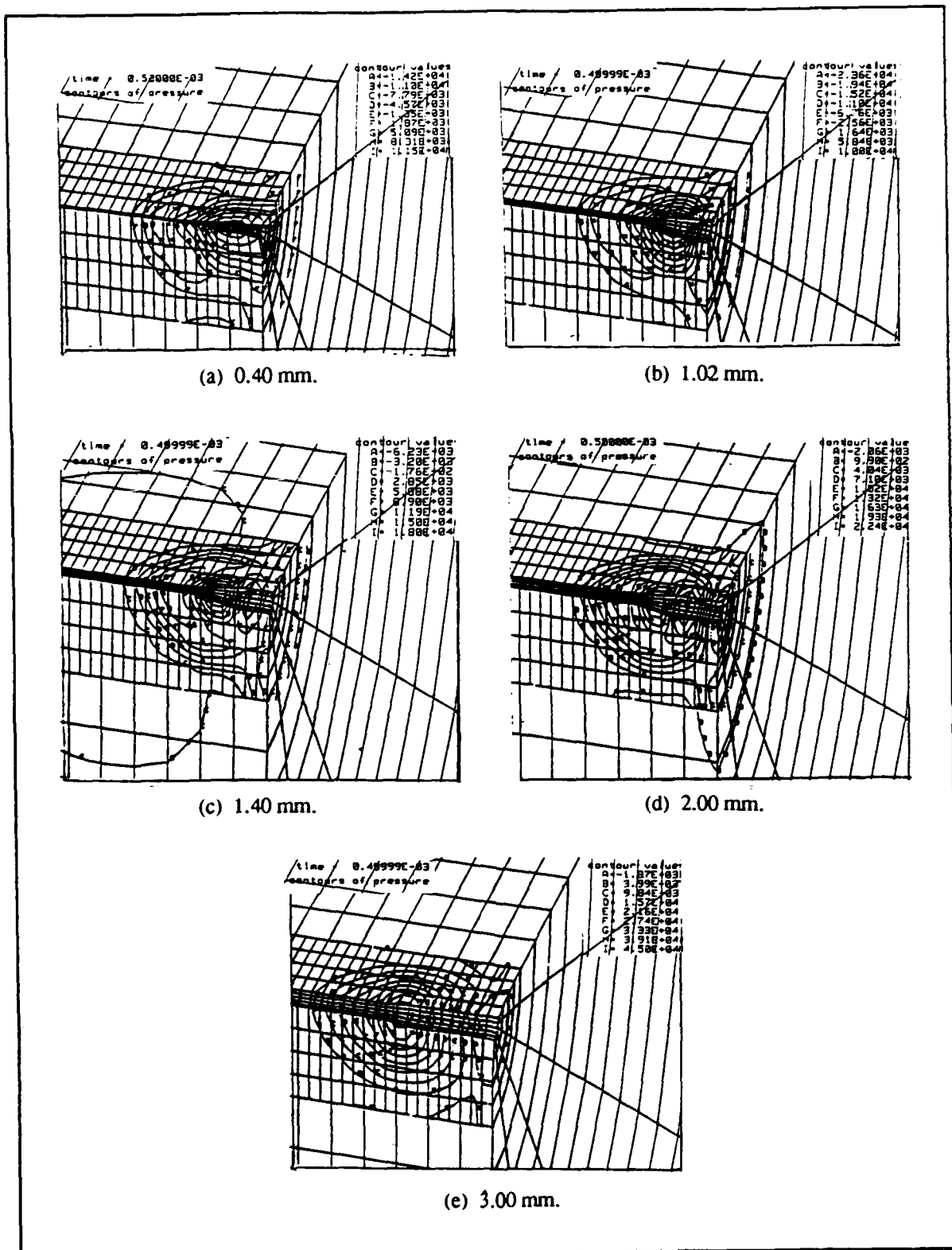


Figure 14
Residual pressure contours in the target for various tunnel diameters.
(Units for contour values are $\text{kg}/(\text{mm} \cdot \text{s}^2)$)

formed. The force causing rebound is eventually offset by the friction force which opposes rebound, and the projectile finally comes to rest in the case of the three larger tunnels.

The effect of the tunnel diameter on penetration depth was non-dimensionalized by dividing the tunnel diameter by the projectile diameter to facilitate a useful definition of an upper limit for the tunnel diameter. Figure 15 shows the effect of the ratio on the maximum penetration depth. As the ratio approached zero, the slope of the curve approached zero. These data indicated that a reasonable upper limit for the ratio was 0.25. Consequently, as long as the artificial tunnel diameter remains one quarter or less of the projectile diameter, the DYNA3D penetration model should be sufficiently insensitive to the presence of an artificial tunnel. The ratio of 0.25 appears to be an optimal balance between accuracy and computation time for DYNA3D simulations of anchor penetration into rock materials. Schwer and Day (1991) report that a ratio of 0.4 or less does not affect the penetrability of the target model when using DYNA2D. That standard applied to the present DYNA3D simulation would lead to a 20 percent error in predicted penetration depth. Thus, the critical target-to-projectile diameter would seem to depend on whether DYNA2D or DYNA3D is being used.

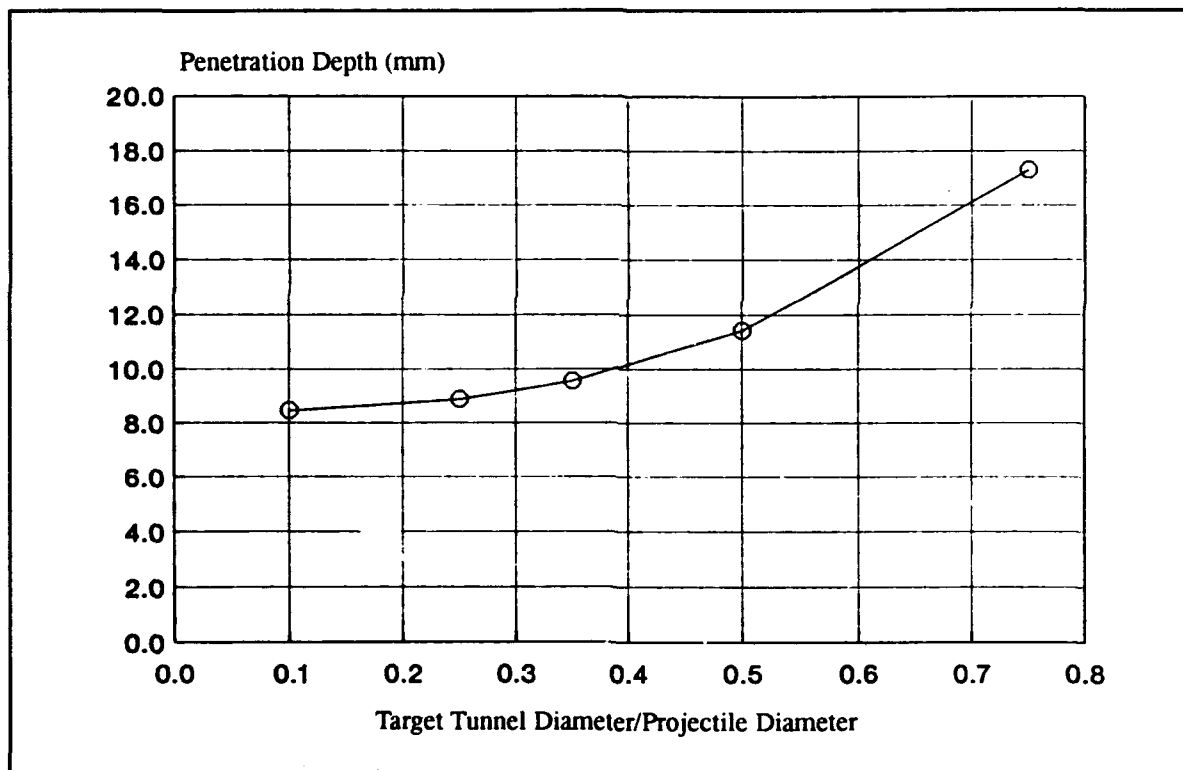


Figure 15
Normalized chart for the effect of the target/projectile diameter ratio on the maximum penetration depth.

Effect of Friction Coefficient. The effect of friction at the projectile/rock interface was studied to develop skill in applying the friction slideline capability in DYNA3D, and to determine the sensitivity of the model to the friction coefficient. Since little is known about the coefficient of friction for rock anchor penetration, and coefficient of friction values vary significantly in the literature, the model's response to different values needed to be quantified. The effect of the friction coefficient prescribed for the sliding interface between the projectile and target was varied from zero to 0.1 in three simulations. The tunnel-to-projectile diameter ratio was held constant. The resulting effect on penetration model response is shown in Figure 16. Predictably, a smaller coefficient of friction results in a larger penetration depth. The variation in maximum penetration depth was approximately 20 percent. However, this diminished to 10 percent or less when rebound was considered and residual penetration depth was the basis of comparison.

The residual rebound velocity for the frictionless case and for the 0.05 coefficient of friction case was nonzero. Had the simulation been allowed to continue, the projectile would have exited the cavity for the frictionless case and perhaps as well for the 0.05 case. These data indicate that only simulations with a coefficient of friction equal to 0.1 or greater would prove useful for anchor extraction studies because static residual conditions are essential to such studies. The residual pressure contour data for this simulation are shown in Figure 14(c).

The data also show that larger values of interface friction result in higher maximum deceleration levels as expected. Further, greater values of interface friction show lesser oscillation in the projectile deceleration graphs. This is perhaps because interface friction reduces relative (tangential) motion between the projectile and rock, and the Type 3 sliding surface algorithm is invoked less often. In doing so, the response of the projectile is smoother. It would be expected that the frequency content of the impact time histories would be higher for the higher friction simulations shown because these impacts are sharper.

Effect of Different Material Models. Various DYNA3D material models were considered in search of a model that would suitably describe material behavior of the rock target. A good material model should allow for the cracking tendency of rock. DYNA3D contains four potential material models for modeling rock targets: kinematic/isotropic elastic-plastic model (#3), a soil and crushable foam model (#5), a concrete/geological model (#16), and a geologic cap model (#25).

In the previous parameter studies, DYNA3D material model #3 was used exclusively. Here the rock target material model was changed to a soil and crushable foam model, DYNA3D material model #5, which can also be used to model rock including tensile cracking. The parameter values used for this model are given in Table 5. These data prescribe a pressure versus volumetric strain graph of the form shown in Figure 17. The values for the yield function constants were obtained from the DYNA2D study by Zhou (1988) which intended to replicate sandstone targets. Material model #3 was again used for the projectile (Table 3 and Figure 8).

Unfortunately material model #5 failed to provide a useful penetration model with a sandstone target when using the parameter values described. As shown in Figure 18, the target material displaced away from the projectile. These results would not be useful in conjunction with anchor extraction studies because no condition of confinement was predicted. A comparison of the penetration model response for material models #3 and #5 is shown in Figure 19. Overall, the results are similar. Material model #5 constituted a softer target and allowed approximately 10 percent more penetration, and the projectile reached a small positive steady state velocity and

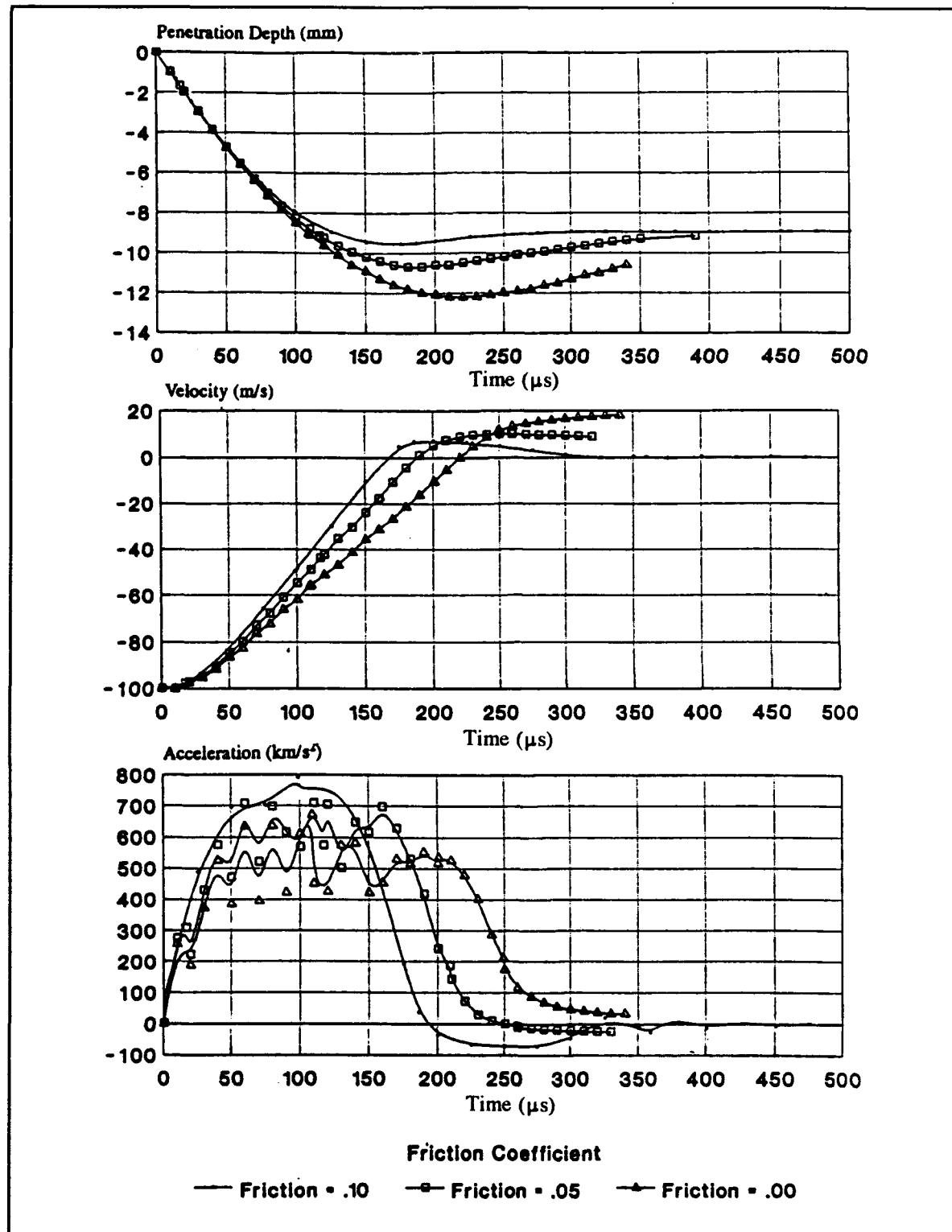


Figure 16
Effect of friction coefficient on projectile penetration depth,
velocity, and acceleration.

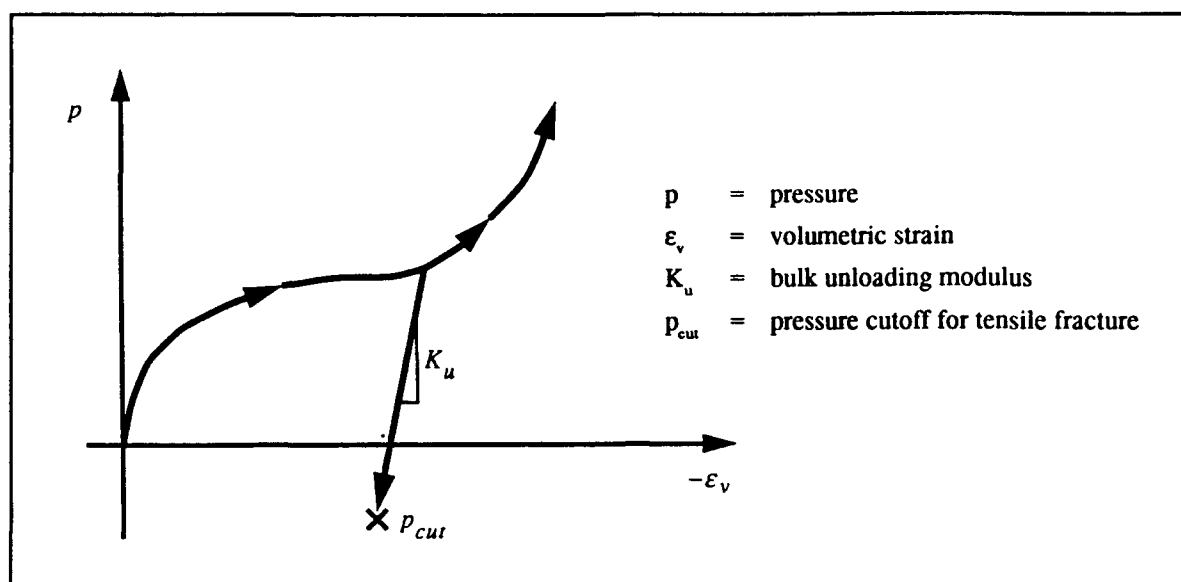


Figure 17
Pressure versus volumetric strain curve for soil and crushable foam material model (Whirley and Hallquist, 1991).

Table 5
Target Material Properties for Material Model #5

Density	2.13E-6 kg/mm ³	(2130 kg/m ³)
Shear modulus	5.68E6 kg/(mm·s ²)	(5.68 GPa)
Bulk unloading modulus, K_u	11.25E6 kg/(mm·s ²)	(11.25E6 GPa)
Yield function constant 0	1.33 kg/(mm·s ²)	
Yield function constant 1	60,270 kg/(mm·s ²)	
Yield function constant 2	0	
Pressure cutoff for tensile fracture, p_{cut}	0	
No. of points on the p vs. ϵ_v curve	6	
Volumetric strain values, ϵ_v	0 .0025 .01 .04 .05 .055	
Corresponding pressure values, p	0 15000 21250 34000 41300 50000	

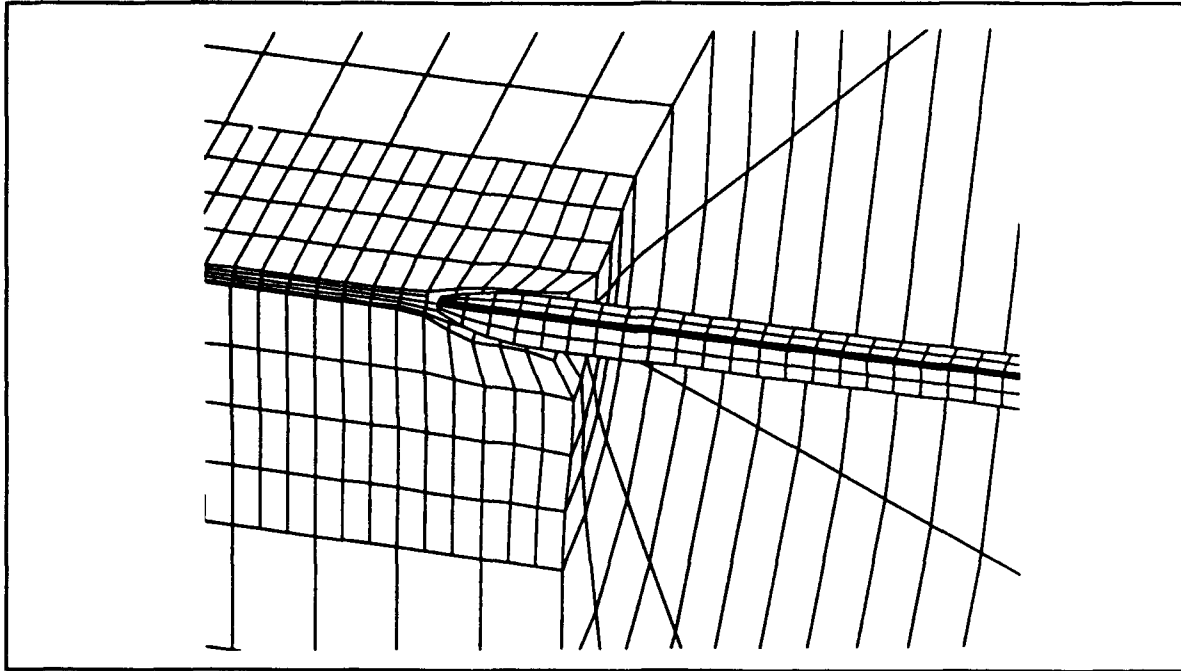


Figure 18
Projectile embedded in target characterized by material model #5.

was backing out of the cavity. The projectile acceleration response is very similar for material models #3 and #5.

In further attempts with material #5, an error was encountered when trying to assign any value other than zero to the pressure cutoff for tensile fracture; a small negative value of ten and a small positive value of ten encountered run-time errors. DYNA3D material models #16 and #25 were not considered in this study. Future rock anchor penetration studies should investigate these models as well.

Effect of Hardening Modulus. Using material model #3 and DYNA2D, Zhou (1988) reported a 25 percent reduction in penetration depth when using zero hardening instead of 0.5 percent of Young's modulus for the hardening modulus value. Therefore, the hardening modulus in material model #3 was varied to see if a similar reduction occurred in a DYNA3D simulation. Goldsmith and Zhou (1989) suggested using a nominal value of 1.0 percent of Young's modulus for the hardening parameter. The hardening modulus (or tangent modulus, E_T , in Figure 8) clearly increases the resistance of the target, and a reduction in penetration depth is anticipated with higher values. It is expected to be a critical material model parameter in modeling penetration.

The tangent modulus for this study was set at zero and 1.0 percent of Young's modulus for two successive simulations. The material properties used for the target (see Table 4) were otherwise unchanged. The coefficient of friction between the projectile and target was 0.1.

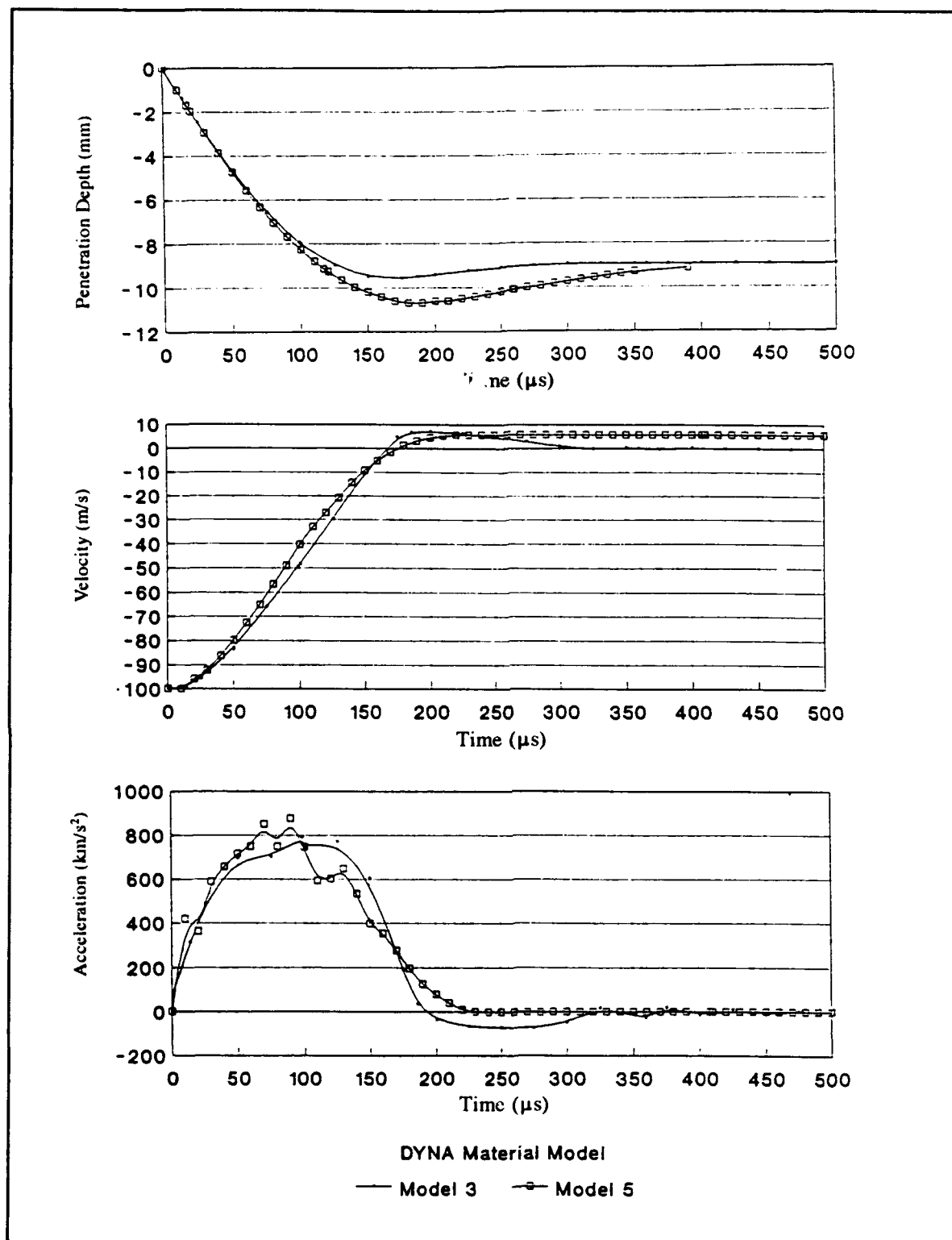


Figure 19
 Effect of rock target material models on projectile penetration depth, velocity, and acceleration.

Figure 20 compares the penetration response for different values of target hardness. The penetration depth was about 25 percent less for the hardening modulus value of 1.0 percent of Young's modulus compared to no hardening. The maximum deceleration of the projectile was correspondingly greater since the penetration depth decreased. Corresponding residual pressure contours in the rock target are shown in Figure 21. These data show that the average direct residual stress (residual pressure) on the projectile is higher for the lower hardening modulus.

Larger Anchor Projectile Study

The penetration model for a larger anchor projectile was constructed from knowledge gained in replicating Zhou's small fastener penetration model and from the aforementioned parameter study. The larger projectile was 2.54 cm in diameter and 17.78 cm long. The ogival nose is defined by the ratio between the nose arc's radius and the projectile diameter; in this case, the caliber radius head was 3.0. A sketch of the projectile is shown in Figure 22. The following description of the construction of the DYNA3D penetration model for the larger projectile is included for completeness.

Construction of the finite element model of the projectile was facilitated by including a small artificial bore 0.508 cm in diameter at the center. This prevented very small hexahedron solid elements from being formed in the development of the projectile model. The projectile was divided into a grid 2 elements wide by 14 elements long and then rotated 90 degrees about the projectile centerline in five successive increments to create 140 eight-node solid elements which constitutes a one-quarter solid model of the projectile. The material behavior of the steel projectile was modeled using an elastic-plastic material model (DYNA3D model #3). The parameter values used for this material model are given in Table 6.

The target was modeled as a cylindrical block having a depth of 63.5 cm and a radius of 25.4 cm. To promote reasonable computer run times, a small artificial tunnel 0.635 cm in diameter was introduced along the centerline of the target. This corresponds to a tunnel-to-projectile diameter ratio of 0.25, which was found to be an optimum value in the preliminary study. The inner part (the first 10.16 cm along the radius) was finely zoned to accommodate substantial deformation gradients. The grid for this zone is 4 elements wide by 100 elements deep and was rotated in five successive increments to form a one-quarter solid model of the target. The outer part of the target was divided into a 3 by 25 mesh with the element size increasing by a factor of two for each increment from the center outward. The two different meshes of the target were joined using a tied sliding boundary. No sliding or separation was permitted at this interface. A total of 2,375 eight-node solid elements made up the one-quarter solid model of the target.

The base of the target model was restrained against displacement. Target material behavior was modeled as an elastic plastic material (DYNA3D model #3) using the parameter values listed in Table 7. A nominal value of 1 percent of Young's modulus was used for the tangent modulus as suggested by Goldsmith and Zhou (1989).

A sliding interface was employed between the target and projectile. This interface was assigned a coefficient of friction value of 0.1 and permits development of gaps or voids during the simulation. The DYNA3D penetration model for the larger anchor projectile is constituted of 2,515 eight-node solid elements, and is shown in Figure 23.

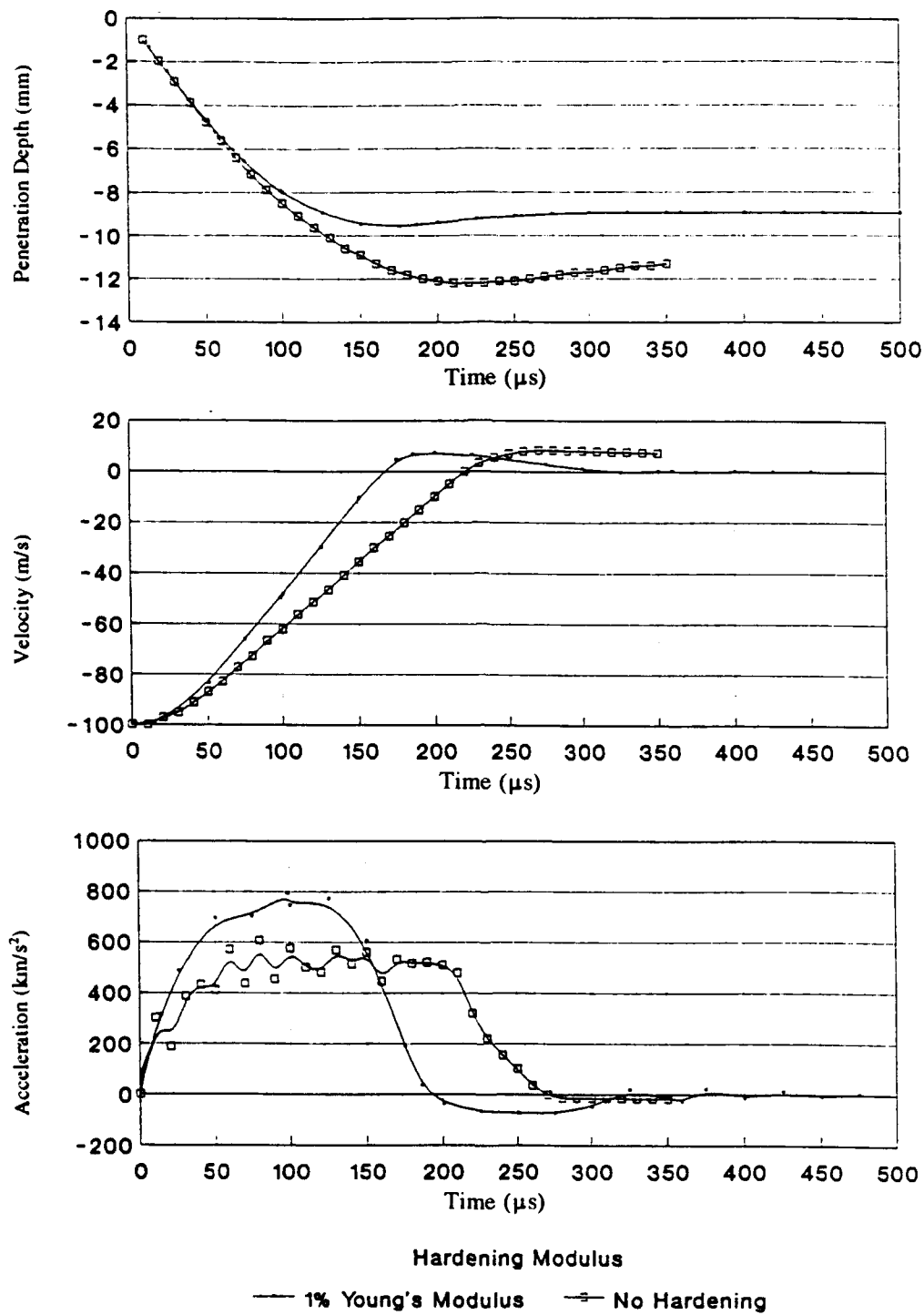
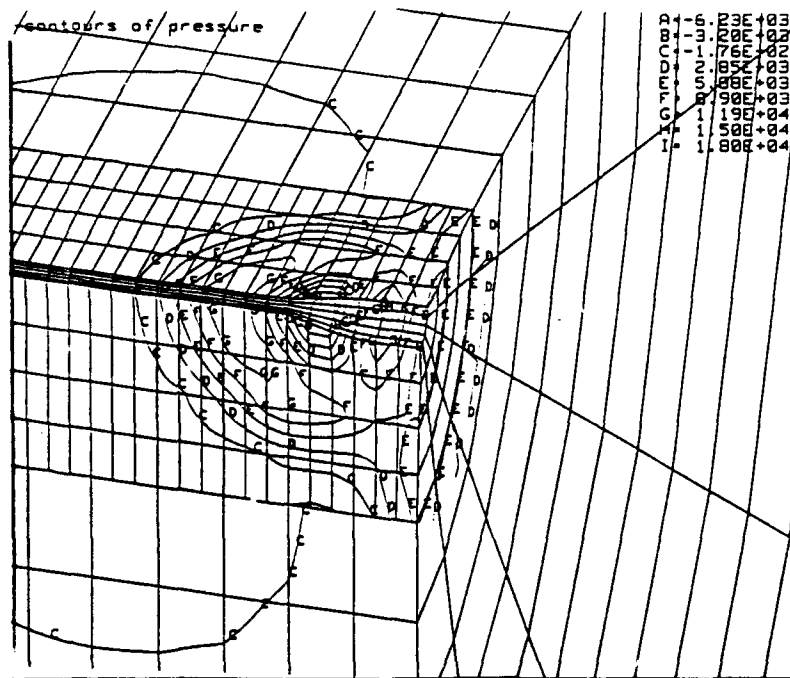
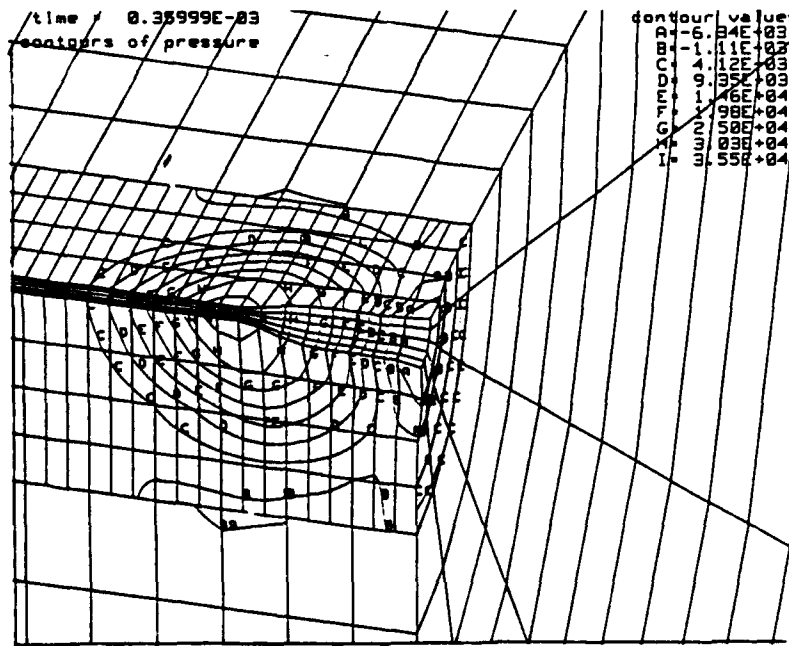


Figure 20
Effect of target hardening modulus on projectile penetration
depth, velocity, and acceleration.



(a) 1% of Young's modulus.



(b) Hardening modulus of zero.

Figure 21
Contours of residual pressure in the target for varying hardening modulus values.
(Units are $\text{kg}/(\text{mm} \cdot \text{s}^2)$)

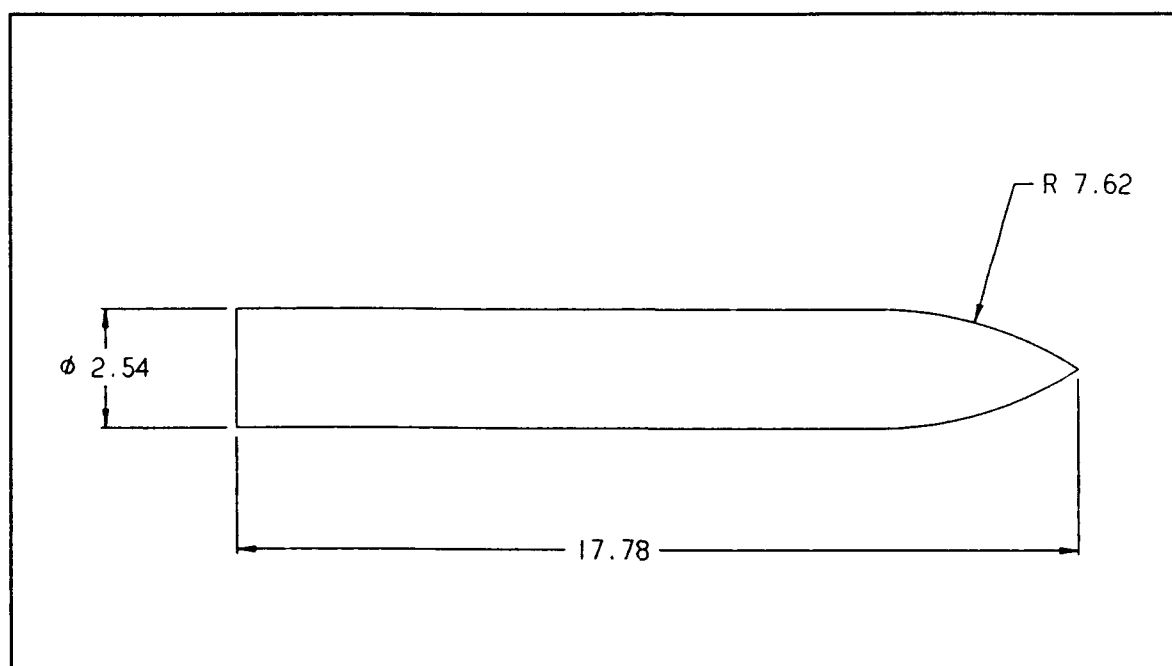


Figure 22
Larger anchor projectile. (Dimensions are in centimeters)

Table 6
Projectile Material Properties for
the Larger Anchor Projectile

Density	7.80 g/cm ³	(7800 kg/m ³)
Young's modulus	2.00E12 g/(cm·s ²)	(200 GPa)
Poisson's ratio	0.3	
Uniaxial yield stress	17.9E9 g/(cm·s ²)	(1.79 GPa)
Tangent modulus	10.0E9 g/(cm·s ²)	(1.0 GPa)

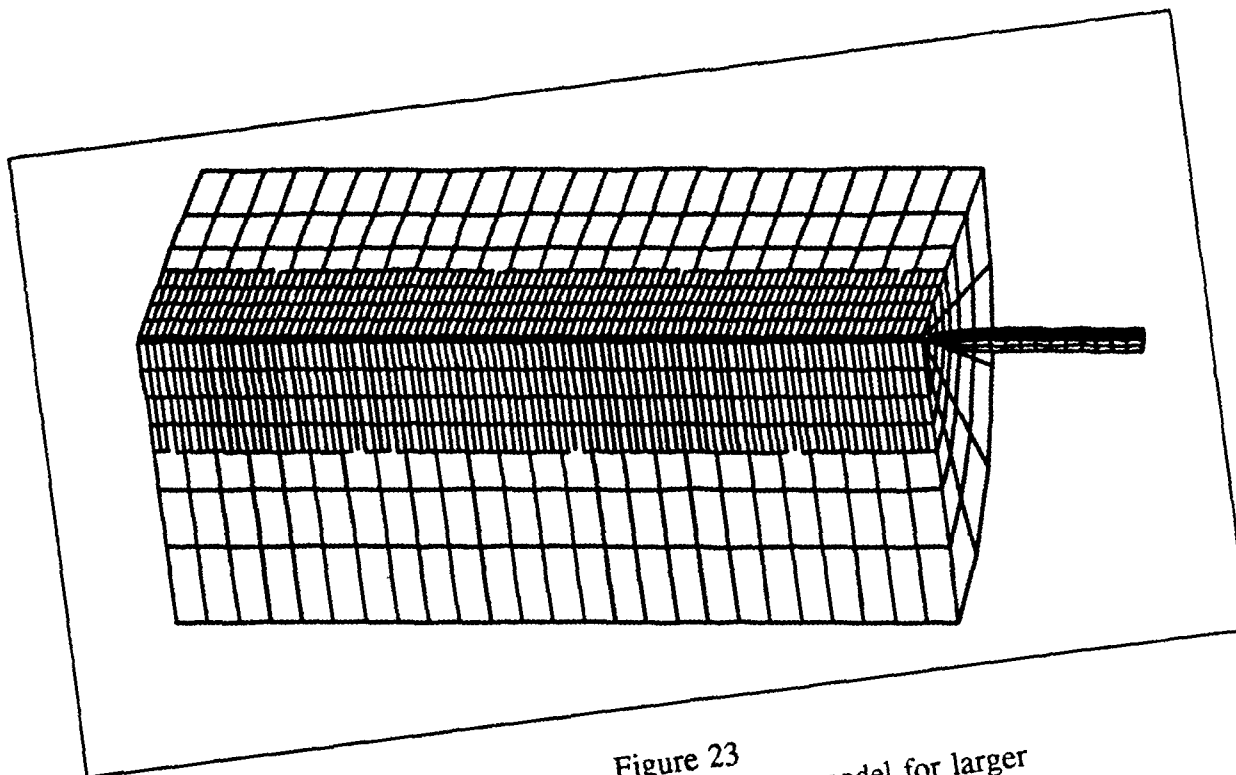


Figure 23
DYNA3D finite element penetration model for larger
anchor projectile.

Table 7
Target Material Properties for
the Larger Anchor Projectile

Density	2.16 g/mm ³	(2160 kg/m ³)
Young's modulus	44.E9 g/(cm·s ²)	(4.4 GPa)
Poisson's ratio	0.3	
Uniaxial yield stress	.234E9 g/(cm·s ²)	(.0234 GPa)
Tangent modulus*	.440E9 g/(cm·s ²)	(.0440 GPa)

*A nominal value of 1% of Young's modulus was used for the
tangent modulus as suggested by Goldsmith and Zhou (1988).

Computer run times on the Sun 4/260 workstation rated at 11 mips were approximately 18 hours, a reduction of over 50 percent in compute time from the DYNA3D model (Figure 7) of Zhou's penetration problem. The reduction was achieved by halting the simulation when the projectile came to rest, and also by having reduced the number of elements in the model in the radial direction. Further reduction could be achieved by truncating the mesh in the vertical direction as well.

In a subsequent simulation, the target material characterization was modeled with DYNA3D material model #5 so that the differences between the two material models for the target could again be assessed. The parameter values used for this model are listed in Table 8.

Table 8
Target Material Properties Used With Material
Model #5 for the Larger Anchor Projectile

Density	2.16 g/cm ³	(216 kg/m ³)
Shear modulus	8.44E10 g/(cm·s ²)	(8.44 GPa)
Bulk unloading modulus	11.25E10 g/(cm·s ²)	(11.25 GPa)
Yield function constant 0	.00133E-7 g/(cm·s ²)	
Yield function constant 1	60.27 g/(cm·s ²)	
Yield function constant 2	0	
Pressure cutoff for tensile fracture, ρ_{cut}	0	
No. of points on the ρ vs. ϵ_v curve	6	
Volumetric strain values, ϵ_v	0	.0025 .01 .04 .05 .055
Corresponding pressure values, ρ	0	15E7 21.25 E734E7 41.3E7 50E7

The projectile dynamic responses for material models #3 and #5 are shown in Figure 24. The initial impact velocity was 100 m/s. In this case, the projectile penetration was less for material model #5, which was opposite to the outcome for the smaller projectile (Figure 19). Otherwise the responses were similar. Moreover, material model #5 again failed to provide a residual stress field as shown by the absence of stress contours in Figure 25, due again to the target material having pulled away from the projectile.

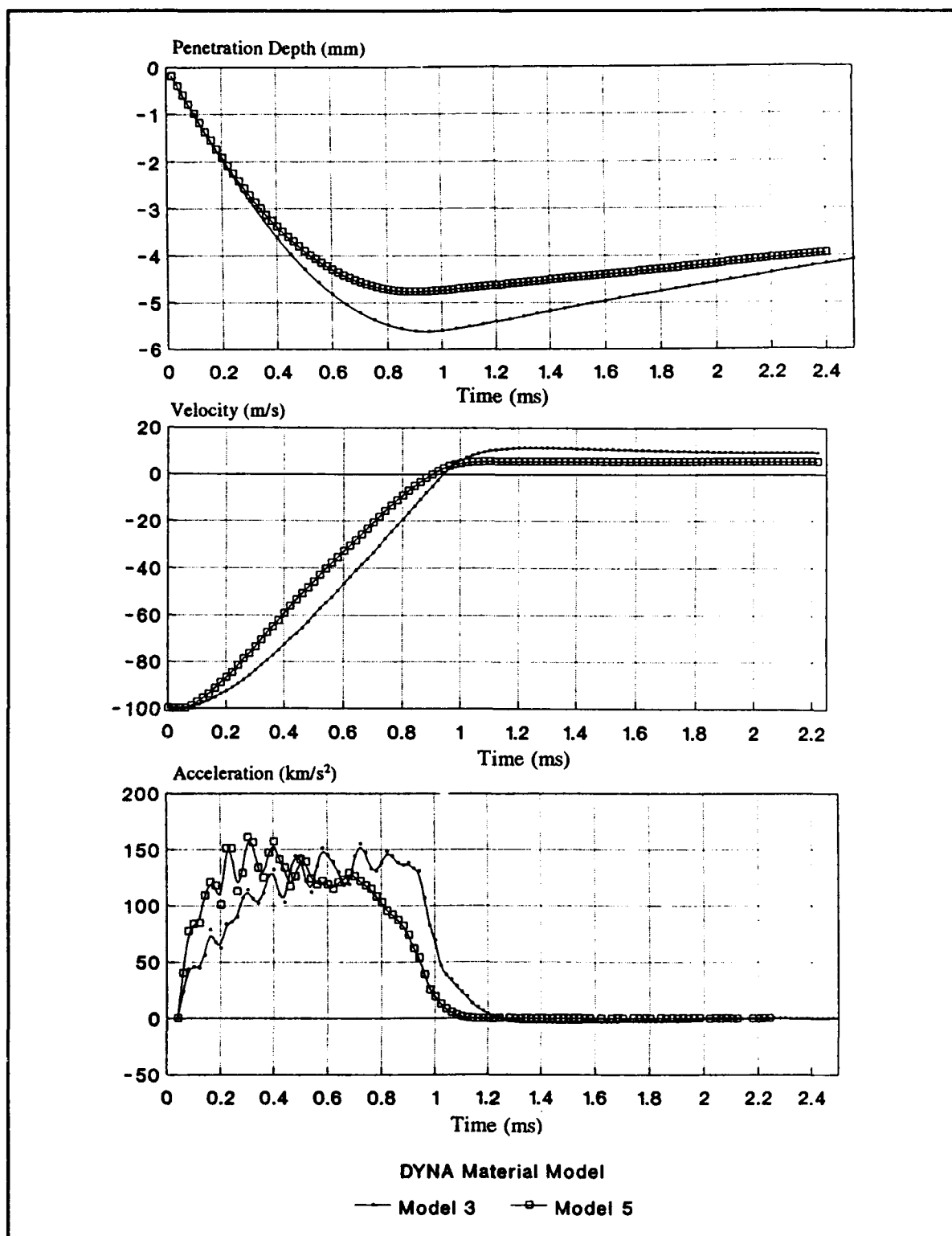
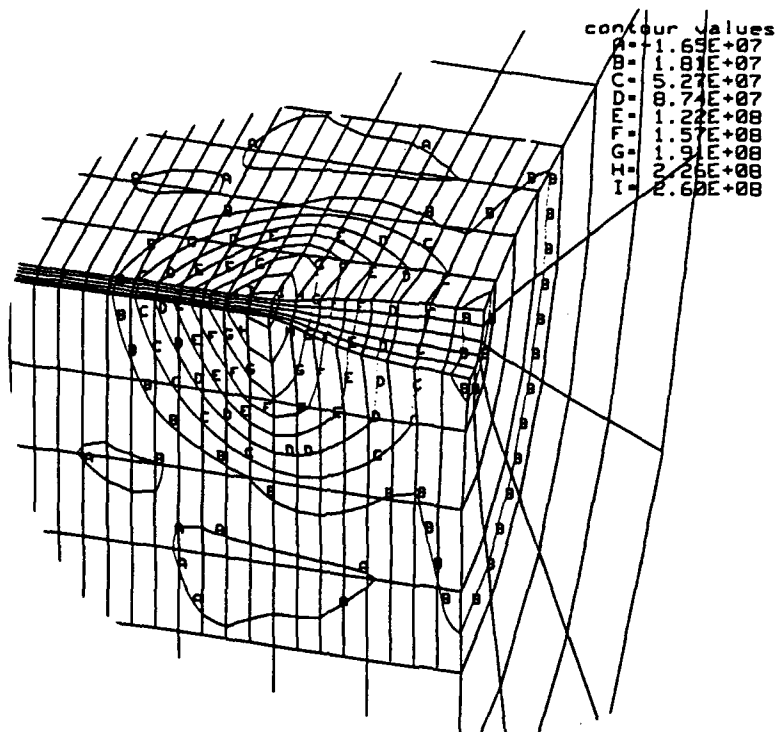
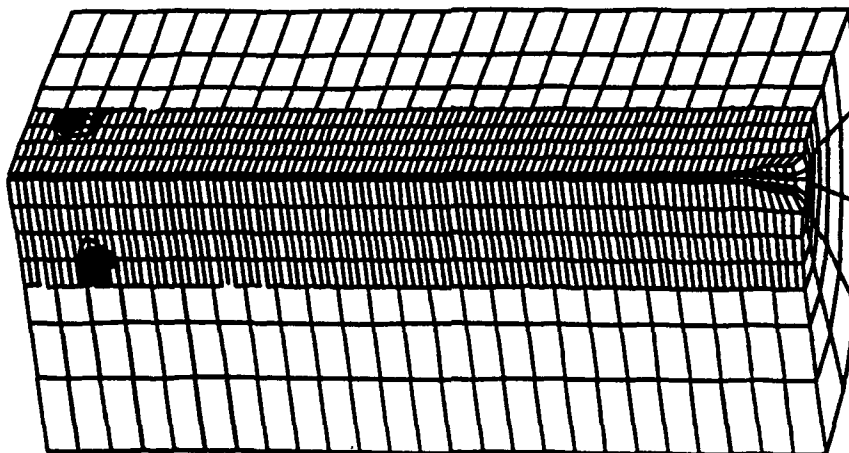


Figure 24
Effect of target material models on larger anchor projectile
penetration depth, velocity, and acceleration.



(a) Material model #3.



(b) Material model #5.

Figure 25
Contours of target pressure for larger anchor projectile.

ANALYSIS OF CONFINEMENT STRESS

The confinement stress field resulting from an embedded anchor projectile is prerequisite information for calculating extraction load-deformation behavior and the holding capacity of the anchor. The purpose of this section is to analyze the computed three-dimensional residual stress field that surrounds an anchor projectile, particularly at the interface where the stresses impinge on the projectile. Confinement stresses are first defined and discussed. Then computed results are discussed which demonstrate how to interpret confinement stress data in the context of anchor extraction studies. The effects of various parameters on confinement stress are also discussed.

Description and Discussion of Residual and Confinement Stress Data

In this section a distinction between residual and confinement stress is made. Residual stress is defined as the stress response computed at the time the anchor projectile has come to rest. Confinement stress is a subset of these data referred to the target elements lining the cavity formed by the impact. Specifically, the direct or normal residual stress component acting on the anchor projectile surface and the shear residual stress component acting on the projectile tangential to this surface are defined as confinement stresses.

In the computation of contact/impact phenomena, more accurate contact stress data can sometimes be obtained from nodal force data which has been converted to contact stress by a tributary element method (Hughes, et al., 1976). Element stresses are averaged quantities at the center of the element and therefore are not strictly associated with the interface surface. However, nodal force data cannot be conveniently post-processed with TAURUS. Thus, only element stress data were considered in this analysis of confinement stress. Further, computed pressure contour data, although easy to interpret and invariant, was avoided in the analysis of confinement stress because pressure is an average of the three normal stress components. The difference in magnitude between confinement stress and pressure can therefore be substantial because of the influence of tensile stress which often occurs in the hoop direction.

The following confinement stress components are of interest and pertain to any arbitrary plane containing the symmetry axis of the penetration model: normal stress (σ_x), shear stress (τ_{zx}), both referred to the positive xz plane, for example, of the target as shown in Figure 26, as well as the maximum and minimum principal stresses (σ_{\min} and σ_{\max}). The vertical normal stress components, σ_z and σ_y , and the maximum shear stress and the intermediate principal stress components are otherwise not required for the present discussion.

The intersection of the vertical xz plane and the cavity is curved in the region of the projectile nose. The residual normal stress (σ_x) and residual shear stress (τ_{zx}) components in this region are not strictly confinement stresses because they are not normal or tangential to the projectile. Local stress component data are actually needed in this region instead of the global stress component data being discussed. Local stress components are currently not conventionally processed by DYNA3D. Therefore, in the region of the projectile nose, the minimum principal stress σ_{\min} (largest compressive stress) data should also be considered in the analysis of confinement stress in the absence of local stress data.

An understanding of cavity expansion theory also helps to interpret numerically computed confinement stress data. From the results of this theory, similarity should be anticipated between the σ_x and σ_{\min} stress components. Cavity expansion theory assumes the strain energy in the target to be distributed exclusively in horizontal planes. In effect, this theory assumes σ_x to be identical to σ_{\min} (in the vertical xz plane). Further, values for these components should tend to

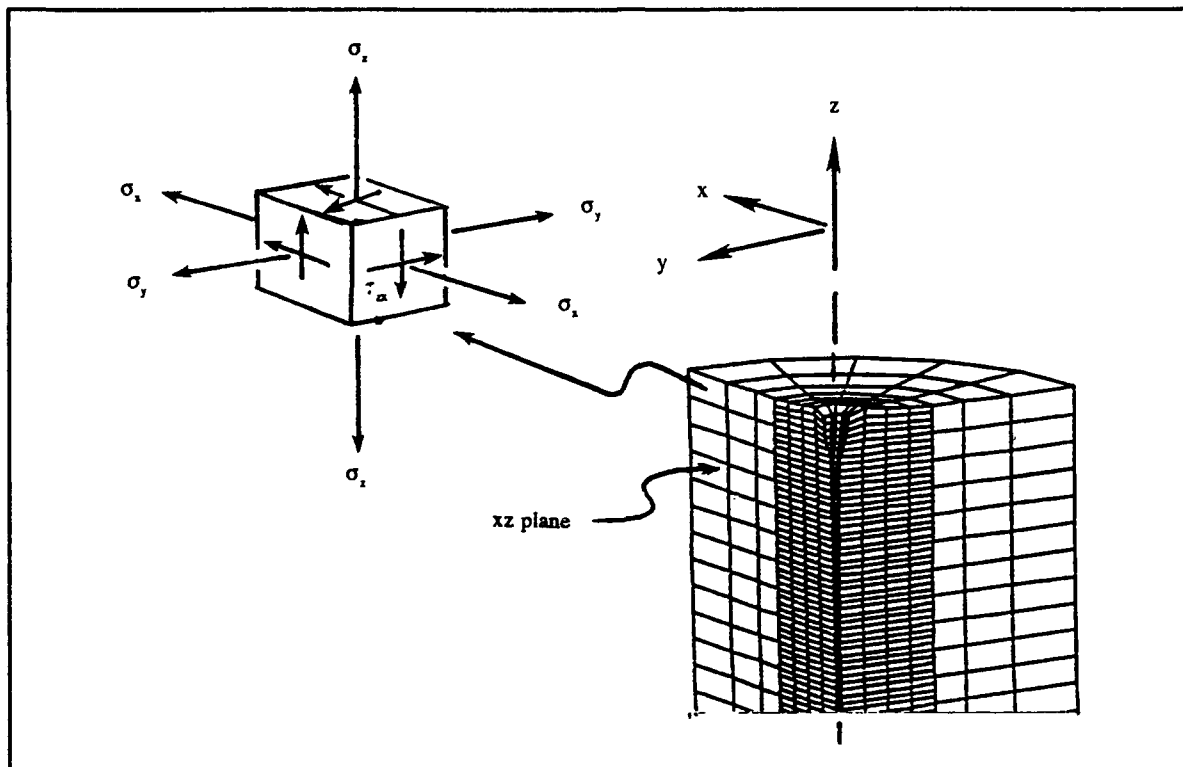


Figure 26
Stress block at center of a typical finite element in target model.

be compressive. The extent to which calculated three-dimensional residual stress data differ from these observations, is the extent to which the essentially one-dimensional character of cavity expansion theory is in error. Conversely, cavity expansion theory suggests that stress components σ_x and σ_{\max} should be dissimilar, and that they should be of opposite sign. This is because the theory effectively assumes that σ_{\max} is identical to the tangential or hoop stress component, which tends to be tensile.

Discussion of Results

Residual stress fields for the four components (σ_x , τ_{zx} , σ_{\max} , σ_{\min}) are presented in contour data form and discussed for two anchor projectile simulations involving sandstone targets: the smaller fastener anchor projectile simulation and the larger anchor projectile simulation. For the respective input data files, see Appendix F, try #7 and run #1. Twenty DYNA3D simulations of penetration models were conducted during the course of this project. These two simulations were considered to be more realistic. Others were aimed at understanding the effects of various simulation parameters as previously described in the parameter study.

Smaller Fastener Anchor Projectile. The residual stress results for the fastener anchor projectile problem are presented in Figure 27. The residual stress contour values are in units of $\text{kg/mm} \cdot \text{s}^2$ (to convert to MPa, multiply the data in Figure 27 by 10^{-3}). Negative values in the figure refer to compressive stress. It is noted that, as required by rotational symmetry, the

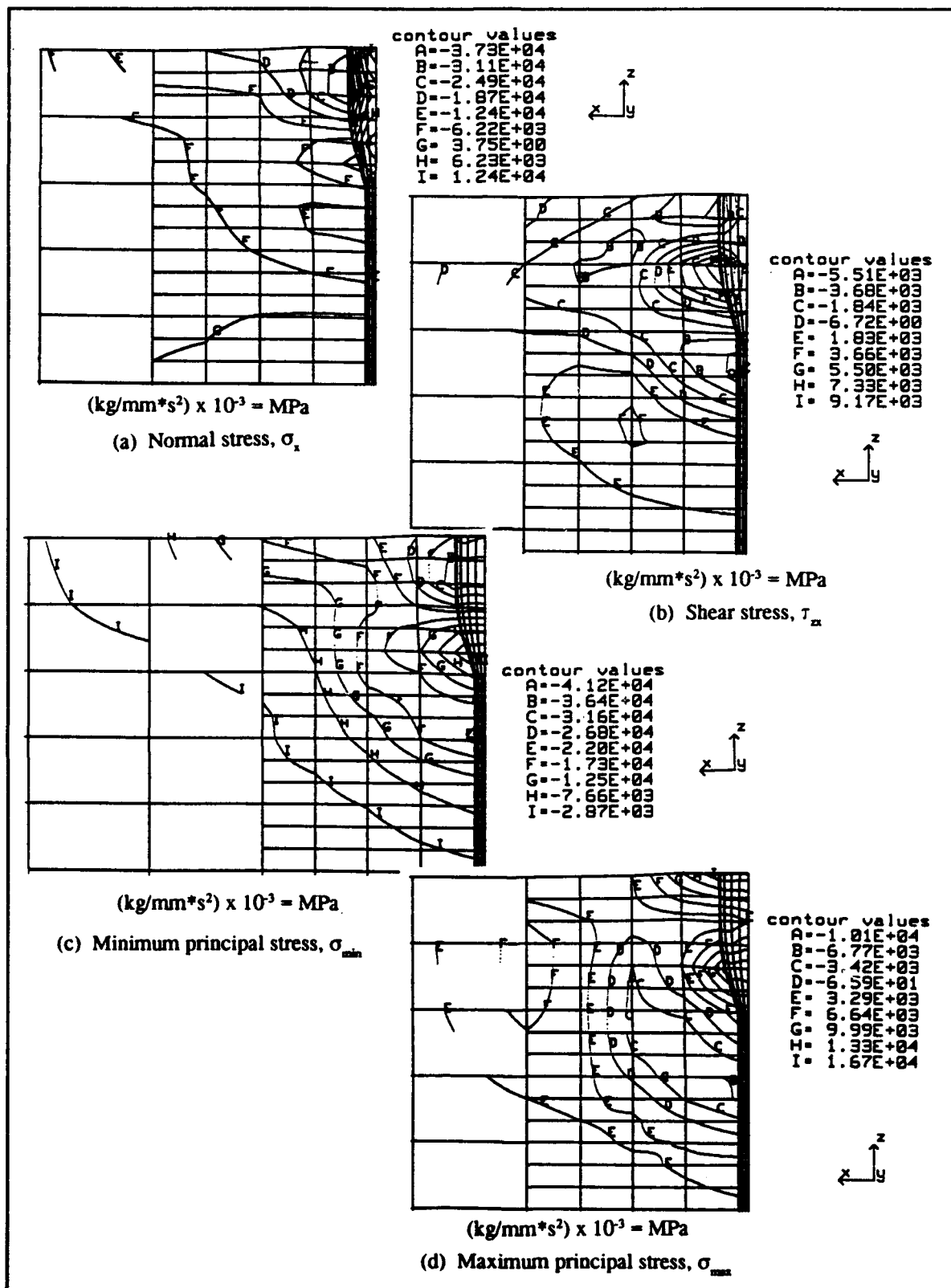


Figure 27
Residual stresses for smaller fastener anchor projectile in sandstone.

computed principal stress data shown are rotationally symmetric, while the normal and shear stress data shown are restricted to the xz plane.

Irrespective of the particular component, the largest residual stresses occur adjacent to the embedded anchor projectile. Thus, confinement stresses are observed to be the largest residual stresses in the surrounding rock medium. Residual stress decays rapidly with distance from the embedded anchor projectile. Beyond two or three projectile diameters, the residual stress in the rock is negligible. This behavior is generally consistent with cavity expansion theory which also predicts the rate of decay of the residual stress. The particular cavity expansion theory presented in Appendix A predicts that residual stress decreases as $1/r^2$ in the cracked region of brittle materials and as $1/r^3$ in the elastic region beyond, where r is radial distance from the symmetry axis (see Figure A-4).

In Figure 27(a), the maximum value for σ_x , the normal component of confinement stress, occurs halfway down the length of the embedded projectile shank (straight part). In Figure 27(b), the maximum value for τ_{zx} , the tangential component of confinement stress, occurs slightly farther up on the embedded projectile shank. The contour pattern for the minimum principal stress component presented in Figure 27(c) is similar to the contour pattern for the normal stress component. The confinement stress diminishes almost an order magnitude from the maximum location, midway along the shank, to the anchor projectile tip.

The maximum principal stress, shown in Figure 27(d), tends to be tensile, and approximates the hoop stress component (the σ_y component which is not shown) in the rock surrounding the projectile. As such, it is not a confinement stress per se, but it is indicative of the cracking potential of the rock surrounding the projectile, which can, in turn, affect confinement stress. The maximum value of this stress component occurs at the surface in the crater uplift area which is shown as a raised surface adjacent to the projectile. It diminishes to a depth midway along the cavity, whereupon it increases again toward the projectile nose. However, since cracking was excluded from these calculations, stress levels above the tensile strength of sandstone (0.1 to 4.5 MPa) are clearly unrealistic.

The contour data presented above were calculated using a tunnel-to-projectile diameter ratio of 0.35. They are between the results for a ratio of 0.25, and the results for a ratio of 0.50 (respectively, tries #9 and #8, Appendix F). The results for these two cases are shown in Figure 28, and were compared with the results in Figure 27(a). The size of the tunnel has little effect on the residual stress response if the ratio is near 0.25, the value arrived at on the basis of target penetration depth in the parameter study.

The coefficient of friction influences the depth of anchor projectile penetration, but varying the coefficient from zero to 0.1 was found to have little influence on confinement stress. The residual stress field resulting from specifying no friction (try #12, Appendix F) is shown in Figure 29. It is very much the same as the residual stress field for a coefficient of friction of 0.1 (Figure 27a). The difference is only in the location of maximum confinement stress which changes to a higher position on the shank of the anchor projectile due to greater depth of penetration. The anchor holding force should correspondingly increase due to greater penetration, but confinement stress (which is basically unit holding force) is basically independent of the coefficient of friction.

In the parameter study, it was found that penetration depth was influenced by the hardening modulus of the rock when modeled with DYNA3D material model #3. In the present case, the hardening modulus was reduced from one percent of Young's modulus to zero. The residual stress results are shown in Figure 30. When these data are compared with those for a hardening value of one percent (Figure 27a), a corresponding decrease in confinement stress of

approximately 25 percent is evident for the case of no hardening. The hardening modulus of rock, therefore, plays a significant role in the magnitude of confinement stress.

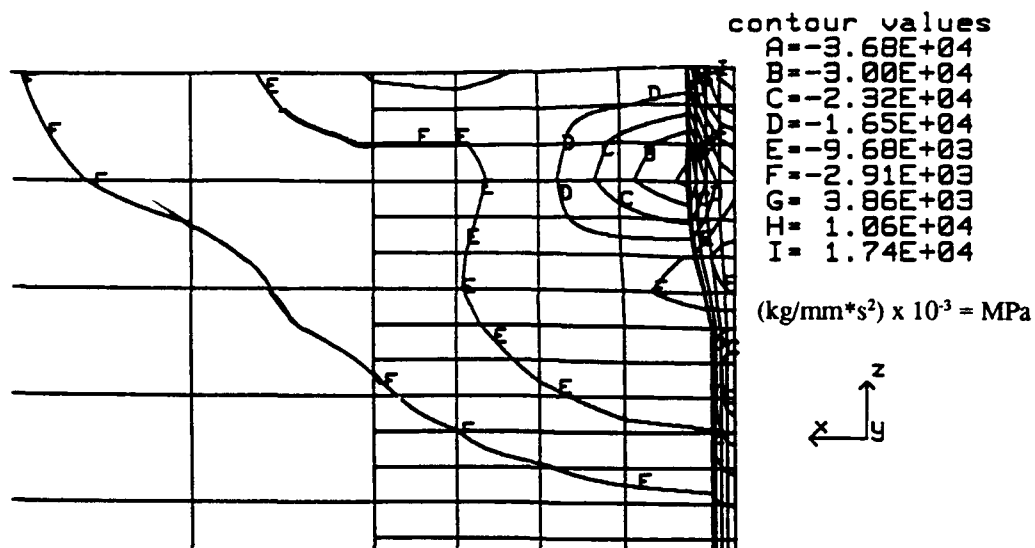
Larger Anchor Projectile. The initial kinetic energy for the large anchor projectile simulation was two times greater than that for the fastener anchor projectile. However, the residual stress field, shown in Figure 31, when converted to a common measure,* was approximately the same as the residual stress field for the fastener problem (Figure 27). The similarity of these results is explained by the specification of the same material model. Both anchor penetration simulations employed the same elastic-plastic material model with the same yield strength and hardening modulus. That the initial kinetic energy of impact and projectile radius differed substantially, made little difference to the residual stress. Thus, residual stress essentially depends on material properties of the rock target. This is also observed in static cavity expansion theory, where the stress necessary to quasi-statically open a cavity of prescribed radius is the primary objective (see Figure A-2 in Appendix A). According to this theory, the stress is independent of dynamics, and primarily dependent on the strength of the target material. Penetration response of the projectile is determined separately by considering an auxiliary dynamic analysis of a penetration model. Thus, the use of appropriate material models for characterizing rock material response in simulation of penetration problems is very important according to the results from both numerical models and analytical models.

The contour patterns for normal stress, σ_x , and minimum principal stress, σ_{\min} , are similar, as shown in Figures 31(a) and 31(c), respectively. This again indicates that the rock strain energy is primarily stratified and nearly contained in horizontal planes, as is assumed in cavity expansion theory. Alternatively, consideration of the vertical stress component, σ_z , may be ignored in favor of σ_x (or σ_y) as has been done in the present analysis of residual and confinement stress. The maximum value of the confinement stress component, σ_x , is located on the projectile nose. Slightly higher stresses occur just beneath the nose. The normal confinement stress component diminishes almost one order of magnitude along the projectile surface from the nose to the surface of the target.

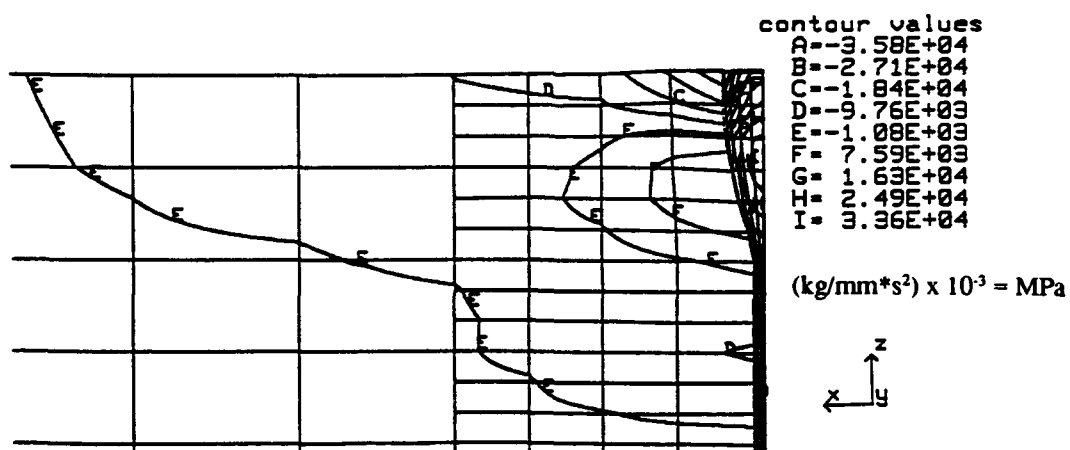
In Figure 31(b), the tangential or shear residual stress component, τ_{zx} , is shown to be less in magnitude than the normal stress component by a factor of about six. The tangential confinement stress varies slowly along the projectile surface from a maximum value at the tip to a minimum value at the surface of the target. The negative contour values of τ_{zx} at the interface indicate that the confinement stress acts upward on the target cavity and downward on the embedded projectile.

Contour data for the maximum principal stress component, σ_{\max} , shown in Figure 30(d) represent primarily a hoop stress component. This stress component is compressive (negative) along the lower half of the embedded projectile and tensile along the upper half. This indicates that radial cracking in the target would be limited to the upper portion of the projectile and certainly to the crater area at the surface.

*To convert the labeled contour values in Figure 31 from $\text{g/cm} \cdot \text{s}^2$ units to MPa units, multiply by 10^{-7} .



(a) Noticeably different σ_x distribution for ratio = 0.50.



(b) Substantially the same σ_x distribution for ratio = 0.25.

Figure 28
The effect of tunnel-to-projectile diameter ratio on residual stress.

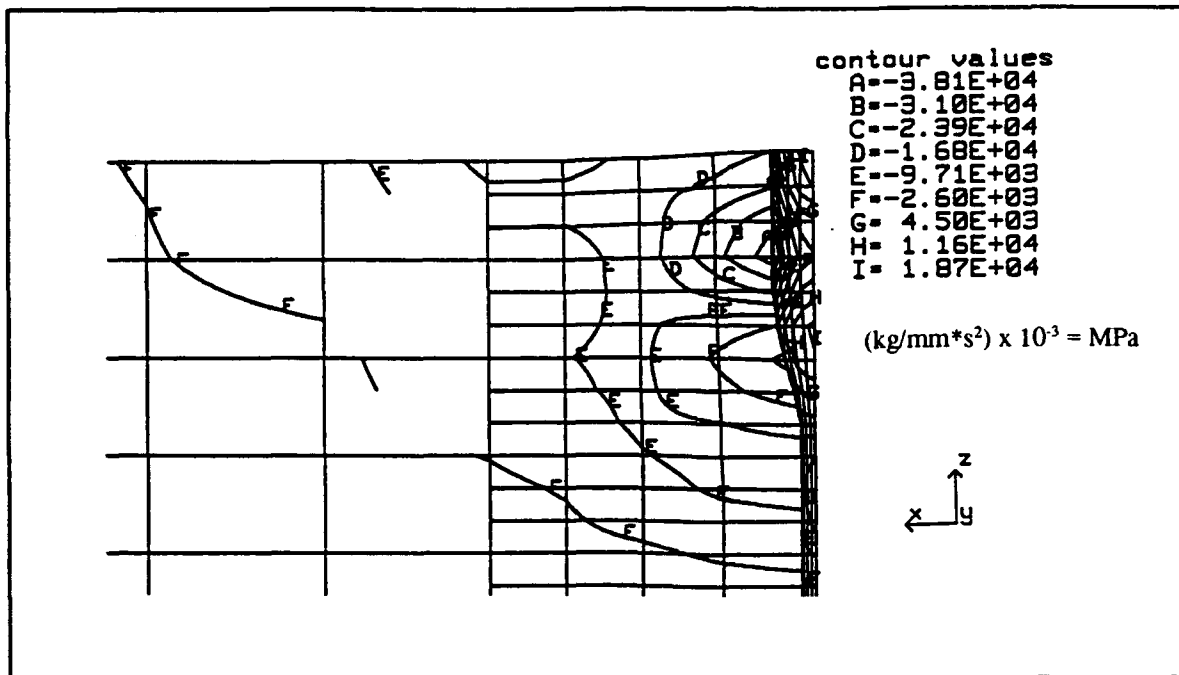


Figure 29
Normal stress, σ_x , for zero coefficient of friction.

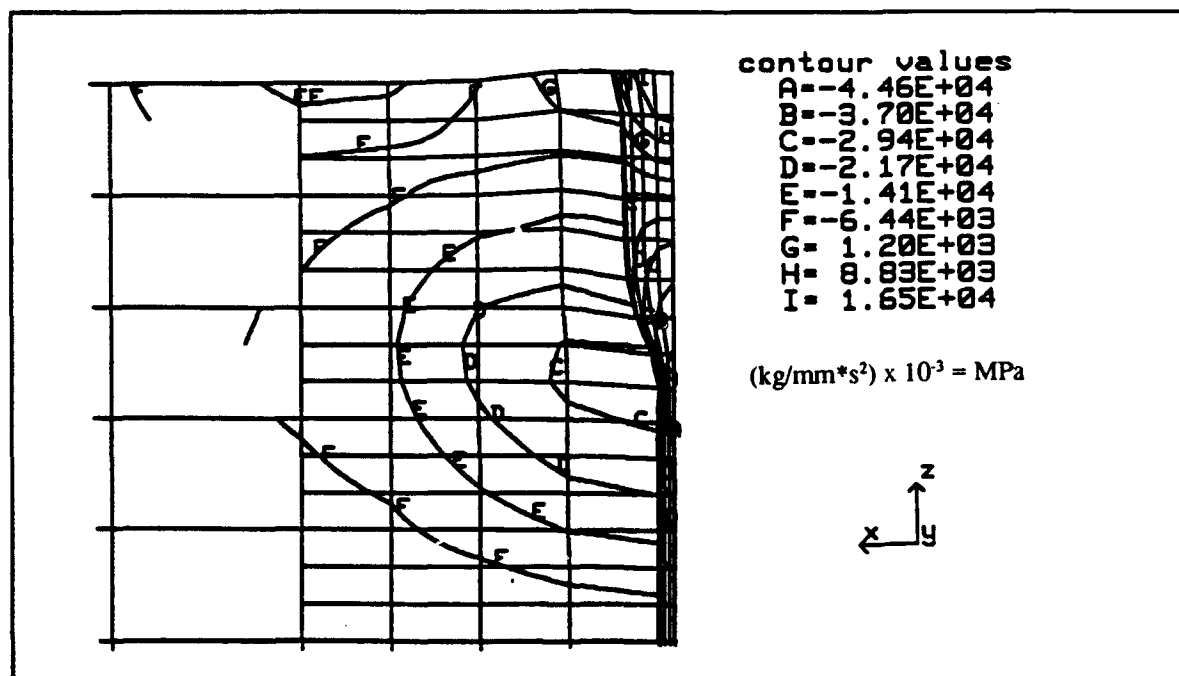


Figure 30
Normal stress, σ_x , for zero hardening modulus.

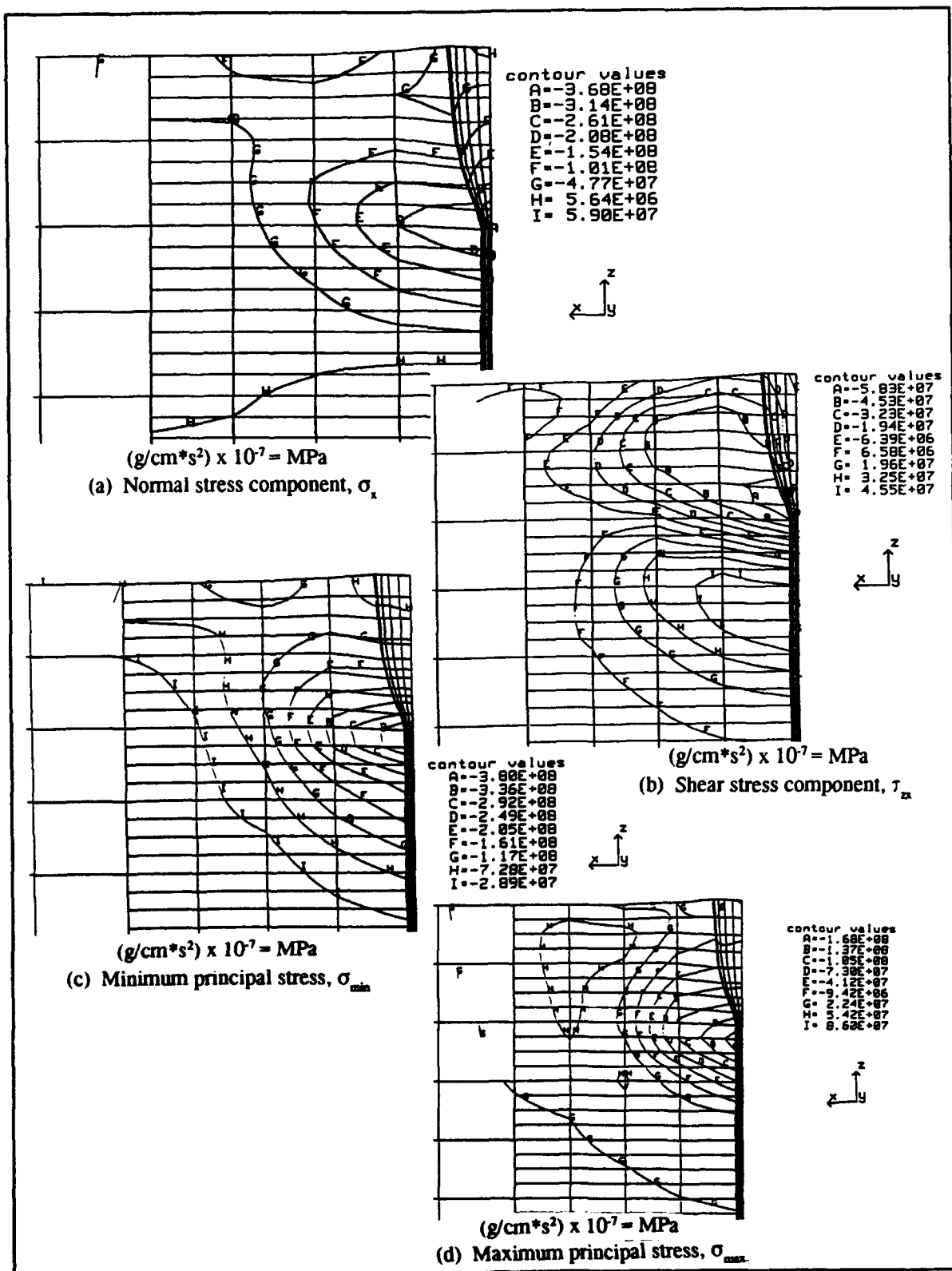


Figure 31
Residual stress for larger anchor projectile in sandstone.

On a typical unit surface area of the projectile, the downward shear confinement stresses, Figure 31(b), are equilibrated by the upward component of normal confinement stress acting on the ogival nose, Figure 31(a). The free body diagram of the projectile, sketched in Figure 32, roughly illustrates the equilibrium of these two components of confinement stress.

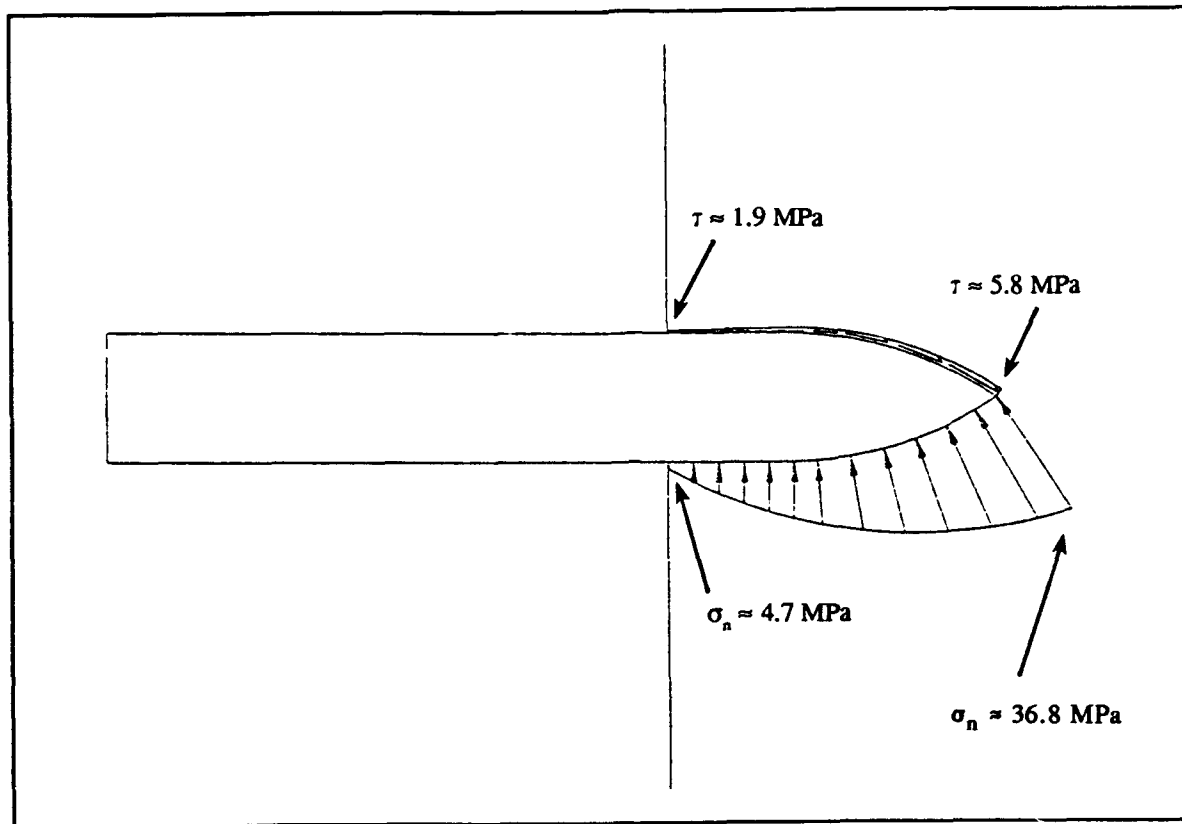


Figure 32
Confinement stress distribution for larger anchor projectile embedded in sandstone.

SUMMARY AND CONCLUSIONS

Three-dimensional finite element modeling of penetration of ballistically embedded projectiles in rock was considered to establish a numerical procedure for investigating the influence of various parameters on the penetration process and on the resulting residual stress fields surrounding the embedded projectile. The explicit finite element program DYNA3D was employed and evaluated for these computations. Insight was also gained from a brief study of cavity expansion theories applied to projectile penetration of rock targets. In this preliminary study, the finite element penetration model was limited to normal projectile impacts and axisymmetric geometry. A deformable projectile model, nonlinear material behavior for the projectile and rock target, and a sliding interface with friction between the projectile and rock target were included in the penetration model.

The following conclusions pertain to construction of a penetration model for determining confinement stress around projectiles embedded in rock targets using DYNA3D.

In general, an artificial tunnel must be included in the finite element model of the rock target to facilitate model construction and to minimize computer run time. The penetration depth, velocity, deceleration, and stress response were not affected by the tunnel if the tunnel-to-projectile diameter ratio was less than 0.25. In a similar manner, a small artificial bore at the center of the finite element model of the projectile may be used to enhance the numerical efficiency of the penetration model.

The target may be divided into two parts to facilitate finite element subdivision. The inner part of the model must be finely subdivided to capture the high deformation gradients that occur near the target/projectile interface. The outer part of the target model may be coarsely subdivided, and its outer diameter may be limited to three to four times the projectile diameter without affecting accuracy, since stress fields decay rapidly with distance from the projectile.

Specification of a sliding surface is essential in modeling the behavior of the projectile/target interface. Further, a tied sliding interface option was convenient for imposing displacement compatibility at the interface between the inner and outer parts of the target model.

Twenty simulations of penetration models were conducted. The models included a smaller anchor projectile, representing a fastener, penetrating a sandstone target, and a larger rock anchor projectile also penetrating a sandstone target. All simulations were limited to normal projectile impacts. They were also limited to three-dimensional quarter models of axisymmetric penetration configurations to minimize simulation turnaround time using a Sun 4/260 workstation. Simulation times were found to easily allow for overnight turnaround time, and improved performance may be anticipated with newer workstation hardware.

In summary the DYNA3D system proved remarkably facile in simulating complex penetration problems and calculating the structural dynamics of normally impacting, ballistically embedded projectiles and the associated confinement stress fields surrounding the embedded projectile.

Direct attempts to validate the numerical penetration model using existing analytical solutions for penetration problems based on cavity expansion theory were not successful. The analytical solutions are generally too limited to serve as a benchmark. They cannot provide stress data results with sufficient detail commensurate with the detail in residual stress gradients surrounding the body of embedded projectiles. However, the results from a particular spherical cavity expansion theory were useful as a guide to interpretation of numerical results, and substantial qualitative agreement was found between numerical and analytical solutions for residual stresses surrounding embedded projectiles.

In a further attempt at validation, an existing DYNA2D numerical solution of an axisymmetric penetration problem was replicated using the DYNA3D penetration model developed in this study. The DYNA3D prediction of penetration depth did approach the DYNA2D solution from below, as expected from the mathematical theory of the displacement-based finite element method.

Parameter studies of the penetration models were conducted to assess the effects of alternative DYNA3D material models for rock targets including various target strengths, and to assess the effects of alternative coefficients of friction for a Coulomb model of the sliding interface between the projectile and rock medium.

Of four DYNA3D material models identified as potentially suitable for modeling rock targets, two were investigated in this study. The more successful model was an elastic-plastic strain hardening model. This model, however, does not allow for modeling the brittle behavior

of rock in tension. A second model, the soil and crushable foam model, does allow for a tension cutoff and brittle material modeling. However, this model failed to work when the tension cutoff value specified was other than zero. When it did work, a null solution was obtained for the residual stress state in the target material because the target cavity produced by the impact separated from the embedded projectile.

The strain hardening modulus for the elastic-plastic material model for rock targets had the most influence on computed residual stress states. A value equal to 1 percent of Young's modulus for the rock material, resulted in a 25 percent increase in confinement stress acting on the embedded projectile, and a similar decrease in penetration depth, when compared to the results assuming no strain hardening in an elastic-perfectly plastic material model characterization of the rock target.

In contrast with the strength of the rock target material, the coefficient of friction at the projectile/target interface had only a minor affect on confinement stress. However, an increase in projectile deceleration and a decrease in penetration depth with increasing coefficient of friction did occur as expected.

RECOMMENDATIONS

Further studies to evaluate DYNA3D material models for rock targets are required. Material models must eventually account for cracking in rock media. Recently published DYNA3D documentation (Whirley and Hallquist, 1991) includes much improved definitions of material models and input parameters that will facilitate additional study of material models for rock. Material models accounting for more realistic behavior including anisotropic in-situ fracture conditions which could greatly influence the penetration process may yet have to be developed. The experience of the present study is that rock target material modeling remains the most important issue in successful numerical simulation of rock anchor penetration.

Further attempts at validating the numerical penetration model should be pursued and should incorporate the experimental data compiled by Goldsmith and colleagues under NCEL sponsorship, Brunette and Goldsmith (1990), Goldsmith and Zhou (1989), and Zhou and Goldsmith (1990).

Additional studies are needed with larger three-dimensional models that do not exploit two planes of symmetry for convenience. Supercomputers should be used. DYNA3D exists on many of these platforms, and penetration models developed initially on workstations can be easily moved to supercomputing environments where performance increases of two orders of magnitude may be anticipated.

Parameter studies are needed to evaluate the effect of finer mesh subdivisions on the dynamic response of projectiles and on confinement stress. Finer model subdivisions nearer the projectile would improve the definition and accuracy of confinement stress predictions.

There are some post-processing limitations with TAURUS. Local stresses as well as nodal point force data should be made available for assessing confinement stresses more accurately.

Upon refinement of the finite element penetration model as suggested in the aforementioned recommendations, further parameter studies should be resumed to investigate the relationship between residual stress fields and the properties of seafloor rock and PEA projectiles.

REFERENCES

- Beard, R.M. (1984). Memorandum to files on the "Testing of a conical rock fluke for the 20K propellant embedded anchor; status report," Naval Civil Engineering Laboratory, Port Hueneme, CA, Jan 1984.
- Bernard, R.S., and D.C. Creighton (1976). "Projectile penetration in earth material, theory and computer analysis," Defense Nuclear Agency, Washington, DC, Nov 1976.
- Brunette, H., and W. Goldsmith (1990). "Propellant-driven anchoring in rock: Results from initial scaling tests," *Int. J. Impact Engineering*, vol 9, no. 1, 1990, pp 51-69.
- Creighton, D.C. (1982). "Non-normal projectile penetration in soil and rock: User's guide for computer code PENCO2D," TR SL-82-7, U.S. Army Engineering Waterways Experiment Station, Vicksburg, MS, Sep 1982.
- Forrestal, M.J., and D.B. Longcope (1990). "Target strength of ceramic materials for high-velocity penetration," *J. Appl. Phys.*, vol 67, no. 8, 15 Apr 1990, pp 3669-3672.
- Goldsmith, W., and G. Zhou (1989). "Model investigation of seafloor fluke embedment," final report on Contract NCEL-N47408-89-C-1055 for period 4/1989 to 9/1989, Department of Mechanical Engineering, University of California, Berkeley, CA, Sep 1989.
- Hallquist, J.O. (1976). "A procedure for the solution of finite-deformation contact-impact problems by the finite element method," UCRL-52066, Lawrence Livermore National Laboratory, University of California, Livermore, CA, Apr 1976.
- _____ (1977). "A numerical procedure for three-dimensional impact problems," Preprint UCRL-78765, Lawrence Livermore National Laboratory, University of California, Livermore, CA, Aug 1977.
- _____ (1978). "A numerical treatment of sliding interfaces and impact. Computational techniques for interface problems," *ASME, AMD*, vol 30, Dec 10-15 1978, pp 117-133.
- Heuzé, F.E. (1989). "An overview of projectile penetration into geological materials, with emphasis on rocks." *Computational techniques for contact, impact, penetration and perforation of solids*, *ASME, AMD*, vol 103, Dec 1989, pp 275-308.
- Hill, R. (1950). "The mathematical theory of plasticity," Oxford University, Oxford.
- Hughes, T.J.R., R.L. Taylor, J.L. Sackman, A. Currier, and W. Kanoknukulchai (1976). "A finite element method for a class of contact-impact problems," *Computational Methods in Applied Mechanics and Engineering*, vol 8, 1976, pp 249-276.
- Rainsberger, R. (1988). "INGRID by example. A pictorial tutorial, UCID-2156, Lawrence Livermore National Laboratory, University of California, Livermore, CA, Nov 1988.

Schulz, J.C. (1978). "Finite element structural analysis of a kinetic energy warhead penetrating concrete," Naval Weapons Center, NWC Technical Memorandum 3621, China Lake, CA, Sep 1978.

Schwer, L.E., R. Rosinsky, and J. Day (1988). "An axisymmetric Lagrangian technique for predicting earth penetration including penetrator response," *Int. J. Num. Anal. Meth. Geom.*, vol 12, Nov 1988, pp 235-262.

Schwer, L.E., and J. Day (1991). "Computational Techniques for Penetrations of Concrete and Steel Targets by Oblique Impact of Deformable Projectiles," *Nuclear Engineering and Design* 125 (1991), pp 215-238.

Shugar, T.A., and P.C. Wager (1982). "Structural analysis of propellant-embedded anchor systems," *Ocean Structural Dynamics Symposium '82 Proceedings*, Sep 8-10 1982, Oregon State University, Corvallis, OR.

Stowe, R.L. (1984). Naval sea anchor project, Structures Laboratory, U.S. Army Corps of Engineers Waterways Experiment Station, Vicksburg, MS, Oct 1984.

Wadsworth, J.F., and R.M. Beard (1980). "Propellant-embedded anchors: Prediction of holding capacity in coral and rock seafloors," Naval Civil Engineering Laboratory, Technical Note N-1595 (DTIC ADA103105), Port Hueneme, CA, Nov 1980.

Whirley, R.G., and J.O. Hallquist (1991). "DYNA3D: A nonlinear, explicit, three-dimensional finite element code for solid and structural mechanics - User manual," UCRL-MA-107254, Lawrence Livermore National Laboratory, University of California, Livermore, CA, May 1991.

Wilson, J.M., P.B. Attewell, D.R. Williams, D.B. Williams, and G. Zhou (1990). "Penetration and pullout strength of fasteners fired into rocks," *Proceedings of the ISRM International Symposium on Static and Dynamic Considerations in Rock Engineering*, Swaziland, Africa, Sep 1990.

Zhou, G. (1988). Penetration of fastener projectiles into construction materials, PhD thesis, School of Engineering and Applied Science, University of Durham, UK, Sep 1988, 237 pp.

Zhou, G., and Goldsmith, W. (1990). Factors related to propellant-driven anchoring in rock, Final report to NCEL on contract NCEL-N47408-89-C-1055, Department of Mechanical Engineering, University of California, Berkeley, CA, Dec 1990.

Appendix A

A SPHERICAL CAVITY EXPANSION THEORY

An overview of a spherical cavity expansion theory applied to projectile penetration is presented. The theory facilitates understanding of fundamental behavior in rock anchor projectile problems, and is used in the present project as a guide to interpreting results from the numerical models.

Introduction

The basic idea is to analyze the penetration of an object in a semi-infinite medium by simulating it as a cavity expanding in an infinite medium.

As an example, consider that the medium is elastic-perfectly plastic, incompressible, and obeys the von-Mises yield condition, and that quasi-static expansion of a cavity from radius $r = 0$ to $r = a$ is to take place under the action of an unknown stress σ_s as shown in Figure A-1. The stress is to be determined by cavity expansion theory.

In this case, cavity expansion theory yields the following radial stress at the cavity radius, $r = a$ (see Schulz, 1978, or Bernard and Creighton, 1976),

$$\sigma_s = \frac{2}{3} \sigma_y \left[1 + \ln \left(\frac{2}{3} \epsilon_y \right) \right] \quad (\text{A-1a})$$

where σ_y and ϵ_y are the unaxial stress and strain, respectively, at the yield point. The maximum shear stress in this material is assumed to be

$$\tau_s = \frac{1}{2} \sigma_y \quad (\text{A-1b})$$

An auxiliary analysis of a simple penetration model is developed next. Assume during penetration that the stresses in Equation A-1 act over the hemispherical tip of a rigid spherical-nosed projectile. The total drag force, F_s , acting on the projectile can then be obtained by integration over the hemisphere, as follows.

$$F_s = \pi a^2 \left(\sigma_s + \frac{\pi}{2} \tau_s \right) \quad (\text{A-2})$$

Conservation of momentum for the projectile requires that

$$F_s = m \dot{v} \quad (\text{A-3})$$

where m is the projectile mass and v is the projectile velocity, and a superscript dot indicates differentiation with respect to time.

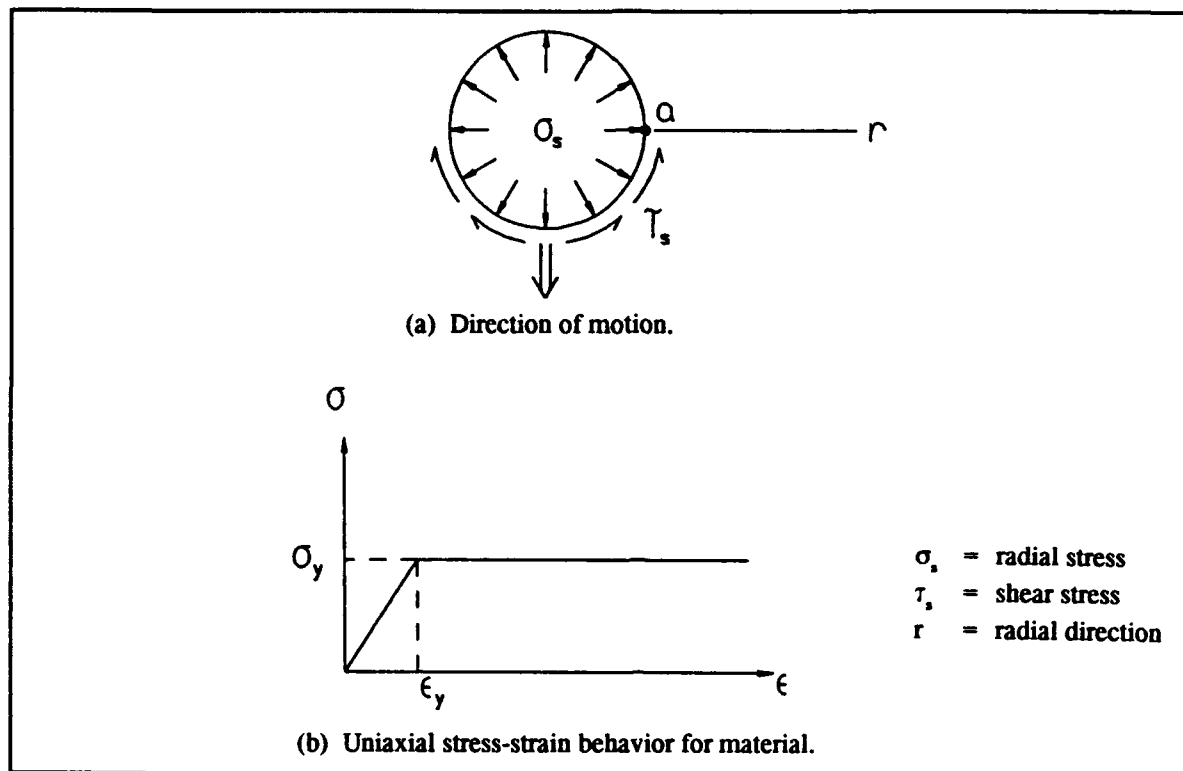


Figure A-1
One-dimensional coordinate system, stress and material behavior.

Equations A-1, A-2, and A-3 can be combined to yield a first order differential equation for the velocity as a function of time, which can easily be integrated. A second integration will yield the penetration depth, z , of the projectile as a function of time. The results are:

$$v(t) = \left[\frac{\pi a^2}{m} \left(\sigma_s + \frac{\pi}{2} \tau_s \right) - g \right] t - v_0 \quad (A-4)$$

$$z(t) = \left[\frac{\pi a^2}{m} \left(\sigma_s + \frac{\pi}{2} \tau_s \right) - g \right] \frac{t^2}{2} - v_0 t \quad (A-5)$$

where v_0 is the initial impact velocity at $t = 0$.

The crucial part of the penetration model analysis is knowing the radial stress on the cavity surface. Once known, the depth of penetration can then be determined similarly as shown by the above simple penetration model example.

Spherical Cavity Expansion Theory for Infinite Brittle Medium

A spherical cavity theory is presented for determining the radial stress at the cavity radius for brittle materials such as concrete and rock. The presentation is based on a re-derivation of the equations published by Forrestal and Longcope (1990) with extension of the results to plain

concrete. The equations presented in this brief publication were confirmed, and their re-derivation in this study served to further explicate the theory.

Referring to Figure A-2, the problem addressed is to find an analytical expression for the radial stress $\sigma_r(a)$. The following primary assumptions are made:

- Spherical symmetry ($\sigma_\phi = \sigma_\theta$)
- Homogeneous and isotropic material
- Quasi-static cavity expansion

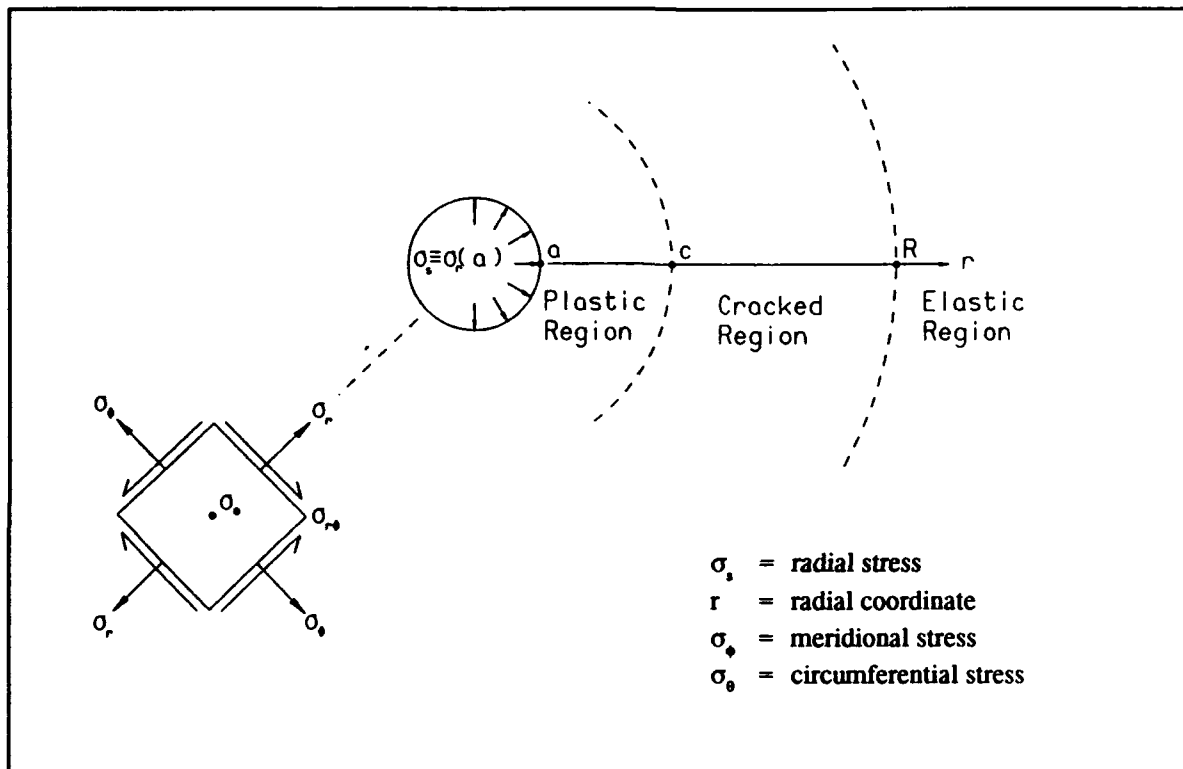


Figure A-2
Coordinate system, stress definitions, and material behavior region.

Material descriptions for the three regions indicated are required. The elastic region is characterized by the following constants:

- K = bulk modulus
 E = Young's modulus
 ν = Poisson's ratio
 T = tensile strength

The cracked region is characterized as follows. Radial cracks are assumed to exist and, therefore, $\sigma_\phi = \sigma_\theta = 0$. Otherwise, the region is elastic with the same parameters as the elastic region. It is this region that specializes the theory for brittle media.

The plastic region is characterized by the following constants.

Y = compressive strength

λ = pressure-dependent constant for shear strength ($0 \leq \lambda \leq 1$)

τ = shear strength which depends on confinement or mean stress, and is calculated by

$$\tau = (3 - \lambda) Y/3 \quad (\text{A-6})$$

Elastic Region, $r \geq R$. The boundary value problem describing the elastic region is:

$$\text{Governing equation of equilibrium:} \quad \frac{d\sigma_r}{dr} + \frac{2}{r} (\sigma_r - \sigma_\theta) = 0 \quad (\text{A-7a})$$

$$\text{Boundary condition:} \quad \sigma_r(R) \equiv P \quad (\text{A-7b})$$

where the radial stress P will be related to the tensile strength of the elastic material on the verge of cracking.

The solution of the boundary value problem, which is given by Hill (1950), is:

$$\text{Radial stress:} \quad \sigma_r = \frac{PR^3}{r^3} \quad (\text{A-8a})$$

$$\text{Circumferential (tension) stress:} \quad \sigma_\theta = -\frac{PR^3}{2r^3} \quad (\text{A-8b})$$

$$\text{Meridional stress:} \quad \sigma_\phi = \sigma_\theta \quad (\text{A-8c})$$

$$\text{Radial displacement:} \quad u = \frac{1+\nu}{2E} \frac{PR^3}{r^2} \quad (\text{A-8d})$$

At the boundary $r = R$, the stresses are evaluated as

$$\sigma_r = P \quad (\text{A-9a})$$

and

$$\sigma_\theta = \sigma_\phi = -\frac{P}{2} \quad (\text{A-9b})$$

Further, due to cracking of the elastic material at the boundary,

$$\sigma_{\theta} = -T \quad (A-10)$$

Therefore, the radial stress P at the boundary can be determined.

$$P = 2T \quad (A-11)$$

In summary, for the elastic region, the radial stress at $r = R$ is twice the tensile strength, T , and diminishes as $1/r^3$ as shown in Figure A-3.

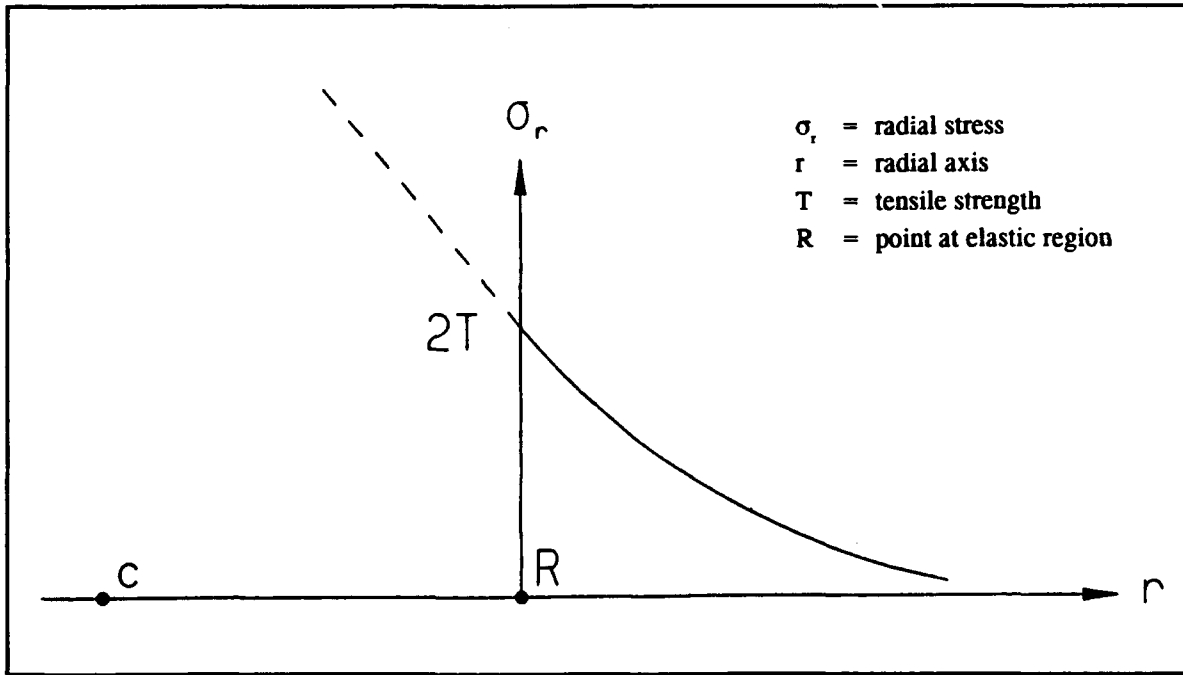


Figure A-3
Radial stress in elastic region.

Cracked Region, $c \leq r \leq R$. The boundary value problem describing the cracked region is:

Governing equation of equilibrium:
$$\frac{d\sigma_r}{dr} + \frac{2}{r} \sigma_r = 0 \quad (A-12a)$$

Boundary condition:
$$\sigma_r(R) = 2T \quad (A-12b)$$

The solution to the boundary value problem, by the method of separation of variables, is:

$$\sigma_r = \frac{2 T R^2}{r^2} \quad (A-13)$$

Apply the boundary condition at $r = c$, that the radial stress equals the compressive strength, Y .

$$\sigma_r(c) = Y \quad (A-14)$$

By eliminating T in terms of Y in Equation A-13, an alternative expression for radial stress is found.

$$\sigma_r = \frac{Y c^2}{r^2} \quad (A-15)$$

Equating the two expressions in Equations A-13 and A-15 for radial stress, the following relationship is obtained.

$$\left(\frac{c}{R}\right)^2 = \frac{2 T}{Y} \quad (A-16)$$

The following remarks stem from Equation A-16.

- The ratio of radii defining the limits of the cracked region is fixed by the tensile and compressive strengths of rock.
- It may be supposed that the definition of a brittle material becomes one in which the compressive strength is more than twice the tensile strength so that the radii ratio does not exceed one.
- The values of c and R are obtained after consideration of the plastic region and completing the solution of the problem.

To obtain the radial displacement for the cracked region, the pressure-volume relation is applied

$$p = K \epsilon \quad (A-17)$$

Here, p is the mean stress which, for the cracked region, is,

$$p = \frac{1}{3} \sigma_r \quad (A-18)$$

and ϵ is the percent volume change which, for the cracked region, is,

$$\epsilon = \epsilon_r + 2 \epsilon_\theta \quad (\text{A-19})$$

The strain-displacement relations are,

$$\epsilon_r = -\frac{du}{dr} \quad (\text{A-20a})$$

and,

$$\epsilon_\theta = -\frac{u}{r} \quad (\text{A-20b})$$

Therefore, using Equations A-17 through A-20, the following relation is obtained:

$$\frac{\sigma_r}{3} = -K \left(\frac{du}{dr} + \frac{2u}{r} \right) \quad (\text{A-21})$$

When Equations A-15 and A-21 are combined, the following equation governing the radial displacement is obtained:

$$\text{Pressure-volume relation in terms of } u: \quad \frac{du}{dr} + \frac{2u}{r} = -\frac{Y c^2}{3 K r^2} \quad (\text{A-22a})$$

$$\text{Boundary condition from elastic region:} \quad u(R) = \left(\frac{1+\nu}{2E} \right) P R \quad (\text{A-22b})$$

The solution of this boundary value problem, by the method of integrating factors, is:

$$u = \left[\frac{(1+\nu) T R^2}{E} + \frac{Y c^2}{3 K} \right] \frac{R}{r^2} - \frac{Y c^2}{3 K} \frac{1}{r} \quad (c \leq r \leq R) \quad (\text{A-23})$$

This completes the analysis of the cracked region. The stress distribution for the cracked and elastic regions is shown in Figure A-4. In the cracked region, the radial stress varies as $1/r^2$, compared to $1/r^3$ for the elastic region. This shows that the presence of radial cracks impedes the decay of radial stress with distance from the source in an elastic medium.

Plastic Region, $a \leq r \leq c$. The governing equation of equilibrium for the plastic region is

$$\frac{d\sigma_r}{dr} + \frac{2(\sigma_r - \sigma_\theta)}{r} = 0 \quad (\text{A-24})$$

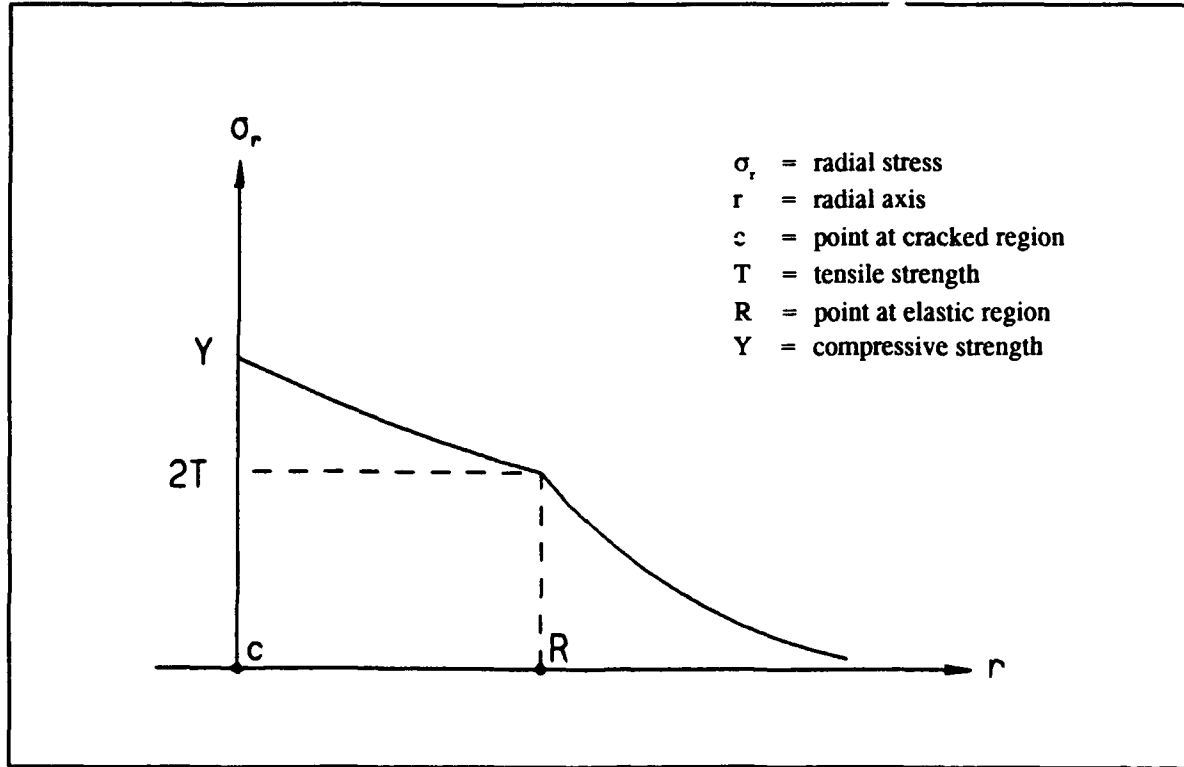


Figure A-4
Radial stress in cracked and elastic regions.

The material is in a state of plastic deformation. Accordingly, stresses must obey the pressure-dependent failure surface relation shown in Figure A-5. This yield surface is described by

$$(\sigma_r - \sigma_\theta) = \lambda p + \tau \quad (\text{A-25a})$$

where

$$p = \frac{1}{3} (\sigma_r + 2 \sigma_\theta) \quad (\text{A-25b})$$

Eliminating σ_θ in terms of σ_r , the governing equilibrium equation becomes,

$$\frac{d\sigma_r}{dr} + \frac{2}{r} \left[\lambda \left(\frac{3\sigma_r - 2\tau}{3 + 2\lambda} \right) + \tau \right] = 0 \quad (\text{A-26})$$

To simplify the algebra, a new constant α is defined,

$$\alpha = \frac{6}{3 + 2\lambda}$$

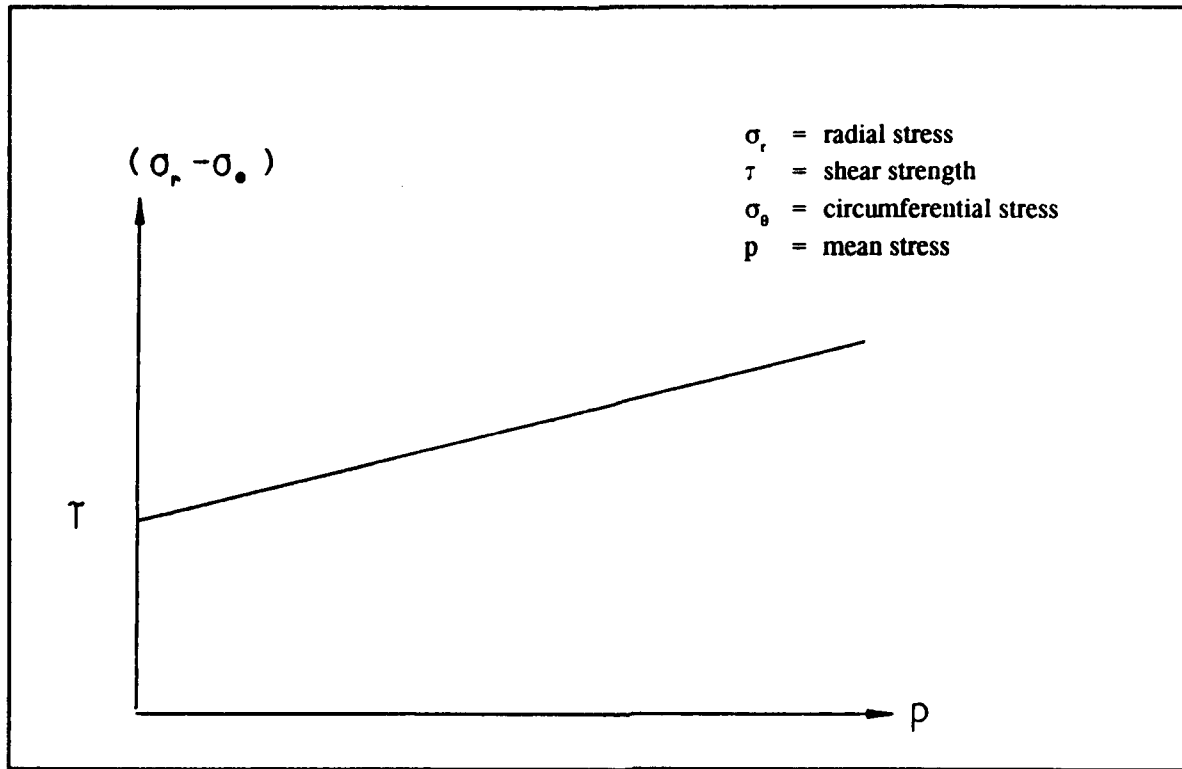


Figure A-5
Constants model for pressure-dependent shear strength.

Thus, the boundary value problem for the plastic region is:

Governing equation of equilibrium:
$$\frac{d\sigma_r}{dr} + \frac{\alpha \lambda}{r} \sigma_r = -\frac{\alpha \tau}{r} \quad (\text{A-27a})$$

Boundary condition:
$$\sigma_r(c) = Y \quad (\text{A-27b})$$

The solution of the boundary value problem, by the method of integrating factors, is:

$$\sigma_r = \frac{Y}{\lambda} \left[\frac{2}{\alpha} \left(\frac{c}{r} \right)^{\alpha \lambda} - \left(\frac{3 - \lambda}{3} \right) \right] \quad (\text{A-28})$$

This expression for radial stress in the plastic region when evaluated at $r = a$ gives the required solution:

$$\sigma_s \equiv \sigma_r(a) \quad (\text{A-29})$$

However, the ratio c/a remains unknown. The required solution for the ratio c/a is outlined in the following steps:

- (1) Invoke the mass conservation equation in Eulerian coordinates and the displacement boundary condition at $r = c$ from the cracked region.

$$\text{Mass conservation: } \frac{d}{dr}[(r - u)^3] = \frac{3 \rho r^2}{\rho_0} \quad (\text{A-30a})$$

$$\text{Boundary condition: } u(c) = \frac{(1 + \nu)TR^3}{Ec^2} + \frac{Y}{3K}(R - c) \quad (\text{A-30b})$$

- (2) Approximate the mass density ratio for small volume changes as follows, and express ϵ in terms of the radial stress,

$$\frac{\rho}{\rho_0} = \frac{1}{1 - \epsilon} \approx 1 + \epsilon = 1 + \frac{Y}{K} \left[\frac{1}{\lambda} \left(\frac{c}{r} \right)^{\alpha \lambda} - \frac{3 - \lambda}{3 \lambda} \right] \quad (\text{A-31})$$

- (3) Substitute Equation A-31 into Equation A-30a and integrate both sides from a to c :

$$[c - u(c)]^3 \approx (c^3 - a^3) \left[1 - \left(\frac{3 - \lambda}{3 \lambda} \right) \frac{Y}{K} \right] + \frac{3Y}{\lambda K(3 - \lambda \alpha)} \left[c^3 - a^3 \left(\frac{c}{a} \right)^{\alpha \lambda} \right] \quad (\text{A-32})$$

- (4) Expand the left-hand side of Equation A-32, neglecting second and higher order terms,

$$[c - u(c)]^3 \approx c^3 - 3c^2[u(c)] \quad (\text{A-33})$$

- (5) The resulting expressions for the required ratio, after some algebra, are,

$$\text{First order solution: } \left(\frac{a}{c} \right)^3 \equiv \beta = \frac{9}{2} (1 - \nu) \left(\frac{Y}{2T} \right)^{1/2} \frac{Y}{E} \quad (\text{A-34a})$$

$$\text{Second order solution: } \left(\frac{a}{c} \right)^3 = \beta + \frac{\beta(1 - 2\nu)Y}{\lambda E} \left[(3 - \lambda) - (3 + 2\lambda) \left(\frac{1}{\beta} \right)^{\alpha \lambda / 3} \right] \quad (\text{A-34b})$$

In these expressions, T is the tensile strength, E is Young's modulus, and ν is Poisson's ratio. This completes the solution of the plastic region and the spherical cavity problem.

Summary. The pressure necessary to open a spherical cavity from zero initial radius to radius $r = a$ is,

$$\sigma_s \equiv \sigma_r(a) = \frac{Y}{\lambda} \left[\frac{2}{\alpha} \left(\frac{c}{a} \right)^{\alpha \lambda} - \left(\frac{3 - \lambda}{3} \right) \right] \quad (\text{A-35})$$

where $\frac{c}{a} = \left(\frac{1}{\beta}\right)^{1/3}$ = the first order solution

Y = the uniaxial compressive strength

λ = the pressure dependent shear strength parameter ($0 \leq \lambda \leq 1$)

$$\alpha = \frac{6}{3 + 2 \lambda}$$

Appendix B

ANALYSIS OF A DYNAMIC CYLINDRICAL CAVITY EXPANSION THEORY

The penetration theory presented by Zhou (1988) was analyzed in an attempt to calculate depths of penetration. The units used in this analysis are kilogram, meter, and seconds. The equation numbers are Zhou's. The variables are defined as follows:

a : radius of projectile	R : radius of nose
A : area of cylindrical section	Vo : initial velocity
C1 : quasi-static coefficient	Y : yield strength
C2 : inertial coefficient	Y1 : effective yield strength
d : diameter of projectile	Zf : depth of penetration
E : Young's modulus	$\alpha 2$: guess
Et : strain hardening	β : material constant
g : gravity	$\epsilon 1$: strain in locked elastic region
l : projectile length	$\epsilon 2$: strain in locked plastic region
L : length of nosecone radius section	θ : ogival half-nose angle
m : mass of projectile	$\rho 1$: density of elastic region
n : number of terms in summation	$\rho 2$: density of plastic region
percent_ $\rho 0$: assume a % porosity for $\rho 1$	$\rho 0$: initial density of target
Ps : shear resistance	ρs : density of steel projectile

The initial values given the variables are as follows:

$d := .004$ $R := .010$ $l := .035$ $\rho 0 := 2130$ $Vo := 100$ $\rho s := 7820$
 $\alpha 2 := .01$ percent_ $\rho 0 := .18$ $n := 1 \dots 10$ $E := 13.62 \cdot 10^9$ $Y := 45 \cdot 10^6$

The densities of the elastic and plastic regions are given by the following relationships:

$$\rho 1 := \rho 0 \cdot (1 + \text{percent_}\rho 0) \quad \rho 2 := \frac{\rho 1}{1 - \alpha 2}$$

The relationship used for the effective yield strength, strain hardening, and the strain in the locked elastic region are as follows, respectively:

$$Y1 := Y \cdot \left[1 - \frac{Et}{E} \right] \quad Et := 1.1 \cdot E \quad \epsilon1 := \frac{Y1}{E} \quad (A.20)$$

The material constant, β , as defined by Zhou:

$$\beta := \frac{3 \cdot Y}{4 \cdot E} - \left[\frac{\epsilon1}{2} \right]$$

The ogival half-nose angle, θ , is developed:

$$a := \frac{d}{2} \quad L := \sqrt{R^2 - (R - a)^2} \quad \theta := \frac{\pi}{2} - a \sin \left[\frac{(R - a)}{R} \right]$$

The quasi-static term and the initial coefficients as defined by Zhou:

$$C1 := \frac{2 \cdot \pi \cdot L}{\cos(\theta)} \left[a \cdot \cos(\theta) - L + \frac{L}{\sin(\theta)} \left[\frac{\theta}{2} + \frac{1}{2} \sin(\theta) \cdot \cos(\theta) \right] \right] \quad (2.42)$$

$$\begin{aligned} C2a := & \frac{2 \cdot L}{a^2 \cdot (\cos(\theta))^2} \left[a - \frac{L}{\sin(\theta)} \right] \\ & \cdot \left[\frac{\rho0}{2} \left[\ln \left[\frac{\sin(\theta) - \cos(\theta) + 1}{\sin(\theta) + \cos(\theta) - 1} \right] - \sin(\theta) \right] \right. \\ & \left. - \frac{\rho2}{2} \ln(\alpha2) \cdot \left[\tan(\theta) - \frac{a \cdot \sin(\theta)^2}{L \cdot \cos(\theta)} - \sin(\theta) \right] \right] \end{aligned} \quad (2.43)$$

$$\begin{aligned} C2b := & \frac{2 \cdot L^2}{a^2 \cdot \sin(\theta) \cdot \cos(\theta)^2} \left[\frac{\rho0}{2} \left[\frac{\theta}{2} - \frac{1}{2} \sin(\theta) \cdot \cos(\theta) \right] - \frac{\rho2}{2} \ln(\alpha2) \right. \\ & \left. \cdot \left[\left[1 - \frac{a}{L} \sin(\theta) \right] \cdot \ln \left[\frac{\sin(\theta) - \cos(\theta) + 1}{\sin(\theta) + \cos(\theta) - 1} \right] - \left[\frac{\theta}{2} + \frac{1}{2} \sin(\theta) \cdot \cos(\theta) \right] \right] \right] \end{aligned}$$

$$C2 := C2a + C2b \quad (\text{Sign may be + or -; it was not given.})$$

The mass of the projectile, m , is given as follows:

$$A := \pi \cdot a^2 \quad m := \left[(1 - L) \cdot A + \frac{3}{4} L \cdot A \right] \cdot \rho_s$$

The shear resistance, P_s , is given as follows:

$$P_s := \frac{E}{3} [1 - e^{-(2 \cdot \theta)}] - \frac{Y1}{2} \ln(\alpha 2) + \frac{Et}{3} \ln(\alpha 2) \cdot \ln[1 - \sqrt{\alpha 2}]$$

$$- \frac{2}{3} Et \cdot \left[\sum_n \left[\frac{(-1)^{n-1}}{n^2} \cdot [\alpha 2^{-.5 \cdot n} - [\alpha 2^{-.5} - 1]^n - 1] \right] \right] \quad (2.20a)$$

And, finally, the depth of penetration, Z_f :

$$Z_f := \frac{m}{2 \cdot A \cdot C2} \ln \left[1 + \frac{A \cdot C2}{C1 \cdot P_s} V_0^2 \right] \quad (2.41)$$

The values obtained for the variables are as follows:

$$m = 0.003 \quad \theta \cdot (180/\pi) = 36.87$$

$$\rho_0 = 2130 \quad \rho_1 = 2513.4 \quad \rho_2 = 2538.788 \quad \alpha 2 = 0.01$$

$$C1 = 0 \quad C2a = -3720.066 \quad C2b = 2099.201$$

$$P_s = 5.829 \cdot 10^{17} \quad Z_f = 4.92145418 \cdot 10^{-13}$$

This is an incorrect Z_f depth. The shear resistance P_s appears to be unusually large. This leads to a check of the shear resistance term or more specifically, the summation of the shear resistance term.

The shear resistance summation term was computed for several values of $\alpha 2$. This term is computed as follows:

$$\alpha 2 := .1, .2 \dots .5 \quad n := 1 \dots 25$$

$$P_{n,(\alpha 2 \cdot 10)} := \frac{(-1)^{n-1}}{n^2} [\alpha 2^{-.5 \cdot n} - [\alpha 2^{-.5} - 1]^n - 1]$$

	$\alpha = .1$	$\alpha = .2$	$\alpha = .3$	$\alpha = .4$	$\alpha = .5$
P =	0	0	0	0	0
	-1.081	-0.618	-0.413	-0.291	-0.207
	2.279	0.921	0.503	0.306	0.195
	-4.821	-1.354	-0.603	-0.321	-0.186
	10.718	2.081	0.756	0.353	0.186
	-24.911	-3.345	-0.992	-0.405	-0.194
	60.006	5.594	1.354	0.483	0.21
	-148.768	-9.665	-1.91	-0.595	-0.234
	377.636	17.158	2.768	0.75	0.267
	-977.648	-31.157	-4.104	-0.967	-0.31
	2573.52	57.656	6.2	1.268	0.366
	-6871.898	108.412	-9.518	-1.688	-0.437
	18578.048	206.638	14.813	2.278	0.53
	-50771.228	-398.493	-23.323	-3.109	-0.648
	140076.327	776.301	37.098	4.285	0.8
	-389733.04	-1525.759	-59.533	-5.957	-0.996
	$1.093 \cdot 10^6$	3022.237	96.284	8.345	1.249
	$-3.083 \cdot 10^6$	-6028.02	-156.803	-11.771	-1.577
	$8.753 \cdot 10^6$	12097.682	256.943	16.705	2.003
	$-2.499 \cdot 10^7$	-24413.887	-423.375	-23.839	-2.557
	$7.168 \cdot 10^7$	49515.906	701.111	34.19	3.282
	$-2.066 \cdot 10^8$	-100884.335	-1166.326	-49.258	-4.229
	$5.977 \cdot 10^8$	206394.848	1948.271	71.26	5.473
	$-1.736 \cdot 10^9$	-423854.969	-3266.798	-103.479	-7.109
	$5.059 \cdot 10^9$	873463.732	5496.727	150.788	9.267

This shows the shear resistance term diverges. This numerical result prompted a theoretical check of the series term for shear resistance using the n^{th} term test for a divergent series.

The n^{th} -Term Test for a Divergent Series. The following series is a term in the formula for target resistance in the cylindrical cavity expansion theory presented by Zhou (1988).

$$\sum_{n=1}^{\infty} \frac{\left[\frac{1}{\alpha^{n/2}} - \left(\frac{1}{\alpha^{1/2}} - 1 \right)^n - 1 \right] (-1)^{n-1}}{n^2} \quad (\text{B-1a})$$

where,

$$\alpha = 1 - \frac{\rho_1}{\rho_2} \quad (0 < \alpha < 1) \quad (\text{B-1b})$$

The numerical evidence indicates this term to be divergent. Analyzing it by the n^{th} -term test for divergence, it is first simplified by choosing a specific value of α (with no loss of generality). A convenient value is,

$$\alpha = \frac{1}{4} \quad (\text{B-2})$$

The series simplifies to,

$$\sum_{n=1}^{\infty} \frac{2^n - 2}{n^2} (-1)^{n-1} \quad (\text{B-3})$$

Allowing the n^{th} term to pass to infinity,

$$\lim_{n \rightarrow \infty} \frac{2^n - 2}{n^2} (-1)^{n-1} = \lim_{n \rightarrow \infty} \frac{2^n}{n^2} (-1)^{n-1} \quad (\text{B-4})$$

Applying L'Hospital's rule,

$$\lim_{n \rightarrow \infty} \frac{2^n}{n^2} (-1)^{n-1} = \lim_{n \rightarrow \infty} \frac{2^{n-1} n (-1)^{n-1} + 2^n (n-1) (-1)^{n-2}}{2n} \quad (\text{B-5})$$

Applying it again,

$$\lim_{n \rightarrow \infty} \frac{2^n}{n^2} (-1)^{n-1} = \lim_{n \rightarrow \infty} \frac{2^{n-2} n(n-1) (-1)^{n-1} + 2^{n-1} (n-1) (-1)^{n-2} + \dots}{2} \quad (\text{B-6})$$

This limit oscillates between + and - infinity, and therefore,

$$\lim_{n \rightarrow \infty} \frac{2^n - 2}{n^2} (-1)^{n-1} \neq 0 \quad (\text{B-7})$$

Therefore, the series B-3 diverges. By inspection, this result is typical of any value of α in its range (0 to 1). Therefore, the series B-1 is divergent by the n^{th} -term test.

Appendix C

OVERVIEW COMMENTS ON DYNA3D

Three features of the computer program DYNA3D are discussed which are relevant to understanding its application to penetration problems involving anchor projectiles in rock. These features relate to the program's capability to handle highly transient events involving material and geometric nonlinearity and interface sliding capability in a robust manner. The discussion equally applies to the two-dimensional program, DYNA2D. Further, the discussion given is introductory, and is generally meant for potential users of the program who are only somewhat familiar with finite element theory and jargon. A detailed description of DYNA3D is provided in the user manual (Whirley and Hallquist, 1991).

Explicit Time Integration

DYNA3D is an explicit finite element computer program for three-dimensional nonlinear dynamic problems. The word explicit refers to the type of direct step-by-step method of numerically integrating or discretizing the system of nonlinear equations of motion. These equations are second order differential equations in time. Specifically, DYNA3D employs the explicit central difference algorithm in its solution. The central difference algorithm advances to the next time step using only known information calculated in the previous two time steps, and because it relies solely on known information while advancing the solution, the algorithm is termed explicit.

In contrast, an implicit finite element computer program requires not only information calculated previously, but also requires unknown information at the end of the time step to advance the solution. To do this it must also solve a system of simultaneous algebraic equations which result from the implicit algorithm's discretization of the equations of motion. This system is often large, and it must be solved each time step because of the nonlinearity present in the equations of motion.

There are, however, two advantages to implicit algorithms. The time steps may be substantially larger than for explicit algorithms, and the numerical process may be unconditionally stable, whereas the explicit algorithms are only conditionally stable. The latter advantage strictly applies to linear problems, however.

A characteristic of explicit temporal integration algorithms is that they must employ very small time steps to maintain stability of the numerical process. This is a consequence of their conditional stability. The time step size is based on a characteristic length of the smallest element in the finite element model. DYNA3D monitors the change in the characteristic length during the solution and automatically adjusts the time step size so that stability is maintained. The user has no control of how small the time step becomes during the solution, except of course initially in the construction of the finite element model.

The net result of employing the explicit time integration algorithm is that DYNA3D can handle highly transient events and complex problems in a fairly straightforward, if not brute force, manner. Abrupt changes in nonlinear material behavior, deformation and loading, all of

which are reflected in the current state of the equations of motion, are generally captured satisfactorily by small time steps and explicit methods. However, very large numbers of time steps are required even for simulations of highly transient events.

Constant Stress Finite Elements

In addition to the straightforward simplicity of an explicit integration algorithm for solving complex nonlinear equations of motion, DYNA3D employs finite elements which allow for simple evaluation of integrals in the finite element formulation, such as the internal force vector integral. This is motivated by the need to minimize the compute time within each time step since large numbers of time steps are required. To this end, the DYNA programs employ constant stress finite elements for solving continuum problems; specifically, a four-node quadrilateral element in DYNA2D, and an eight-node solid element in DYNA3D are used. These are very basic displacement-based finite element formulations.

Further, DYNA3D defaults to a one-point Gaussian quadrature rule at the center of each element to numerically integrate the required integrals. The required integrals are therefore under-integrated for the sake of minimizing the compute time within each time step. The material constitutive equations are therefore only evaluated at the center of each element. Also, a form of numerical instability called "hour glassing" becomes a real concern due to the fact that element stiffness matrices are not fully evaluated (they are rank deficient). They may be prone to assuming spurious shapes, actually resembling an hour glass in some cases. This instability is generally controlled in DYNA3D and is otherwise not a practical concern to the user. On the other hand, specification of full quadrature rules generally results in prohibitive overall compute times for problem solution and is often not a desirable option.

Special Handling Techniques for Contact/Impact

Originally, the DYNA3D algorithm for integrating the equations of motion for nodes which either impact or release on interface surfaces was based on a contact/impact algorithm for implicit temporal integration developed by Hughes, et al. (1976). Special equations for velocities and accelerations in the basic temporal integration algorithm were developed to manage the jump conditions at impact and release of sliding interface nodes. In simple planar impact demonstration problems, they were shown to dramatically improve computational results by eliminating ringing in the impact stress data. Other demonstration problems were subsequently solved in two dimensions involving Hertz contact of curved surfaces, and large deformation contact problems of curved surfaces. These equations were originally incorporated in DYNA3D (Hallquist, et al., 1976) after first adapting them to the explicit temporal integration algorithm.

It was reported (Hallquist, et al., 1977) that in hydrodynamic applications, where the material in constant stress elements support large confinement pressures well above the material strength, "hourglass" or "zero-energy" mode shapes contaminated the solution and was a recurring problem. It was not clear as to whether the aforementioned special handling techniques were the cause of the problem. However, it was eventually concluded in the evolution of the DYNA3D contact/impact capability, that for general application these special handling techniques were too expensive and they have since been dropped.

To solve contact/impact problems, the following procedure was developed to handle sliding surface interfaces in DYNA3D. For each sliding interface prescribed in the finite element model, DYNA3D runs through the following non-iterative update steps for every time step:

1. Slave node search
2. Slave element search
3. Tensile interface force calculation
4. Add slave mass to master mass
5. Momentum calculation
6. Effect of slave element stress on master surface acceleration
7. Effect of slave mass on master surface acceleration
8. Slave node accelerations and velocities
9. Time step size necessary to prevent violation of impenetrability

The ability to prescribe various sliding surfaces in DYNA3D makes it particularly applicable to the problem of penetration of a target by a deformable anchor projectile. In particular, the following types were employed in the present project: the "tied" (type 2) slide surface for joining two parts of the finite element model together to satisfy displacement compatibility at the interface without concern for different mesh subdivision; and the "sliding with separation and friction" (type 3) slide surface for the interface between the anchor projectile and the rock medium. In the latter case, a penalty formulation is employed to manage the implementation of impact/release of adjacent surfaces, and a Coulomb friction model is employed for tangential or sliding motion of the adjacent surfaces. When a slave node penetrates an element on the master surface thereby violating the impenetrability condition, a "penalty" force is applied to the node so that it satisfies the constraint.

Appendix D
ANNOTATED INGRID INPUT DATA FILE

```

try #18, friction = .1
dn3d
ld 1 lp 2 .2 0 .2 35.
ld 2 lp 2 0 .7 .6 .7
ld 5 lp 2 2. 35. 2. 5.864
lap .1 0 -8. 5.864
ld 9 lp 2 .01 35 2. 35.
ld 25 lp 2 .02 0 150. 0
ld 27 lp 2 0 -150. 160 -150.
ld 22 lp 2 .7 0 .7 -160.
ld 24 lp 2 15. 0 15. -160.
ld 28 lp 2 150 0 150 -160.
Si 2 sv fric 0.; si 3 tied;

plane 2 0 0 0 0 1 0 .001 symm
0 0 0 1 0 0 .001 symm
term .5e-3
plti 2.50e-5
mat 1 3 head
steel case - 6dac
ro 7.8e-6
e 209e6
pr .3
sigy 1.2e6
etan 1.e6
mat 2 3 head
sandstone
ro 2.13e-6
e 13.62e6
pr .2
sigy .02e6
etan 0
endmat
part 2 5 9 1 1 2 24

drag rota 5 0 0 0 0 0 1 90
si 2 1 1 2 2 2 2 m
velo 0 0 -100e3.
end
part 22 27 24 25 2 102 4
drag rota 5 0 0 0 0 0 1 90
si 1 1 1 2 2 1 2 s
si 1 1 2 2 2 2 3 s
b 2 1 1 2 2 2 1 1 1 1 1
end
part 28 25 24 27 2 34 -12 2.0
drag rota 5 0 0 0 0 0 1 90
si 1 1 2 2 2 2 3 m
b 1 1 2 1 2 1 1 1 1 1 1
end
end

```

```

: Problem identity statement.
: Specifies a DYNA3D input file
: Starts the line definitions for the
: projectile geometry. Lines 1, 2,
: 5, and 14 describe the projectile
: geometry.

: Lines 22, 24, 25, 27, and 28
: describe the two part target
: geometry.

: Defines slide interface #2 as a frictional sliding
: surface with voids (gaps) permitted. Slide interface 3
: ties the two parts of the target together.
: Planes 1 and 2 are defined to
: exploit the two planes of symmetry.
: Simulation stop time.
: Simulation plot interval.
: Defines material #1 as DYNA3D material model 3.
: Header comment as indicated in previous line.
: Density
: Young's Modulus
: Poisson's ratio
: Yield stress
: Hardening modulus
: Defines material #2 in the same manner as material
: #1.

: Ends material definitions.
: Defines a 2D projectile part of four lines, assigns
: material #1, and makes a 2 by 24 mesh.
: Creates a 5 piece solid by rotating the mesh 90 degrees
: Positions sliding interface #2 and makes it the master.
: Initial velocity for the part in z direction.
: Ends part definition.
: Creates the fine 2D target mesh.
: Creates a solid from the 2D mesh.
: Locates slide interface #2 and defines it as slave.
: Locates slide interface #3 and defines it as slave.
: Constrains the nodes at the bottom of the target.
: Ends part definition.
: Defines the coarse 2D target mesh.
: Creates a solid from the 2D mesh.
: Position the master for slide interface #3.
: Constrains the nodes at the bottom of the target.
: Ends part definition
: Ends input file

```

Appendix E
SAMPLE INGRID, DYNA3D, AND TAURUS SESSION

The following statements describe a sample session for creating a simulation run for DYNA3D. The sample problem is the large anchor projectile. The first action is to create and save the following lines in a ASCII text editor. The lines that begin with a c are comment lines and are not required for the program to run.

```

Run #1, Large Anchor Projectile Baseline
c friction = .1
c target material model = 3
c target hole radius = .3175
c units are g, cm, sec.
dn3d
c states that a DYNA3D input file will be created
c next 5 lines describe 1/4 of the projectile profile
ld 1 lp 2 .254 0 .254 17.78
ld 2 lp 2 0 .508 1.27 .508
ld 3 lp 2 1.27 17.78 1.27 4.211
lap 0 0 -6.35 4.211
ld 4 lp 2 0 17.78 1.27 17.78
c next 5 lines describe 1/4 of the target profile
ld 21 lp 2 0. 0. 25.4 0.
ld 22 lp 2 .3175 0 .3175 -63.5
ld 23 lp 2 0. -63.5 25.4 -63.5
ld 24 lp 2 10.16 0 10.16 -63.5
ld 26 lp 2 25.4 0. 25.4 -63.5
c Define the sliding interfaces
si 1 sv fric .1; si 2 tied;
c Sliding interface 1 is sliding with voids and has .1 coef. of friction
c Sliding interface 2 is a tied boundary
plane 2 0 0 0 0 1 0 .001 symm 0 0 0 1 0 0 .001 symm
c describes the planes of symmetry
c The termination time and plot interval are set.
term 5e-3 plti 1e-5
c Start define material #1
mat 1 3 head
4340 steel projectile
c assign material model #3 and puts in a heading statement
c density = ro = g/cm^3
ro 7.8
c Young's modulus = e = g/(cm*s^2)
e 2.00e12
c Poison's ratio = pr
pr .3
c Yield stress = sigy = g/(cm*s^2)
sigy 17.9e9
c Tangential modulus = etan = g/(cm*s^2)
etan 10.0e9
mat 2 3 head
sandstone
ro 2.16
e 44e9
pr .3
sigy .234e9
etan .440e9
endmat

```

```

part 2 3 4 1 1 2 14
drag rota 5 0 0 0 0 1 90;
si 2 1 1 2 2 2 1 m
c initial velocity of the projectile in cm/sec.
velo 0 0 -10000.
end
part 22 23 24 21 2 100 4
drag rota 5 0 0 0 0 1 90;
si 1 1 1 2 2 1 1 s
si 1 1 2 2 2 2 2 s
b 2 1 1 2 2 2 111111
c Constrain the boundary in the x, y, and z directions
end
part 26 21 24 23 2 25 -3 2.0
c defines a four sided region, lines 26, 21, 24, 23, assigns material 2
c 34 elements between lines 21 & 23, 12 elements between lines 24 & 26
c -12 (- sign) & the 2 defines the ratio of the first to the last
c segment between lines 24 and 26.
drag rota 5 0 0 0 0 1 90;
si 1 1 2 2 2 2 2 m
b 1 1 2 1 2 1 111111
c Constrain the nodes at the bottom boundary in the x, y,
c and z directions.
end
end

```

The above file was saved as a file named run1 for this example.

Next, the INGRID program is executed by typing ingrid at the prompt. (The program is case sensitive; note the type case when the file names are typed.) The INGRID program then asks for an input and output file name. In this example, respond with:

```
i=run1 o=run1o
```

INGRID then loads the ASCII file run1 and prompts the user for the graphics device driver. Select number 2 for screen output on the Sun IV in graphics window 2. At this point, any of the interactive commands can be entered. To create an input file for DYNA3D type:

```
continue
```

This causes INGRID to create a DYNA3D input file named the output file name given above. In this example, the file name is run1o. INGRID then exits. To start the DYNA3D program type:

```
dyna3d
```

DYNA3D responds with a prompt for input and output file names. In this example, the proper response is:

```
i=run1o g=run1p
```

The input file name (i=) is the same as the output file name from INGRID. The output file name (g=) is run1p and contains all the graphics information for the simulation. DYNA3D terminates when processing is finished. To view the results from the DYNA3D simulation, the post-processor TAURUS is used. To start TAURUS, enter the following command at the prompt in graphics window 2:

```
taurus
```

TAURUS prompts for the input file name. The proper response for this example is:

```
g=run1p
```

TAURUS then prompts for the graphics driver. Enter 2 for a Sunview driver (1152 x 900 resolution). TAURUS is now ready for interactive commands. The following commands created some of the plots shown in this report for the large anchor projectile.

```
state 500
angle 1 ry 75 rx 30 xscale 5 yscale 5 zscale 5
xtrans -15 ytrans 0 v
m 2
contour 8
contour 9
restore
state 500
rx 90 rz 180
xscale 5 yscale 5 zscale 5
angle 1
ytrans -20
xtrans -5 v
m 2 v
contour 8
contour 9
rx 90
ytrans 5
contour 9
contour 8
phs2 matl 1 1 gather
print mtime 3 1 1
mtime 6 1 1
mtime 9 1 1
phs1
exit
```

This concludes the example problem. To create a file that can be printed at a postscript printer, create the lines above in a ASCII editor and add a 4 to the beginning of the file. This causes TAURUS to send all graphic images to a file in postscript printer format. Save the file under the filename lpplot. The response to the TAURUS prompt for input and output file names now becomes:

```
g=runlp c=lpplot
```

This executes all the commands in the file lpplot and creates a file of the images that would otherwise be printed to the screen. TAURUS responds with the file name that the images are stored in. The file name may be dig.ps or dig.psa or dig.psb or etc. If the file is named dig.ps, the file can be sent to the printer by entering the following line at a command prompt once TAURUS is done processing:

```
lpr dig.ps
```

This causes the line printer to start printing. It will take a few minutes to print the file. The file used to create some of the plots for the Zhou penetration problem is given below:

```
4
state 500
angle 1 ry 75 rx 30 xscale 5 yscale 5 zscale 5
xtrans -35 ytrans -20 v
m 2
contour 8
contour 9
restore
state 500
rx 90 rz 180
xscale 5 yscale 5 zscale 5
angle 1
ytrans -45
xtrans -60 v
m 2 v
contour 8
contour 9
rx 90
ytrans 60
contour 9
contour 8
phs2 matl 1 1 gather
print mtime 3 1 1
mtime 6 1 1
mtime 9 1 1
phs1
exit
```

Appendix F

INGRID INPUT DATA FILES FOR PENETRATION SIMULATIONS

The following is a list of the INGRID input files. For Zhou's penetration problem, each file was called a try. The first four tries for the simulation concentrated on developing the slideline technique. Try #5 contained a large plot interval, and, as a result, the response of the projectile could not be tracked. The boundary in try #6 was not constrained. It was not until try #7 that the results were acceptable. Only the input data deviations from try #7 are highlighted.

try #7: Friction = .1, Target hole radius = .7, etan = 1%, boundary constrained

try #8: Target hole radius = 1 mm

try #9: Target hole radius = .51 mm

try #10: Switch master and slave designation on slide boundary 2

try #11: Friction on slide boundary 2 = .05

try #12: Friction on slide boundary 2 = 0

try #13: Target material model #5. pc=0

try #14: Target material model #5. pc=-4500

try #15: Target hole radius 1.5

try #16: Target hole radius .2, Projectile hole radius = .1

try #17: Etan = 0 in target material model #3

try #18: Etan = 0, Friction = 0.

For the large anchor projectile, each file is called a run. Run #1 is the baseline run. Only the input data deviations from run #1 are listed.

run #1: Friction=.1, Target hole radius=.3175, Target material model #3

run #2: Target material model #5

```

try #7, friction = .1, Constrain target, .7 tgt rad
dn3d
ld 1 lp 2 .2 0 .2 35.
ld 2 lp 2 0 .7 .6 .7
ld 5 lp 2 2. 35. 2. 5.864
lap .1 0 -8. 5.864
ld 14 lp 2 .01 35 2. 35.
ld 25 lp 2 .02 0 150. 0
ld 27 lp 2 0 -150. 160 -150.
ld 22 lp 2 .7 0 .7 -160.
ld 24 lp 2 15. 0 15. -160.
ld 28 lp 2 150 0 150 -160.
si 2 sv fric .1; si 3 tied;
plane 2 0 0 0 0 1 0 .001 symm 0 0 0 1 0 0 .001 symm
term .5e-3 plti 1e-5
mat 1 3 head
steel case - 6dac
ro 7.8e-6
e 209e6
pr .3
sigy 1.2e6
etan 1.e6
mat 2 3 head
sandstone
ro 2.13e-6
e 13.62e6
pr .2
sigy .02e6
etan .1362e6
endmat
part 2 5 14 1 1 2 24
drag rota 5 0 0 0 0 0 1 90;
si 2 1 1 2 2 2 2 m velo 0 0 -100e3.
end
part 22 27 24 25 2 102 4
drag rota 5 0 0 0 0 0 1 90;
si 1 1 1 2 2 1 2 s
si 1 1 2 2 2 2 3 s
b 2 1 1 2 2 2 111111
end
part 28 25 24 27 2 34 -12 2.0
drag rota 5 0 0 0 0 0 1 90;
si 1 1 2 2 2 2 3 m
b 1 1 2 1 2 1 111111
end
end

```

```

try #8, frict=.1, Larger hole
dn3d
ld 1 lp 2 .2 0 .2 35.
ld 2 lp 2 0 .7 .6 .7
ld 5 lp 2 2. 35. 2. 5.864
lap .1 0 -8. 5.864
ld 14 lp 2 .01 35 2. 35.
ld 25 lp 2 .02 0 150. 0
ld 27 lp 2 0 -150. 160 -150.
ld 22 lp 2 1 0 1 -160.
ld 24 lp 2 15. 0 15. -160.
ld 28 lp 2 150 0 150 -160.
si 2 sv fric .1; si 3 tied;
plane 2 0 0 0 0 1 0 .001 symm 0 0 0 1 0 0 .001 symm
term .5e-3 plti 1e-5
mat 1 3 head
steel case - 6dac
ro 7.8e-6
e 209e6
pr .3
sigy 1.2e6
etan 1.e6
mat 2 3 head
sandstone
ro 2.13e-6
e 13.62e6
pr .2
sigy .02e6
etan .1362e6
endmat
part 2 5 14 1 1 2 24
drag rota 5 0 0 0 0 0 1 90;
si 2 1 1 2 2 2 2 m
velo 0 0 -100e3.
end
part 22 27 24 25 2 102 4
drag rota 5 0 0 0 0 0 1 90;
si 1 1 1 2 2 1 2 s
si 1 1 2 2 2 2 3 s
b 2 1 1 2 2 2 1 1 1 1 1
end
part 28 25 24 27 2 34 -12 2.0
drag rota 5 0 0 0 0 0 1 90;
si 1 1 2 2 2 2 3 m
b 1 1 2 1 2 1 1 1 1 1 1
end
end

```



```

try #9, frict=.1, Smaller hole in target
dn3d
ld 1 lp 2 .2 0 .2 35.
ld 2 lp 2 0 .7 .6 .7
ld 5 lp 2 2. 35. 2. 5.864
lap .1 0 -8. 5.864
ld 14 lp 2 .01 35 2. 35.
ld 25 lp 2 .02 0 150. 0
ld 27 lp 2 0 -150. 160 -150.
ld 22 lp 2 .51 0 .51 -160.
ld 24 lp 2 15. 0 15. -160.
ld 28 lp 2 150 0 150 -160.
si 2 sv fric .1; si 3 tied;
plane 2 0 0 0 0 1 0 .001 symm 0 0 0 1 0 0 .001 symm
term .5e-3 plti 1e-5
mat 1 3 head
steel case - 6dac
ro 7.8e-6
e 209e6
pr .3
sigy 1.2e6
etan 1.e6
mat 2 3 head
sandstone
ro 2.13e-6
e 13.62e6
pr .2
sigy .02e6
etan .1362e6
endmat
part 2 5 14 1 1 2 24
drag rota 5 0 0 0 0 0 1 90;
si 2 1 1 2 2 2 2 m
velo 0 0 -100e3.
end
part 22 27 24 25 2 102 4
drag rota 5 0 0 0 0 0 1 90;
si 1 1 1 2 2 1 2 s
si 1 1 2 2 2 2 3 s
b 2 1 1 2 2 2 111111
end
part 28 25 24 27 2 34 -12 2.0
drag rota 5 0 0 0 0 0 1 90;
si 1 1 2 2 2 2 3 m
b 1 1 2 1 2 1 111111
end
end

```

```

try #10, friction = .1, Switch master/slave interface
dn3d
ld 1 lp 2 .2 0 .2 35.
ld 2 lp 2 0 .7 .6 .7
ld 5 lp 2 2. 35. 2. 5.864
lap .1 0 -8. 5.864
ld 14 lp 2 .01 35 2. 35.
ld 25 lp 2 .02 0 150. 0
ld 27 lp 2 0 -150. 160 -150.
ld 22 lp 2 .7 0 .7 -160.
ld 24 lp 2 15. 0 15. -160.
ld 28 lp 2 150 0 150 -160.
si 2 sv fric .1; si 3 tied;
plane 2 0 0 0 0 1 0 .001 symm 0 0 0 1 0 0 .001 symm
term .5e-3 plti 1e-5
mat 1 3 head
steel case - 6dac
ro 7.8e-6
e 209e6
pr .3
sigy 1.2e6
etan 1.e6
mat 2 3 head
sandstone
ro 2.13e-6
e 13.62e6
pr .2
sigy .02e6
etan .1362e6
endmat
part 2 5 14 1 1 2 24
drag rota 5 0 0 0 0 0 1 90;
si 2 1 1 2 2 2 2 s
velo 0 0 -100e3.
end part 22 27 24 25 2 102 4
drag rota 5 0 0 0 0 0 1 90;
si 1 1 1 2 2 1 2 m
si 1 1 2 2 2 2 3 s
b 2 1 1 2 2 2 111111
end
part 28 25 24 27 2 34 -12 2.0
drag rota 5 0 0 0 0 0 1 90;
si 1 1 2 2 2 2 3 m
b 1 1 2 1 2 1 111111
end
end

```

```

try #11, friction = .05, Constrain target, .7 tgt hole
dn3d
ld 1 lp 2 .2 0 .2 35.
ld 2 lp 2 0 .7 .6 .7
ld 5 lp 2 2. 35. 2. 5.864
lap .1 0 -8. 5.864
ld 14 lp 2 .01 35 2. 35.
ld 25 lp 2 .02 0 150. 0
ld 27 lp 2 0 -150. 160 -150.
ld 22 lp 2 .7 0 .7 -160.
ld 24 lp 2 15. 0 15. -160.
ld 28 lp 2 150 0 150 -160.
si 2 sv fric .05; si 3 tied;
plane 2 0 0 0 0 1 0 .001 symm 0 0 0 1 0 0 .001 symm
term .5e-3 plti 1e-5
mat 1 3 head
steel case - 6dac
ro 7.8e-6
e 209e6
pr .3
sigy 1.2e6
etan 1.e6
mat 2 3 head
sandstone
ro 2.13e-6
e 13.62e6
pr .2
sigy .02e6
etan .1362e6
endmat
part 2 5 14 1 1 2 24
drag rota 5 0 0 0 0 0 1 90;
si 2 1 1 2 2 2 2 m
velo 0 0 -100e3.
end
part 22 27 24 25 2 102 4
drag rota 5 0 0 0 0 0 1 90;
si 1 1 1 2 2 1 2 s
si 1 1 2 2 2 2 3 s
b 2 1 1 2 2 2 111111
end
part 28 25 24 27 2 34 -12 2.0
drag rota 5 0 0 0 0 0 1 90;
si 1 1 2 2 2 2 3 m
b 1 1 2 1 2 1 111111
end
end

```

```

try #12, friction = 0, Constrain target, .7 tgt hole
dn3d
ld 1 lp 2 .2 0 .2 35.
ld 2 lp 2 0 .7 .6 .7
ld 5 lp 2 2. 35. 2. 5.864
lap .1 0 -8. 5.864
ld 14 lp 2 .01 35 2. 35.
ld 25 lp 2 .02 0 150. 0
ld 27 lp 2 0 -150. 160 -150.
ld 22 lp 2 .7 0 .7 -160.
ld 24 lp 2 15. 0 15. -160.
ld 28 lp 2 150 0 150 -160.
si 2 sv; si 3 tied;
plane 2 0 0 0 0 1 0 .001 symm 0 0 0 1 0 0 .001 symm
term .5e-3 plti 1e-5
mat 1 3 head
steel case - 6dac
ro 7.8e-6
e 209e6
pr .3
sigy 1.2e6
etan 1.e6
mat 2 3 head
sandstone
ro 2.13e-6
e 13.62e6
pr .2
sigy .02e6
etan .1362e6
endmat
part 2 5 14 1 1 2 24
drag rota 5 0 0 0 0 0 1 90;
si 2 1 1 2 2 2 2 m
velo 0 0 -100e3.
end
part 22 27 24 25 2 102 4
drag rota 5 0 0 0 0 0 1 90;
si 1 1 1 2 2 1 2 s
si 1 1 2 2 2 2 3 s
b 2 1 1 2 2 2 111111
end
part 28 25 24 27 2 34 -12 2.0
drag rota 5 0 0 0 0 0 1 90;
si 1 1 2 2 2 2 3 m
b 1 1 2 1 2 1 111111
end
end

```

```

try #13, material model 5
dn3d
ld 1 lp 2 .2 0 .2 35.
ld 2 lp 2 0 .7 .6 .7
ld 5 lp 2 2. 35. 2. 5.864
lap .1 0 -8. 5.864
ld 14 lp 2 .01 35 2. 35.
ld 25 lp 2 .02 0 150. 0
ld 27 lp 2 0 -150. 160 -150.
ld 22 lp 2 .7 0 .7 -160.
ld 24 lp 2 15. 0 15. -160.
ld 28 lp 2 150 0 150 -160.
si 2 sv fric .1; si 3 tied;
plane 2 0 0 0 0 1 0 .001 symm 0 0 0 1 0 0 .001 symm
term .5e-3 plti !e-5
mat 1 3 head
steel case - 6dac
ro 7.8e-6
e 209e6
pr .3
sigy 1.2e6
etan 1.e6
endmat
mat 2 5 head
sandstone
ro 2.13e-6
g 5.68e6
ku 11.25e6
a0 1.33
a1 60270
a2 0
npts 6
vs 0 .0025 .01 .04 .05 .055
p 0 15000 21250 34000 41300 50000
endmat
part 2 5 14 1 1 2 24
drag rota 5 0 0 0 0 0 1 90;
si 2 1 1 2 2 2 2 m
velo 0 0 -100e3.
end
part 22 27 24 25 2 102 4
drag rota 5 0 0 0 0 0 1 90;
si 1 1 1 2 2 2 1 2 s
si 1 1 2 2 2 2 3 s
b 2 1 1 2 2 2 1 1 1 1 1
end
part 28 25 24 27 2 34 -12 2.0
drag rota 5 0 0 0 0 0 1 90;
si 1 1 2 2 2 2 3 m
b 1 1 2 1 2 1 1 1 1 1 1
end
end
end

```

```

try #14, material model 5
dn3d
ld 1 lp 2 .2 0 .2 35.
ld 2 lp 2 0 .7 .6 .7
ld 5 lp 2 2. 35. 2. 5.864
lap .1 0 -8. 5.864
ld 14 lp 2 .01 35 2. 35.
ld 25 lp 2 .02 0 150. 0
ld 27 lp 2 0 -150. 160 -150.
ld 22 lp 2 .7 0 .7 -160.
ld 24 lp 2 15. 0 15. -160.
ld 28 lp 2 150 0 150 -160.
si 2 sv fric .1; si 3 tied;
plane 2 0 0 0 0 1 0 .001 symm 0 0 0 1 0 0 .001 symm
term .5e-3 plti 1e-5
mat 1 3 head
steel case - 6dac
ro 7.8e-6
e 209e6
pr .3
sigy 1.2e6
etan 1.e6
endmat
mat 2 5 head
sandstone
ro 2.13e-6
g 5.68e6
ku 11.25e6
a0 1.33
a1 60270
a2 0
pc -4500
npts 6
vs 0 .0025 .01 .04 .05 .055
p 0 15000 21250 34000 41300 50000
endmat
part 2 5 14 1 1 2 24
drag rota 5 0 0 0 0 0 1 90;
si 2 1 1 2 2 2 2 m
velo 0 0 -100e3.
end
part 22 27 24 25 2 102 4
drag rota 5 0 0 0 0 0 1 90;
si 1 1 1 2 2 2 1 2 s
si 1 1 2 2 2 2 3 s
b 2 1 1 2 2 2 111111
end
part 28 25 24 27 2 34 -12 2.0
drag rota 5 0 0 0 0 0 1 90;
si 1 1 2 2 2 2 3 m
b 1 1 2 1 2 1 111111
end
end

```

```

try #15, friction = .1, Constrain target, 1.5 hole
dn3d
ld 1 lp 2 .2 0 .2 35.
ld 2 lp 2 0 .7 .6 .7
ld 5 lp 2 2. 35. 2. 5.864
lap .1 0 -8. 5.864
ld 14 lp 2 .01 35 2. 35.
ld 25 lp 2 .02 0 150. 0
ld 27 lp 2 0 -150. 160 -150.
ld 22 lp 2 1.5 0 1.5 -160.
ld 24 lp 2 15. 0 15. -160.
ld 28 lp 2 150 0 150 -160.
si 2 sv fric .1; si 3 tied;
plane 2 0 0 0 0 1 0 .001 symm 0 0 0 1 0 0 .001 symm
term .5e-3 plti 1e-5
mat 1 3 head
steel case - 6dac
ro 7.8e-6
e 209e6
pr .3
sigy 1.2e6
etan 1.e6
mat 2 3 head
sandstone
ro 2.13e-6
e 13.62e6
pr .2
sigy .02e6
etan .1362e6
endmat
part 2 5 14 1 1 2 24
drag rota 5 0 0 0 0 0 1 90;
si 2 1 1 2 2 2 2 m
velo 0 0 -100e3.
end
part 22 27 24 25 2 102 4
drag rota 5 0 0 0 0 0 1 90;
si 1 1 1 2 2 1 2 s
si 1 1 2 2 2 2 3 s
b 2 1 1 2 2 2 111111
end
part 28 25 24 27 2 34 -12 2.0
drag rota 5 0 0 0 0 0 1 90;
si 1 1 2 2 2 2 3 m
b 1 1 2 1 2 1 111111
end
end
end

```

```

try #16, friction = .1, Constrain target, .2 tgt hole
dn3d
ld 1 lp 2 .1 0 .1 35.
ld 2 lp 2 0 .05 .6 .05
ld 5 lp 2 2. 35. 2. 5.864
lap .1 0 -8. 5.864
ld 14 lp 2 .01 35 2. 35.
ld 25 lp 2 .02 0 150. 0
ld 27 lp 2 0 -150. 160 -150.
ld 22 lp 2 .2 0 .2 -160.
ld 24 lp 2 15. 0 15. -160.
ld 28 lp 2 150 0 150 -160.
si 2 sv fric .1; si 3 tied;
plane 2 0 0 0 0 1 0 .001 symm 0 0 0 1 0 0 .001 symm
term .5e-3 plti 1e-5
mat 1 3 head
steel case - 6dac
ro 7.8e-6
e 209e6
pr .3
sigy 1.2e6
etan 1.e6
mat 2 3 head
sandstone
ro 2.13e-6
e 13.62e6
pr .2
sigy .02e6
etan .1362e6
endmat
part 2 5 14 1 1 2 24
drag rota 5 0 0 0 0 0 1 90;
si 2 1 1 2 2 2 2 m
velo 0 0 -100e3.
end
part 22 2/ 24 25 2 102 4
drag rota 5 0 0 0 0 0 1 90;
si 1 1 1 2 2 1 2 s
si 1 1 2 2 2 2 3 s
b 2 1 1 2 2 2 111111
end
part 28 25 24 27 2 34 -12 2.0
drag rota 5 0 0 0 0 0 1 90;
si 1 1 2 2 2 2 3 m
b 1 1 2 1 2 1 111111
end
end

```



```

try #17, friction = .1, 0 hardning modulus, .7 tgt
dn3d
ld 1 lp 2 .2 0 .2 35.
ld 2 lp 2 0 .7 .6 .7
ld 5 lp 2 2. 35. 2. 5.864
lap .1 0 -8. 5.864
ld 14 lp 2 .01 35 2. 35.
ld 25 lp 2 .02 0 150. 0
ld 27 lp 2 0 -150. 160 -150.
ld 22 lp 2 .7 0 .7 -160.
ld 24 lp 2 15. 0 15. -160.
ld 28 lp 2 150 0 150 -160.
si 2 sv fric .1; si 3 tied;
plane 2 0 0 0 0 1 0 .001 symm 0 0 0 1 0 0 .001 symm
term .5e-3 plti 1e-5
mat 1 3 head
steel case - 6dac
ro 7.8e-6
e 209e6
pr .3
sigy 1.2e6
etan 1.e6
mat 2 3 head
sandstone
ro 2.13e-6
e 13.62e6
pr .2
sigy .02e6
etan 0
endmat
part 2 5 14 1 1 2 24
drag rota 5 0 0 0 0 0 1 90;
si 2 1 1 2 2 2 2 m
velo 0 0 -100e3.
end
part 22 27 24 25 2 102 4
drag rota 5 0 0 0 0 0 1 90;
si 1 1 1 2 2 1 2 s
si 1 1 2 2 2 2 3 s
b 2 1 1 2 2 2 111111
end
part 28 25 24 27 2 34 -12 2.0
drag rota 5 0 0 0 0 0 1 90;
si 1 1 2 2 2 2 3 m
b 1 1 2 1 2 1 111111
end
end

```

```

try #18, friction=0 hardening modulus=0
dn3d
ld 1 lp 2 .2 0 .2 35.
ld 2 lp 2 0 .7 .6 .7
ld 5 lp 2 2. 35. 2. 5.864
lap .1 0 -8. 5.864
ld 14 lp 2 .01 35 2. 35.
ld 25 lp 2 .02 0 150. 0
ld 27 lp 2 0 -150. 160 -150.
ld 22 lp 2 .7 0 .7 -160.
ld 24 lp 2 15. 0 15. -160.
ld 28 lp 2 150 0 150 -160.
si 2 sv fric 0; si 3 tied;
plane 2 0 0 0 0 1 0 .001 symm 0 0 0 1 0 0 .001 symm
term .5e-3 plti 1e-5
mat 1 3 head
steel case - 6dac
ro 7.8e-6
e 209e6
pr .3
sigy 1.2e6
etan 1.e6
mat 2 3 head
sandstone
ro 2.13e-6
e 13.62e6
pr .2
sigy .02e6
etan 0
endmat
part 2 5 14 1 1 2 24
drag rota 5 0 0 0 0 0 1 90;
si 2 1 1 2 2 2 2 m
velo 0 0 -100e3.
end
part 22 27 24 25 2 102 4
drag rota 5 0 0 0 0 0 1 90;
si 1 1 1 2 2 1 2 s
si 1 1 2 2 2 2 3 s
b 2 1 1 2 2 2 111111
end
part 28 25 24 27 2 34 -12 2.0
drag rota 5 0 0 0 0 0 1 90;
si 1 1 2 2 2 2 3 m
b 1 1 2 1 2 1 111111
end
end

```

Run #1, Large Anchor Projectile Baseline

```
c friction= .1
c target material model= 3
c target hole radius= .3175
c units are g, cm, sec.
dn3d
c states that a DYNA3D input file will be created
c next 5 lines describe 1/4 of the projectile profile
ld 1 lp 2 .254 0 .254 17.78
ld 2 lp 2 0 .508 1.27 .508
ld 3 lp 2 1.27 17.78 1.27 4.211
lap 0 0 -6.35 4.211
ld 4 lp 2 0 17.78 1.27 17.78
c next 5 lines describe 1/4 of the target profile
ld 21 lp 2 0. 0. 25.4 0.
ld 22 lp 2 .3175 0 .3175 -63.5
ld 23 lp 2 0. -63.5 25.4 -63.5
ld 24 lp 2 10.16 0 10.16 -63.5
ld 26 lp 2 25.4 0. 25.4 -63.5
c Define the sliding interfaces
si 1 sv fric .1; si 2 tied;
c Sliding interface 1 is sliding with voids and has .1 coef. of friction
c Sliding interface 2 is a tied boundary
plane 2 0 0 0 0 1 0 .001 symm 0 0 0 1 0 0 .001 symm
c describes the planes of symmetry
c The termination time and plot interval are set.
term 5e-3 plti 1e-5
c Start define material #1
mat 1 3 head
4340 steel projectile
c assign material model #3 and puts in a heading statement
c density = ro = g/cm^3
ro 7.8
c Young's modulus = e = g/(cm*s^2)
e 2.00e12
c Poison's ratio = pr
pr .3
c Yield stress = sigy = g/(cm*s^2)
sigy 17.9e9
c Tangential modulus = etan = g/(cm*s^2)
etan 10.0e9
mat 2 3 head
sandstone
ro 2.16
e 44e9
pr .3
sigy .234e9
etan .440e9
endmat
part 2 3 4 1 1 2 14
drag rota 5 0 0 0 0 0 1 90;
si 2 1 1 2 2 2 1 m
c initial velocity of the projectile in cm/sec.
velo 0 0 -10000.
```

```

end
part 22 23 24 21 2 100 4
drag rota 5 0 0 0 0 0 1 90;
si 1 1 1 2 2 1 1 s
si 1 1 2 2 2 2 2 s
b 2 1 1 2 2 2 1 1 1 1 1
end
part 26 21 24 23 2 25 -3 2.0
c defines a four sided region, lines 26, 21, 24, 23, assigns material 2
c 34 elements between lines 21 & 23, 12 elements between lines 24 & 26
c -12 (- sign) & the 2 defines the ratio of the first to the last
c segment between lines 24 and 26.
drag rota 5 0 0 0 0 0 1 90;
si 1 1 2 2 2 2 2 m
b 1 1 2 1 2 1 1 1 1 1 1
end
end

```

Run #2, Large Anchor Projectile Baseline
 c target material model= 5
 c units are g, cm, sec.
 dn3d
 c states that a DYNA3D input file will be created
 c next 5 lines describe 1/4 of the projectile profile
 ld 1 lp 2 .254 0 .254 17.78
 ld 2 lp 2 0 .508 1.27 .508
 ld 3 lp 2 1.27 17.78 1.27 4.211
 lap 0 0 -6.35 4.211
 ld 4 lp 2 0 17.78 1.27 17.78
 c next 5 lines describe 1/4 of the target profile
 ld 21 lp 2 0 0 .254 0.
 ld 22 lp 2 .3175 0 .3175 -63.5
 ld 23 lp 2 0 -63.5 25.4 -63.5
 ld 24 lp 2 10.16 0 10.16 -63.5
 ld 26 lp 2 25.4 0 .254 -63.5
 c Define the sliding interfaces si 1 sv fric .1; si 2 tied;
 c Sliding interface 1 is sliding with voids and has .1 coef. of friction
 c Sliding interface 2 is a tied boundary
 plane 2 0 0 0 1 0 .001 symm 0 0 0 1 0 0 .001 symm
 c describes the planes of symmetry
 c The termination time and plot interval are set.
 term 5e-3 plti 1e-5
 c Start define material #1
 mat 1 3 head
 4340 steel projectile
 c assign material model #3 and puts in a heading statement
 c density = $\rho = \text{g/cm}^3$
 ρ 7.8
 c Young's modulus = $E = \text{g/(cm*s}^2\text{)}$
 E 2.00e12
 c Poison's ratio = ν
 ν .3
 c Yield stress = $\sigma_y = \text{g/(cm*s}^2\text{)}$
 σ_y 17.9e9
 c Tangential modulus = $\eta = \text{g/(cm*s}^2\text{)}$
 η 10.0e9
 mat 2 5 head
 sandstone, material model #5
 ρ 2.16
 c Shear modulus = $G = \text{g/(cm*s}^2\text{)}$
 G 8.44e10
 c Bulk unloading modulus = $K_u = \text{g/(cm*s}^2\text{)}$
 K_u 11.25e10
 c a0-2 are constants for the Yield function
 a0 .00133e7
 a1 60.27e7
 a2 0
 c p_c = pressure cutoff
 p_c 0
 npts 6
 c npts specifies 6 points on the p-vs curve
 c ν_s = volumetric strain

```

vs 0 .0025 .01 .04 .05 .055
c p = pressure
p 0 15e7 21.25e7 34e7 41.3e7 50e7
endmat
part 2 3 4 1 1 2 14
drag rota 5 0 0 0 0 1 90;
si 2 1 1 2 2 2 1 m
c initial velocity of the projectile in cm/sec.
velo 0 0 -10000.
end
part 22 23 24 21 2 100 4
drag rota 5 0 0 0 0 1 90;
si 1 1 1 2 2 1 1 s
si 1 1 2 2 2 2 2 s
b 2 1 1 2 2 2 111111
end
part 26 21 24 23 2 25 -3 2.0
c defines a four sided region, lines 26, 21, 24, 23, assigns material 2
c 34 elements between lines 21 & 23, 12 elements between lines 24 & 26
c -12 (- sign) & the 2 defines the ratio of the first to the last
c segment between lines 24 and 26.
drag rota 5 0 0 0 0 1 90;
si 1 1 2 2 2 2 2 m
b 1 1 2 1 2 1 111111
end
end

```

DISTRIBUTION LIST

ADINA ENGRG, INC / WALCZAK, WATERTOWN, MA
AEWES / LIB, VICKSBURG, MS
AEWES / PETERS, VICKSBURG, MS
AFOSR / NA HOKANSON, WASHINGTON, DC
AMPHIB / SAN DIEGO, CA
APPLIED RSCH ASSOCIATION / HIGGINS, ALBUQUERQUE, NM
APTEC / SAN JOSE, CA
ARMSTRONG AERO MED RSCH LAB / OVENSHERE, WRIGHT PATTERSON AFB, OH
ARMY / R&D LAB, STRNC-UE, NATICK, MA
ARMY CORPS OF ENGRS / HQ, DAEN-ECE-D, WASHINGTON, DC
ARMY EWES / WES (NORMAN), VICKSBURG, MS
ARMY EWES / WESIM-C (N. RADHAKRISHNAN), VICKSBURG, MS
ASSOCIATED SCIENTISTS / MCCOY, WOODS HOLE, MA
BING C YEN / IRVINE, CA
CALIF INST OF TECH / PASADENA, CA
CATALINA MARINE SCIENCE / AVALON, CA
CATHOLIC UNIV / CE DEPT (KIM) WASHINGTON, DC
CENTRIC ENGINEERING SYSTEMS INC / TAYLOR, PALO ALTO, CA
CESO / CODE 155, PORT HUENEME, CA
CHILDS ENGRG CORP / K.M. CHILDS, JR., MEDFIELD, MA
COLORADO SCHOOL OF MINES / GOLDEN, CO
COLORADO ST UNIV / FORT COLLINS, CO
COLUMBIA GULF TRANSMISSION / HOUSTON, TX
COMNAVAIRSYSCOM / CODE 422, WASHINGTON, DC
CORNELL UNIV / ITHACA, NY; KULHAWY, ITHACA, NY
COUNTY OF VENTURA / VENTURA, CA
CRREL / CECRL-IC, HANOVER, NH; KOVACS, HANOVER, NH
DAMES & MOORE / LOS ANGELES, CA
DOT / TRANSP SYS CEN (TONG), CAMBRIDGE, MA
DTIC / ALEXANDRIA, VA
DTRCEN / (CODE 1720), BETHESDA, MD
EASTPORT / VENTURA, CA
FAU / BOCA RATON, FL
GEORGE WASHINGTON UNIV / ENGRG & APP SCI SCHL (FOX), WASHINGTON, DC
GEOTECHNICAL ENGRS, INC / MURDOCK, WINCHESTER, MA
GERWICK INC / SAN FRANCISCO, CA
HALEY & ALDRICH, INC. / CHET SEYDEMIR, CAMBRIDGE, MA
HEUZE / ALAMO, CA
HKS INC / PROVIDENCE, RI
HQ AFESC / RDC (DR. M. KATONA), TYNDALL AFB, FL
HYPERBARIC CENTER / DURHAM, NH
INSTITUTE OF MARINE SCIECES / MOREHEAD CITY, NC
IOWA STATE / AMES, IA
JOHN HOPKINS UNIV / BALTIMORE, MD
KWAJALEIN ATOLL / APO AP,
LANTDIVNAVFAECOM / CODE 411, NORFOLK, VA
LAWRENCE LIVERMORE NATIONAL LAB / LIVERMORE, CA
LAWRENCE UNIV / SOUTHFIELD, ME
LEHIGH UNIV / BETHLEHAM, PA
LIN OFFSHORE ENGRG / SAN FRANCISCO, CA

LOCKHEED / RSCH LAB (M. JACOBY), PALO ALTO, CA
LOCKHEED / RSCH LAB (P UNDERWOOD), PALO ALTO, CA
MAINE MARITIME ACADEMY / LIB, CASTINE, ME
MARC ANALYSIS RSCH CORP / HSU, PALO ALTO, CA
MCCLELLAND ENGRS / HOUSTON, TX
MCRDA / QUANTICO, VA
MICHIGAN UNIVERSITY / HOUGHTON, MI
MIT / R.V. WHITMAN, CAMBRIDGE, MA
MOBILE / DALLAS, TX
NAS ADAK / FPO AP
NATL ACADEMY OF SCIENCES / NRC, DR. CHUNG, WASHINGTON, DC
NAVALGROUPONE / SAN DIEGO, CA
NAVFACENGCOM / CODE 04A3, ALEXANDRIA, VA; CODE 04B2 (J. CECILIO),
ALEXANDRIA, VA; CODE 04BE (WU), ALEXANDRIA, VA; CODE 1002B,
ALEXANDRIA, VA; CODE 163, ALEXANDRIA, VA
NAVFACENGCOM CHESDIV / CODE FPO-1C, WASHINGTON, DC
NAVSEASYS COM / CODE 56W23, WASHINGTON, DC
NAVSHIP / VALLEJO, CA; CODE 245L, FPO AP
NCSC / PANAMA CITY, FL
NCTC / PORT HUENEME, CA
NEW ENGLAND MARINE RESEARCH LAB / LIB, DUXBURY, MA
NIEDORODA / GAINESVILLE, FL
NOAA / JOSEPH VADUS, ROCKVILLE, MD
NOAC / NSTL, MS
NORTHWESTERN UNIV / EVANSTON, IL; BAZANT, EVANSTON, IL; CE DEPT
(BELYTSCHKO), EVANSTON, IL
NRL / CODE 4430, WASHINGTON, DC
NRL / RATH, ARLINGTON, VA
NSF / STRUC & BLDG SYSTEMS (KP CHONG), WASHINGTON, DC
NSWC / CODE 3144, POINT MUGU, CA
NUSC / LIB, NEW LONDON, CT
NUSC DET / CODE 44 (CARLSEN), NEW LONDON, CT
NY MARITIME COLLEGE / BRONX, NY
OCNR / CODE 10P4 (KOSTOFF), ARLINGTON, VA
OCNR / CODE 1121 (EA SILVA), ARLINGTON, VA
OCNR / SILVA, ARLINGTON, VA
OIC / POINT MUGU, CA
ONR / CODE 1132SM, ARLINGTON, VA
OREGON STATE UNIV / CORVALLIS, OR; CE DEPT (HUDSPETH), CORVALLIS, OR; CE
DEPT (YIM), CORVALLIS, OR; DEPT OF MECH ENGRG (SMITH), CORVALLIS, OR
PACDIVNAVFACENGCOM / CODE 102, PEARL HARBOR, HI
PENN STATE UNIV / LAB, STATE COLLEGE, PA
PMB ENGRG / LUNDBERG SAN FRANCISCO, CA
PORTLAND STATE UNIV / MIGLIORI, PORTLAND, OR
PURDUE UNIVERSITY / WEST LAFAYETTE, IN
PWC / FPO AP
SAN DIEGO STATE UNIV / SAN DIEGO, CA
SCE / FPO AP
SCHUPACK SUAREX ENGRS INC / SCHUPACK, NORWALK, CT
SCOPUS TECHNOLOGY INC / (B NOUR-OMID), EMERYVILLE, CA
SCOPUS TECHNOLOGY INC / (S. NOUR-OMID), EMERYVILLE, CA
SEAL TEAM 6 / NORFOLK, VA
SEATTLE UNIV / SEATTLE, WA

SHANNON AND WILSON INC / SEATTLE, WA
 SRI INTL / ENGRG MECH DEPT (GRANT), MENLO PARK, CA; ENGRG MECH DEPT
 (SIMONS), MENLO PARK, CA
 STANFORD UNIV / APP MECH DIV (HUGHES), STANFORD, CA; CE DEPT (PENSKY),
 STANFORD, CA; DIV OF APP MECH (SIMO), STANFORD, CA
 STATE OF CALIF / SACRAMENTO, CA
 SUBGROUPONE / SAN DIEGO, CA
 TEXAS A&M UNIV / COLLEGE STATION, TX; HERBICH, COLLEGE STATION, TX
 TRW INC / CRAWFORD, REDONDO BEACH, CA
 TUFTS UNIV / SANYEI, MEDFORD, MA
 UCLA / FOURNEY, LOS ANGELES, CA
 UNIV OF CALIF / SCRIPPS INST OF OCEANOGRAPHY, LA JOLLA, CA
 UNIV OF CALIF BERKELEY / BERKELEY, CA
 UNIV OF CALIFORNIA / CE DEPT (HERRMANN), DAVIS, CA; CE DEPT (KUTTER),
 DAVIS, CA; CE DEPT (RAMEY), DAVIS, CA; CTR FOR GEOTECH MODEL (IDRISS),
 DAVIS, CA; MECH ENGRG DEPT (BAYO), SANTA BARBARA, CA; MECH ENGRG DEPT
 (BRUCH), SANTA BARBARA, CA; MECH ENGRG DEPT (LECKIE), SANTA BARBARA,
 CA; MECH ENGRG DEPT (MCMECKING), SANTA BARBARA, CA; MECH ENGRG DEPT
 (MITCHELL), SANTA BARBARA, CA; MECH ENGRG DEPT (TULIN), SANTA BARBARA,
 CA
 UNIV OF COLORADO / CE DEPT (HON-YIM KO), BOULDER, CO; MECH ENGRG DEPT
 (PARK), BOULDER, CO
 UNIV OF CONN / LEONARD, STORRS, CT
 UNIV OF DELAWARE / NEWARK, DC
 UNIV OF HAWAII / HONOLULU, HI
 UNIV OF HAWAII / KANEOHE BAY, HI
 UNIV OF ILLINOIS / CE LAB (PECKNOLD), URBANA, IL
 UNIV OF MICH / ANN ARBOR, ME
 UNIV OF N CAROLINA / CE DEPT (GUPTA), RALEIGH, NC
 UNIV OF N CAROLINA / CE DEPT (TUNG), RALEIGH, NC
 UNIV OF NY / BUFFALO, NY
 UNIV OF RHODE ISLAND / KOVACS, KINGSTON, RI; VEYERA, KINGSTON, RI
 UNIV OF TENNESSEE / KNOXVILLE, TN
 UNIV OF TEXAS / AUSTIN, TX
 UNIV OF WASHINGTON / MATTOCK, SEATTLE, WA
 UNIV OF WISCONSIN / MILWAUKEE, WI
 UNIV OF WYOMING / CIVIL ENGRG DEPT, LARAMIE, WY
 UNIVERSITY OF CONN / LIBRARY, GROTON, CT
 US MERCHANT MARINE ACADEMY / KINGS POINT, NY
 USA BELVOIR / FORT BELVOIR, VA
 USAMMRC / DRXMR-SM, WATERTOWN, MA
 USCGHQ / G-ECV, WASHINGTON, DC
 USDA FOREST SERVICE / SAN DIMAS, CA
 USNA / OCEAN ENGRG DEPT, ANNAPOLIS, MD
 VIRGINIA INST OF MARINE SCI / GLOUCESTER POINT, VA
 WESTNAVFACENGCOM / SAN BRUNO, CA
 WOODS HOLE OCEANOGRAPHIC / LIB, WOODS HOLE, MA
 WOODWARD CLYDE CONSULTANTS / OAKLAND, CA
 WORCHESTER POLYTECH / SULLIVAN, WORCESTER, MA

DISTRIBUTION QUESTIONNAIRE

The Naval Civil Engineering Laboratory is revising its primary distribution lists.

SUBJECT CATEGORIES

1 SHORE FACILITIES

- 1A Construction methods and materials (including corrosion control, coatings)
- 1B Waterfront structures (maintenance/deterioration control)
- 1C Utilities (including power conditioning)
- 1D Explosives safety
- 1E Aviation Engineering Test Facilities
- 1F Fire prevention and control
- 1G Antenna technology
- 1H Structural analysis and design (including numerical and computer techniques)
- 1J Protective construction (including hardened shelters, shock and vibration studies)
- 1K Soil/rock mechanics
- 1L Airfields and pavements
- 1M Physical security

2 ADVANCED BASE AND AMPHIBIOUS FACILITIES

- 2A Base facilities (including shelters, power generation, water supplies)
- 2B Expedient roads/airfields/bridges
- 2C Over-the-beach operations (including breakwaters, wave forces)
- 2D POL storage, transfer, and distribution
- 2E Polar engineering

3 ENERGY/POWER GENERATION

- 3A Thermal conservation (thermal engineering of buildings, HVAC systems, energy loss measurement, power generation)
- 3B Controls and electrical conservation (electrical systems, energy monitoring and control systems)
- 3C Fuel flexibility (liquid fuels, coal utilization, energy from solid waste)

- 3D Alternate energy source (geothermal power, photovoltaic power systems, solar systems, wind systems, energy storage systems)

- 3E Site data and systems integration (energy resource data, integrating energy systems)

- 3F EMCS design

4 ENVIRONMENTAL PROTECTION

- 4A Solid waste management
- 4B Hazardous/toxic materials management
- 4C Waterwaste management and sanitary engineering
- 4D Oil pollution removal and recovery
- 4E Air pollution
- 4F Noise abatement

5 OCEAN ENGINEERING

- 5A Seafloor soils and foundations
- 5B Seafloor construction systems and operations (including diver and manipulator tools)
- 5C Undersea structures and materials
- 5D Anchors and moorings
- 5E Undersea power systems, electromechanical cables, and connectors
- 5F Pressure vessel facilities
- 5G Physical environment (including site surveying)
- 5H Ocean-based concrete structures
- 5J Hyperbaric chambers
- 5K Undersea cable dynamics

ARMY FEAP

- BDG Shore Facilities
- NRG Energy
- ENV Environmental/Natural Responses
- MGT Management
- PRR Pavements/Railroads

TYPES OF DOCUMENTS

D - Techdata Sheets; R - Technical Reports and Technical Notes; G - NCEL Guides and Abstracts; I - Index to TDS; U - User Guides; ☐ None - remove my name

Old Address:

Telephone No.: _____

New Address:

Telephone No.: _____

INSTRUCTIONS

The Naval Civil Engineering Laboratory has revised its primary distribution lists. To help us verify our records and update our data base, please do the following:

- Add - circle number on list
- Remove my name from all your lists - check box on list.
- Change my address - line out incorrect line and write in correction **(DO NOT REMOVE LABEL)**.
- Number of copies should be entered after the title of the subject categories you select.
- Are we sending you the correct type of document? If not, circle the type(s) of document(s) you want to receive listed on the back of this card.

Fold on line, staple, and drop in mail.

DEPARTMENT OF THE NAVY
Naval Civil Engineering Laboratory
560 Laboratory Drive
Port Hueneme CA 93043-4328

Official Business
Penalty for Private Use, \$300

BUSINESS REPLY CARD

FIRST CLASS PERMIT NO. 12503 WASH D.C.

POSTAGE WILL BE PAID BY ADDRESSEE

NO POSTAGE
NECESSARY
IF MAILED
IN THE
UNITED STATES

COMMANDING OFFICER
CODE L34
560 LABORATORY DRIVE
NAVAL CIVIL ENGINEERING LABORATORY
PORT HUENEME CA 93043-4328

NCEL DOCUMENT EVALUATION

You are number one with us; how do we rate with you?

We at NCEL want to provide you our customer the best possible reports but we need your help. Therefore, I ask you to please take the time from your busy schedule to fill out this questionnaire. Your response will assist us in providing the best reports possible for our users. I wish to thank you in advance for your assistance. I assure you that the information you provide will help us to be more responsive to your future needs.



R. N. STORER, Ph.D, P.E.
Technical Director

DOCUMENT NO. _____ TITLE OF DOCUMENT: _____

Date: _____ Respondent Organization : _____

Name: _____ Activity Code: _____

Phone: _____ Grade/Rank: _____

Category (please check):

Sponsor _____ User _____ Proponent _____ Other (Specify) _____

Please answer on your behalf only; not on your organization's. Please check (use an X) only the block that most closely describes your attitude or feeling toward that statement:

SA Strongly Agree A Agree O Neutral D Disagree SD Strongly Disagree

	SA	A	N	D	SD		SA	A	N	D	SD
1. The technical quality of the report is comparable to most of my other sources of technical information.	()	()	()	()	()	6. The conclusions and recommendations are clear and directly supported by the contents of the report.	()	()	()	()	()
2. The report will make significant improvements in the cost and or performance of my operation.	()	()	()	()	()	7. The graphics, tables, and photographs are well done.	()	()	()	()	()
3. The report acknowledges related work accomplished by others.	()	()	()	()	()	<div style="border: 1px solid black; padding: 5px;"><p>Do you wish to continue getting NCEL reports? <input type="checkbox"/> YES <input type="checkbox"/> NO</p></div> <p>Please add any comments (e.g., in what ways can we improve the quality of our reports?) on the back of this form.</p>					
4. The report is well formatted.	()	()	()	()	()						
5. The report is clearly written.	()	()	()	()	()						

Comments:

Fold on line, staple, and drop in mail.

DEPARTMENT OF THE NAVY
Naval Civil Engineering Laboratory
560 Laboratory Drive
Port Hueneme CA 93043-4328

Official Business
Penalty for Private Use, \$300



BUSINESS REPLY CARD

FIRST CLASS PERMIT NO. 12503 WASH D.C.

POSTAGE WILL BE PAID BY ADDRESSEE

NO POSTAGE
NECESSARY
IF MAILED
IN THE
UNITED STATES



COMMANDING OFFICER
CODE L03
560 LABORATORY DRIVE
NAVAL CIVIL ENGINEERING LABORATORY
PORT HUENEME CA 93043-4328

DEPARTMENT OF THE NAVY

COMMANDING OFFICER
NAVCIVENGRLAB
560 LABORATORY DRIVE
PORT HUENEME CA 93043-4328

Official Business
Penalty for Private Use, \$300
NCEL-6110/2 (4/82)

DEFENSE TECHNICAL INFORMATION CENTER
CAMERON STATION
ALEXANDRIA VA 22304-6145

61Y